REFRACTIVE INDEX ENGINEERING BY 3D SUB-WAVELENGTH NANOSTRUCTURING FOR APPLICATIONS IN OPTICS AND OPTICAL SENSING

by

Zsolt Levente Poole

BSE, University of Pittsburgh, 2005

MSE, University of Pittsburgh, 2009

Submitted to the Graduate Faculty of

Swanson School of Engineering in partial fulfillment

of the requirements for the degree of

Doctor of Philosophy

University of Pittsburgh

2014

UNIVERSITY OF PITTSBURGH

SWANSON SCHOOL OF ENGINEERING

This dissertation was presented

by

Zsolt Levente Poole

It was defended on

November 25, 2014

and approved by

Guangyong Li, PhD, Assistant Professor

Mingui Sun, PhD, Professor

William Stanchina, PhD, Chairman and Professor

Sung Kwon Cho, PhD, Associate Professor

Paul Ohodnicki, PhD, Material Scientist

Dissertation Director: Kevin Peng Chen, PhD, Associate Professor

REFRACTIVE INDEX ENGINEERING BY 3D SUB-WAVELENGTH NANOSTRUCTURING FOR APPLICATIONS IN OPTICS AND OPTICAL SENSING

Zsolt Levente Poole, PhD

University of Pittsburgh, 2014

In photonics, the flow of light in light-wave circuits is molded by optical materials and structures with different refractive indices. The ingenuities of photonic engineering are often curbed by the limited range in the refractive indices of naturally occurring optical materials. In this dissertation, sub-wavelength 3D nano-engineering is explored to create artificial optical materials with tunable optical properties. Block-copolymer templating coupled with a wet processing route was applied to realize 3D functional metal oxides with nanostructure features in the sub-50nm regime. Using this low-cost and scalable manufacturing method, high quality films of TiO_2, SnO_2, ZnO, and SiO_2, with refractive indices continuously tunable in the range of 1.17 to 2.2, is demonstrated. These new optical materials open new opportunities in a wide range of applications. This dissertation explores applications for optical fiber sensing, solar cell anti-reflection technology, along with other suggested avenues for exploration.

An expansion of the sensory capability of optical fiber type sensors to include the detection of chemical species, from low to high temperatures, is demonstrated. The merger of functional metal oxides with optical fiber is not well explored both theoretically and experimentally. Full wave simulations were performed that provide valuable insight in the design of these sensors along with experiments to identify the type of the sensory responses. Measurements performed using

Optical Frequency Domain Reflectometry demonstrate the use of the developed sensors for the distributed type detection of hydrogen at very high temperatures, for applications in hydrogen driven Fuel Cells. With distributed sensing a single sensor can function as a linear combination of hundreds of sensor and can be used to analyze existing gradients across the sensor element.

Optical anti-reflection technology can benefit substantially from the extensive broadening of the available refractive indices. Optimal anti-reflection coatings predicted by theory rely on continuous gradual changes in the refractive indices which are too difficult to manufacture conventionally, if at all. The use of the developed refractive index engineering scheme for the realization of low cost and practical, broad-band and omnidirectional anti-reflection coatings with an improved efficiency, is also demonstrated.

TABLE OF CONTENTS

LIST OF TABLES

LIST OF FIGURES

PREFACE

First and foremost I would like to thank my wife for her endless support in all aspects of my life. For being there in difficult times and for sharing the good ones. During my pursuit of a doctorate degree, she gave birth to our beautiful daughter. My wife and daughter, besides providing endless joy in my life, have motivated me to push harder and to become more focused in my work. They have been there every step of the way and together we have successfully arrived to this point, the long awaited time when I finally obtain my PhD and may begin to earn a proper living. I would also like to thank my mom and dad for being there and for being a positive influence in my life by challenging me to do better.

I would like to thank Paul, our collaborating partner from the National Energy Technology Laboratory. He has provided invaluable support from the beginning of the project in all aspects. From discussions to idea development to providing sample imaging support. Paul has spent time and effort with Functional Ion Beam and Scanning and Transmission Electron Microscopy to help analyze many of our fabricated devices and samples. He has provided their equipment and facilities to confirm and help characterize many of our fabricated sensors. Along with his invaluable assistance in acquiring additional funding to support me throughout my PhD carrier and providing further support by sponsoring me for a post doctorate position at the National Energy Technology Laboratory.

Furthermore, many of my colleagues in the lab that I had the pleasure to interact with, assisted in many aspects of the conducted experiments. Aidong is my successor for the work I was doing with the added expertise in manufacturing optical fiber Bragg gratings. He has provided

support in sample preparation and characterization. Rong is also working on sensors associated with optical fiber with the added expertise in the manufacturing of fiber gratings and fiber lasers. He has provide grating manufacturing support along with support by participating in a variety of discussions that were of great value.

Lastly, I would like to thank Dr. Chen for his continuing support both financially and experimentally throughout my graduate career. For a professor that teaches several classes each semester along with having to maintain financial support for 9 graduate students and a post doc or so, he is frequently available for discussions and to provide experimental guidance when needed. Through his hard work, his labs are well equipped with equipment and tools allowing students to pursue a variety of research topics. Through his established collaborative network of professors and industry contacts, a variety of different projects are in exploration each semester, allowing students to be exposed to a broad scope of engineering and scientific problems.

1.0 INTRODUCTION

In optics and photonics the refractive indices of materials is of fundamental importance in defining the inner workings of devices. At their very core the refractive indices, which are generally complex quantities, are a defining property of the interaction of light with the physical world. The rapid emergence of new photonic/optical devices and their widespread implementation demands a high degree of specialization and new methods to push the boundaries in order to reduce costs, improve the efficiencies, and to develop new devices and applications. Many of today's advancements are due to our ability to finely tune the optical properties of materials allowing us to push the boundaries. Advances in semiconductor processing and thin film technologies has brought us optical fiber, advanced thin film components such as antireflection coatings, advanced optical filtering, great advances in photovoltaics, medical technologies, and sensor technologies.

Manipulating important functional materials such as metal oxides at the nanometer scale has seen a tremendous amount of effort to improve on existing technologies and to develop new ones. These types of materials, nanomaterials, can extend our ability in adjusting the material properties, beyond what is achievable by conventional means. Nanostructures with features in the sub-50nm regime have different electronic, chemical, and physical properties from their bulk counterparts, and generally, can be regarded as new materials[1-5]. Manipulating materials in the deep sub-wavelength regime is at the forefront of photonic science, bringing together such diverse fields as chemistry, physics, and engineering. Decades of developments in fabrication techniques

have led to lithography by light, the recording of light generated patterns[6, 7], dip-pen lithography in which specialized inks in combination with nano-tips are used to print down to the 50nm scale[8], with various methods towards the realization of nanorods and alike. Various chemical deposition techniques, the directed self-assembly of colloidal particles to produce direct or sacrificial templates[2], to block copolymer assisted self-assembly[4, 9, 10], have been demonstrated as viable nanomaterial manufacturing techniques.

Block copolymer directed self-assembly is an interesting subset of templating and holds tremendous potential for the large scale fabrication of specialized nanomaterials with unique structures not as easily attainable by other means[4, 11]. A wide range of shapes and sizes of nanomaterials can be realized from a few nanometers to a hundred nanometers[11]. Block copolymers are a type of polymeric compositions that can direct the formation of structures on the nanometer scale. Specialized types of materials, as the products of block copolymer directed assembly, have been well explored in applied physics and engineering to create nanomaterials with unique properties towards improved energy storage and conversion devices, photovoltaics, improved electronic components, advanced sensors, to name a few[4, 11-14].

Although this type of templating has been well explored for porous material fabrication and applied in many ways such as enhancing conductometric sensors, some optical sensing, their use in advanced solar cells, to applications in batteries and supercapacitors, the unique refractive indices attainable with nanostructuring with copolymers has only begun to be explored[15]. For that matter, refractive index engineering by nanostructuring has not been well explored all together to unlock their potential in photonics. In comparison with other methods of templating and nano-fabrication techniques, this type of nanomaterial fabrication stands out due to its versatility and range of applicability, not to mention its inherent ability to be used in large scale fabrication.

In this dissertation the use of block copolymer directed templating to tailor the refractive indices of some important metal oxides “at will”, is demonstrated. Nature does not provide a continuous spectrum of refractive indices, therefore being able to create materials with refractive indices than do not otherwise exist opens up many possibilities. One of which is the integration of well-developed sensory materials, such as functional metal oxides, with optical fiber. A low cost route to refractive index engineering could also allow the practical realization of advanced anti-reflection coatings. Photonic devices designed by transformation optics inherently rely on strong refractive index gradients and these are widely researched today, despite the lack of existing technologies to manufacture them. The demonstrated wet processing route could potentially be used to practically realize many of these designs, cost effectively. Nanostructuring common metal oxides on the sub-wavelength scale may even have the potential to realize the large scale fabrication of all semiconductor materials with novel optical properties, such as refractive indices lower than 1, or of negative values.

2.0 REFRACTIVE INDEX ENGINEERING BY NANOSTRUCTURING

The concept of changing the refractive indices of materials is not new and dates back to the Clusius-Mossotti and the Maxwell-Garnett relations. However, practical realizations require manipulation of materials at the nanometer scale. A surge in nanofabrication technology developments in the recent decades has made such manipulations feasible. There are a limited number of reports showing the alteration of the refractive indices of materials by the means of structuring them on the nanoscale and these have been primarily examined for silica[16, 17]. The extension and the exploration of these techniques to such important materials as functional metal oxides can open up possibilities for a range of applications from science and engineering, security, military, to medical devices and other high impact commercially viable applications.

The effect of nanostructuring on the refractive index is relatively straight forward. However, it is important to note that when one is speaking of the refractive index it is highly dependent on the wavelength of interest. To achieve a purely refractive index effect when nanostructuring, which may or may not be complex, it is essential to maintain a sufficient scale of separation between the lowest wavelength of interest and the largest geometric feature unless a more complicated resonance effect is desired. When the scale of structuring and the wavelength are of similar magnitude, depending on the differences in the refractive indices of course, a much more complicated averaging effect surfaces and enters the realm of photonic crystals that can exhibit photonic band-gaps and other resonant behavior due to complex scattering mechanisms[18]. Although it is difficult to say where the boundary between the two lie as it is different for different structures and geometries, for the sake of simplicity a good rule of thumb is to maintain at least an order of magnitude difference between the largest geometric feature and the

smallest wavelength, that is the largest feature should not be greater than ~λ/10, where λ is the wavelength, to be able to use formulas in the quasi-static limit[19]. The basic idea is illustrated in the figure below, where a new material is formed with its optical properties derived from the sub-wavelength constituent components.

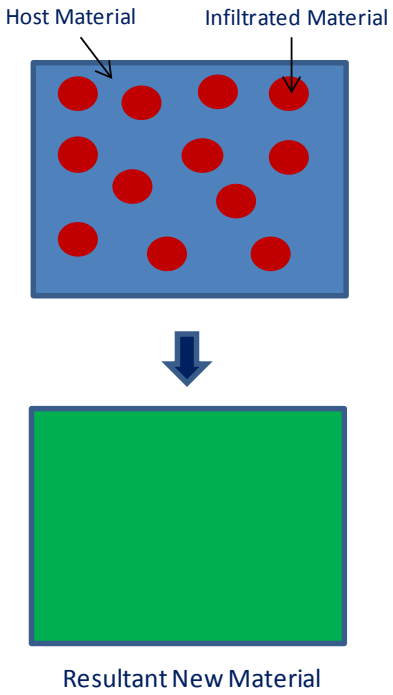

Figure 2-1. Mixing of two materials where nano-spheres of one material is dispersed in another forming a new material.

2.1 AVAILABLE METHODS

For the demonstrated applications in this dissertation the wavelength of interest is from ~350nm to ~1600nm. In order to abide by the general ~λ/10 rule, the largest geometric feature of the

formed nanostructures should be in the ~35nm range or less. Another requirement is that the structuring has to be three-dimensional and the features need to be similar across the dimensions. These two conditions will ensure that there will be minimal changes in the refractive indices across the dimensions and as a function of angle. In other words, we desire to obtain homogenous refractive indices with minimal anisotropy.

In examining the nano-manufacturing techniques available to achieve the stated goals, standard semiconductor processing is eliminated right away as a viable option. With standard semiconductor processing the manufacture of large scale 3D materials is very hard since the material would need to be built up layer by layer. It would take a tremendous amount of effort and time to build up a 1μm thick film composed of 50 layers where each layer would need to be aligned relatively precisely on the sub 20nm scale. This leads us to explore other viable alternatives that may readily provide 3D structures with the desired geometries with much simpler routes.

2.1.1 Colloidal Templating

The use polystyrene spheres were considered first as the means of attempting to change the refractive indices of metal oxides. The examination of the literature showed that this was not accomplished by any published works in prior. Some works showed templating these spheres with diameters of a few hundred nanometers which was as close as could be found on the topic to use as a guide[20]. Polystyrene spheres of a wide range of diameters dispersed in water are commercially available. At a first glance, this route seems like the natural choice due to its apparent overwhelming simplicity. However, after some careful considerations, problems surface.

Templating with colloids of hundred(s) of nm in size can be quite different from templating with colloids that are 20nm in size, as the physics generally change quite a bit when changing the scale by an order of magnitude. The sol-gel precursors developed for the realizations of metal oxides are in general alcohol based. There are a variety of methods that use water as its base component however; experimentally we have found those to provide bad film qualities in preliminary exploration. The availability of polystyrene spheres in solvents other than water proved to be problematic and due to their size which is in the 20nm range, it is too difficult to transfer to an alcohol based solvent due to problems that surface at redistribution and re-separation of the spheres.

Another drawback of colloidal templating may be that the achievable variations in the refractive indices could be quite limited. One reason is that it is difficult to obtain colloidal solutions of higher concentration. Another is that the colloids introduced into a precursor solution may disperse to form a highly homogeneous mixture. However, during and after coating onto a substrate there will be solvent evaporation which will induce densification, starting the colloidal assembly process. It is a possibility that the colloids will achieve their close packing arrangements independently of the metal oxide. That is, it may be possible that the final film will be composed of a bottom layer of closely packed colloids and a top layer of dense metal oxide and vice versa. Or, that the colloids will always achieve the same closely packed arrangement regardless of the colloidal concentration in the mixture. This is because there is no guarantee that the surface of the colloids will chemically interact and bind with the partially hydrolyzed metal alkoxides. Therefore, given the listed considerations and concerns the colloidal method was not chosen and instead block-copolymer templating, discussed next, is chosen as the method to nanostructure metal oxides in the deep sub-wavelength regime.

2.1.2 Block Copolymer Assisted Templating

On the other hand, the use of surfactant assisted templating was found to be very widespread and still at the forefront due to ongoing scientific research in many areas of study. Due to the abundance of publications in using these types of polymers for the fabrication of porous metal oxides, it was adapted as the primary means of testing possible refractive index variations by nano-structuring[21-23].

Block copolymers are at the core of the surfactant method of nanostructuring and are generally composed of two or more distinct blocks bonded to one another. A thermodynamic incompatibility can exist between these blocks, such as mixing oil and water. These copolymers can micro-phase separate on the nanometer scale (5-100nm) to form complex and interesting structures[11, 24]. The type of the structure that forms is highly dependent on the volume fractions of one block with respect to the other, solvents, alkoxides, and etc. A simple way to picture these things is to imagine how oil and water mix where oil droplets are introduced into some water. The oil droplets would disperse but remain intact and acquire a certain shape. Under some external force, these can move around and combine with the other droplets to make new phase separated shapes.

Two competing factors determine the structures that can form in block-copolymers. One is the interfacial energy between the bonded blocks and the other is the amount of chain stretching taking place. The entropy of mixing between two or more blocks is small but these blocks are covalently bonded together so, macro-phase separation cannot occur. The system adapts a chain formation at the molecular level, instead. The minimization of the interfacial energy will drive the blocks to separate from one another, in order to minimize the surface area. This acquired phase separation induces chain stretching away from its equilibrium position. The magnitude of the

effect of these two competing forces depends on the respective volume fractions of the blocks. A general way to describe the structures that form is by a phase diagram that gives the Flory-Huggins interaction parameter in terms of the volume fractions, where χ^N represents the interaction per chain in the polymer network. Figure 2-2 gives an idea of the rich nanostructures that can be formed using block copolymers as structure directing agents as a function of the volume fractions[11].

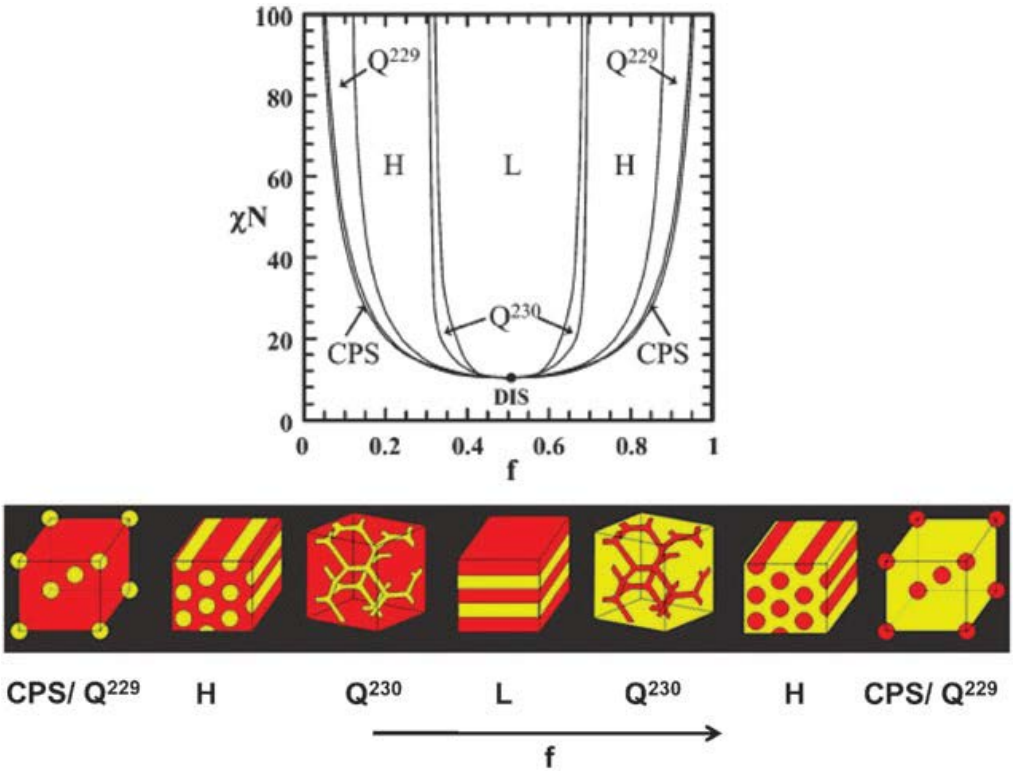

Figure 2-2. Top: Theoretical phase diagram of a diblock copolymer as a function of the volume fraction of one block with respect to the other. **Bottom:** Illustration of the resulting morphologies also a function of the volume fraction. Reproduced ("Adapted" or "in part") from [11] with permission of The Royal Society of Chemistry.

Since the desired final goal is to use these types of polymers to direct the structure of a transition metal oxide, difficulties exist. At the forefront is that nanostructuring by block copolymers can be quite complicated. Phase diagrams for many different block copolymers in different solvents are not readily available and the examination of the obtained structures requires advanced, expensive, and cumbersome techniques such as Transmission Electron Microscopy, and etc. Second, there lies the issue that these are polymers and hence they burn away at relatively low temperatures in comparison. Typically, although highly dependent on the polymer, the temperatures needed to completely remove the organic matrix are low (<200ºC). Since the precursor solutions containing some transition metal complexes need to be converted to an oxide require much higher temperatures, the crystallization and morphology that grows during the process is lacking adequate support and may collapse(Figure 2-3). To prevent these issues, more thermally stable block copolymers can help to a certain extent. Other more complex methods have been developed such as converting a soft copolymer to a hard one during heating that can create a support structure up to higher temperatures[25]. However, these are more complex and, therefore, for the initial development a much a simpler route is taken.

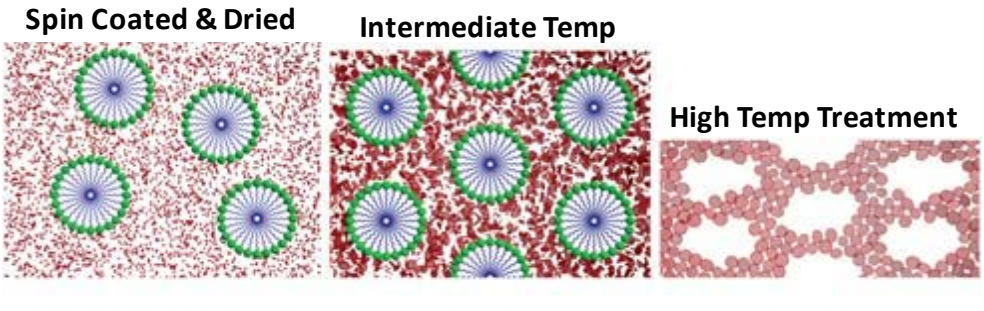

Figure 2-3. A simplified illustration of the micelles formed by Pluronic F-127 and the corresponding variations with the applied temperature. Reproduced ("Adapted" or "in part") from [21] with permission of The Royal Society of Chemistry.

In examining the literature it is found that Pluronic F-127 can provide spherical micelles and this is its most favored phase in a large variety of sol-gel precursor compositions. This tryblock copolymer has a higher removal temperature and, upon exposure to a temperature treatment, the oxide structure that is formed is more likely to remain intact. Although, possibly leaving behind a somewhat skewed structure due some degree of collapse. Pluronic F-127 may form micelles or some other shapes in the alcohol alkoxide solution during the evaporation of the solvent and drying and may organize depending on the environmental conditions[21]. Variation in the refractive indices of the resultant material can be from, for example variation in the density and size of the micelles which can be controlled by changing the amount of the introduced block copolymer, the solvents used, etc.[26].

2.2 EFFECTIVE MEDIUM THEORIES

In examining composite materials with constituent geometric features in the sub-wavelength regime ($<\lambda/10$) it necessary to discuss them as effective mediums, that is, new materials with properties derived from its constituent components. Although, originally derived for approximating the dielectric constants of composite materials, the theory has been expanded to arrive at approximations for a variety of other material properties. The properties that are examined and relevant in this paper are the dielectric constant and the electric conductivity which, for the theories examined are interchangeable terms in the equations. In the following more of a qualitative description is given on the topic to serve as a light introduction rather than a formal rigorous description which has been well developed and it is readily available.

The basic idea behind the effective medium theories is the defined relationship between the microscopic and the macroscopic. The macroscopic field is a type of an average of the microscopic quantities over a region that is large in comparison with the dimensions of the features (colloidal inclusions, holes, i.e. “artificial atoms”) but it is small on the macroscopic scale, i.e. a slowly varying field approximation[27, 28].

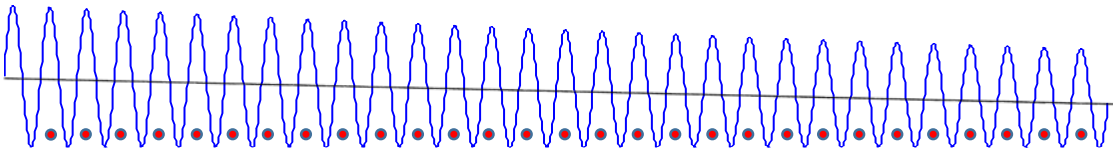

Figure 2-4. Fast varying quantity (microscopic) and slow varying quantity (macroscopic) in a multi-component system**.**

A one dimensional analog is shown in Figure 2.4, which illustrates the basic idea. Here, the fast varying component represents a microscopic quantity where the slow varying component represents a macroscopic quantity. The components that survive a characteristic length scale, which can be arbitrarily defined in attaining a certain degree of accuracy and can be 3,4,10 “atom” spacing, are the ones that influence the macroscopic properties. A valuable link between the macroscopic and microscopic theories, which is also at the fundamentals of the effective medium theories, is given by the Clusius-Mossotti relation. The derivation relies on the Lorentz local field concept which aids in identifying a connection between the dipole moment and the local field by using the molecular polarizability, where P is the polarization.

$$E_{loc} = E_o + \frac{4\pi}{3} P \qquad \textbf{Equation 2-1}$$

The dipole moment for a molecule is given by

$$p = \alpha E_{loc} \qquad \textbf{Equation 2-2}$$

where, α is the polarizability. The polarization **P** for an assemble is

$$P = \sum_i N_i p_i = \sum_i N_i \alpha_i E_{i,loc} \qquad \textbf{Equation 2-3}$$

The sum is carried over the "atoms" with polarizabilities α and local field E_{loc}, and N is simply the number of constituents in a unit volume. Upon substitutions and some algebra, one arrives at the Clusius-Mossotti relation in the usual form which provides a link between the macroscopic quantity such as the dielectric permittivity and the associated microscopic quantity, the atomic polarizability.

$$\frac{\varepsilon - 1}{\varepsilon + 2} = \frac{4\pi}{3} \sum_i N_i \alpha_i \qquad \textbf{Equation 2-4}$$

Similar analysis could be performed to obtain the magnetic permeability, and the electric conductivity can also be found using the methods outlined[28].

2.2.1 Maxwell-Garnet Effective Medium Theory

To arrive at meaningful representations which can be used in estimating the refractive indices, the atomic polarizability α has to be defined using some microscopic theory. A general approach adopted in most literature is the use of the classical spring model however; more accurate descriptions have been introduced and these require the use of second order perturbation theory and other full quantum mechanical models. This dissertation being an introduction to refractive index engineering by nanostructuring with some demonstrated application, complex theories that rely on quantum mechanics are not discussed any further. For the modeling of the dielectric

permittivity for visible and near infrared light, the demonstrated theories are more than adequate. The Maxwell-Garnet theory uses a nice model for the atomic polarizability of the inclusions and regards them as spherical with a being the radius and ε_1 dielectric constant.

$$\alpha = \left(\frac{\varepsilon_1 - 1}{\varepsilon_1 + 2} \right) a^3 \qquad \textbf{Equation 2-5}$$

Upon substitution into the previous formula, one arrives at the Maxwell-Garnet equation in which f is the volume fraction of the inclusions.

$$\left(\frac{\varepsilon - 1}{\varepsilon + 2} \right) = f \left(\frac{\varepsilon_1 - 1}{\varepsilon_1 + 2} \right) \qquad \textbf{Equation 2-6}$$

This equation can give meaningful values for the bulk refractive indices of a composite material made up of a host medium and spherical inclusion under certain circumstances. Another derivation exists for ellipsoidal inclusions which rely on elliptic integrals but it is not described here. An important note here is that this description is not symmetric and that it only works for a two component system. The symmetric aspect, a term found in the descriptions of the effective medium theories simply relates the point of view of the inclusion and the original system and their representation in the variables. In the Maxwell-Garnet case the two points of view, one that regards component A the host and the other that regards component B the host, do not give the same result. Another shortcoming of this model is that it can only be applied practically to inclusions of small volume fractions as in its derivation it is assumed that the spherical domains are spatially separated and that each domain is surrounded by the host medium and that a certain minimum separation exists. Since the model describes a host medium with inclusions, a more useful expression is the following, where the subscript h stands for host and i stands for inclusion.

$$\left(\frac{\varepsilon_{eff} - \varepsilon_h}{\varepsilon_{eff} + 2\varepsilon_h} \right) = f \left(\frac{\varepsilon_i - \varepsilon_h}{\varepsilon_i + 2\varepsilon_h} \right) \qquad \textbf{Equation 2-7}$$

Although the Maxwell-Garnet effective medium theory is useful in understanding the thought behind the process, it cannot be used in practical applications such as porous nanomaterials in which significant volume fractions can exist[28].

2.2.2 Bruggeman Effective Medium Theory

On the other hand, Bruggeman's effective medium theory, built on the Maxwell-Garnet theory, treats the different components of the mixture equivalently without any assumptions on their distribution, i.e. it is symmetric with respect to either point of view and either can be regarded as the host or the inclusion, without limit the number of constituents. In the derivation, a change in the flux through a sphere by its polarization, is considered.

$$\Delta\phi_1 = 2\pi \frac{a^3}{R} \varepsilon E_o \left(\frac{\varepsilon_1 - \varepsilon}{\varepsilon_1 + 2\varepsilon} \right) \qquad \textbf{Equation 2-8}$$

This method brings in view a relation and using this Bruggeman made the hypothesis that there should not be a change in the flux.

$$f_1 \Delta\phi_1 + f_2 \Delta\phi_2 = 0 \qquad \textbf{Equation 2-9}$$

Upon substitution and generalization to an n components system the relation takes the following form, in which n is the number of Euclidian spatial dimensions.

$$\sum_i f_i \left(\frac{\varepsilon_i - \varepsilon}{\varepsilon_i + (n-1)\varepsilon} \right) = 0 \qquad \textbf{Equation 2-10}$$

For a two component system in 3 dimensional space the following quadratic formula is to be evaluated to get the effective dielectric constant

$$-2\varepsilon^2 + \left[3f1\left(\varepsilon_1 - \varepsilon_2\right) + 2\varepsilon_2 - \varepsilon_1 \right] \varepsilon + \varepsilon_1 \varepsilon_2 = 0 \qquad \textbf{Equation 2-11}$$

Bruggeman's effective medium theory is perhaps the most well know of all the effective medium theories and it is widely applied in commercial scientific Ellipsometers (an instrument used in refractive index characterizations).

2.3 MEASURING THE REFRACTIVE INDICES

A critical part in the design of refractive index adjusted metal oxide nanomaterials is to be able to measure the attained refractive indices with a certain degree of accuracy. For measuring refractive indices Ellipsometry is the prominent method and is widely applied in semiconductor physics and micro/nano electronics. It is a non-destructive optical technique for the investigation of the dielectric properties of thin films. This method, coupled with effective medium theories and advanced modeling tools, can be used to measure electrical conductivity, the complex dielectric properties such as refractive index and absorption, material composition, doping concentration, and film thickness. It is very sensitive to changes in the optical responses of materials, specifically the polarization. Although it is a very powerful technique, it has an inherent downside that is, to a great degree, it relies on modeling. This is the fitting of the measured data to models that represent the sample under scrutiny and can lead to uncertainty[29].

2.3.1 Ellipsometry Fundamentals

Light interactions at interfaces give rise to several observable phenomena. The direction of light changes, polarization changes, its velocity changes, impedance mismatches can give rise to reflections, and absorption that attenuates the light intensity due to the imaginary component. The

refractive index associated with a medium can be used to characterize both a velocity change and attenuation, or in other words, it is generally a complex quantity.

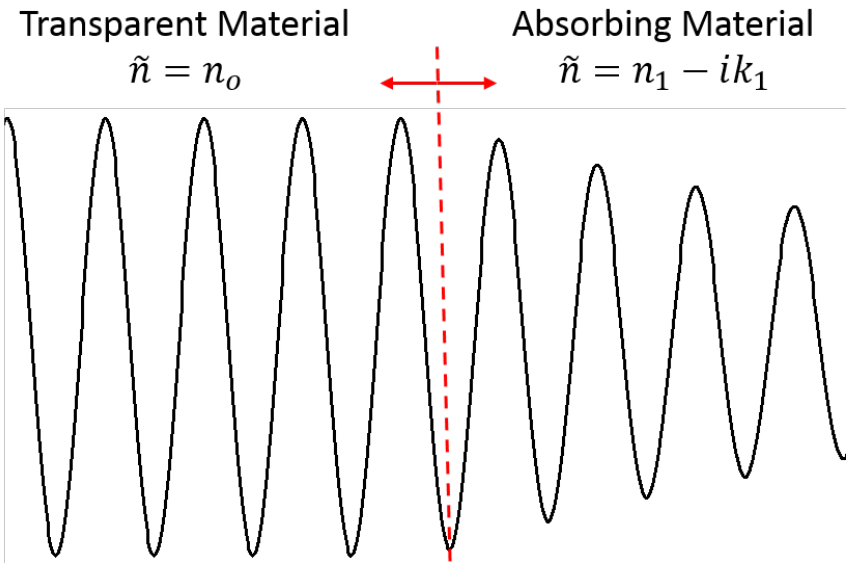

Figure 2-5. A simplified illustration of the interaction of light with matter.

When the medium is transparent the velocity and angles of light change. However, light propagation through an absorbing medium is more complex and the light intensity is reduced depending on the material type and its thickness. The loss in intensity by an absorbing medium is given by an exponential relationship in terms of the intensity at the interface and the absorption coefficient α, according to the Beer-Lambert law.

$$I = I_o e^{-\alpha z} \qquad \textbf{Equation 2-12}$$

Where the absorption coefficient α is given by

$$\alpha = \frac{4\pi k}{\lambda} \qquad \textbf{Equation 2-13}$$

Another important characteristic of absorbing media is the penetration depth, which is how deep light can propagate before decaying to 1/e of the original value. This is just the inverse of the absorption coefficient.

$$\delta = \frac{\lambda}{4\pi k} \qquad \textbf{Equation 2-14}$$

It is important to note that at considerable film thicknesses the reflected light that makes it to the detector can be too weak and can limit the film thickness characterizations. At the interface of two media reflection and transmission takes place at various angles. These angles can be simply determined by Snell's law.

$$\tilde{n}_1 \sin(\theta_1) = \tilde{n}_2 \sin(\theta_2) \qquad \textbf{Equation 2-15}$$

In Ellipsometry, the polarization of light is a critical aspect and it gives the orientation of the electric field. Light can be linearly polarized where the orientation of the electric field is constant. Light can also be circularly and elliptically polarized. The type of polarization is determined by decomposing the polarizations into the two transverse components, x and y for example for a z propagating light beam. In general, the two components of the polarization are out of phase and do not meet the requirements to form either linear or circular polarization. In many cases when linearly polarized light reflects off of a surface its polarization state is converted to elliptical due to the phase shifts that occur between the two polarization states.

Thus far we can find the angles of the light beams, and the absorptive properties but we are missing information that allows for the determination of the amount of the intensity that gets reflected and transmitted. As we mentioned earlier, the electric field can be decomposed into the two components transverse to the direction of propagation, E_p (electric field parallel) and E_s (electric field perpendicular). The Fresnel reflection coefficients provide us with the missing

relative intensity change information. The relative fractions of the two reflected components are given by

$$r_p = \frac{E_p^r}{E_p^i} = |r_p| e^{i\delta_p}$$
$$r_s = \frac{E_s^r}{E_s^i} = |r_s| e^{i\delta_s} \qquad \textbf{Equation 2-16}$$

It is now important to note that for maximum sensitivity it is desirable to change the incident angle to maximize the difference between the s and p components and this maximum is generally in the vicinity of the Brewster's angle ($\theta_B = \tan^{-1}\frac{n_2}{n_1}$), which for most transparent dielectrics with an air interface is near 70°. The ratio of the r_p and r_s components gives the Ellipsometric equations where the parameters Ψ and Δ are called the Ellipsometric angles. The analysis of these two parameters allows one to find the optical properties of thin films under investigation.

$$\rho = \frac{r_p}{r_s} = \tan\Psi e^{i\Delta}$$
$$\tan\Psi = \frac{|r_p|}{|r_s|} \qquad \textbf{Equation 2-17}$$
$$\Delta = \delta_p - \delta_s$$

In real systems, detectors generate currents which are then converted into voltages and, as such, the Ellipsometric angles are derived from these quantities, they are not directly measured. A simplified layout of the different components integrated to perform Ellipsometric measurements is given in the figure below.

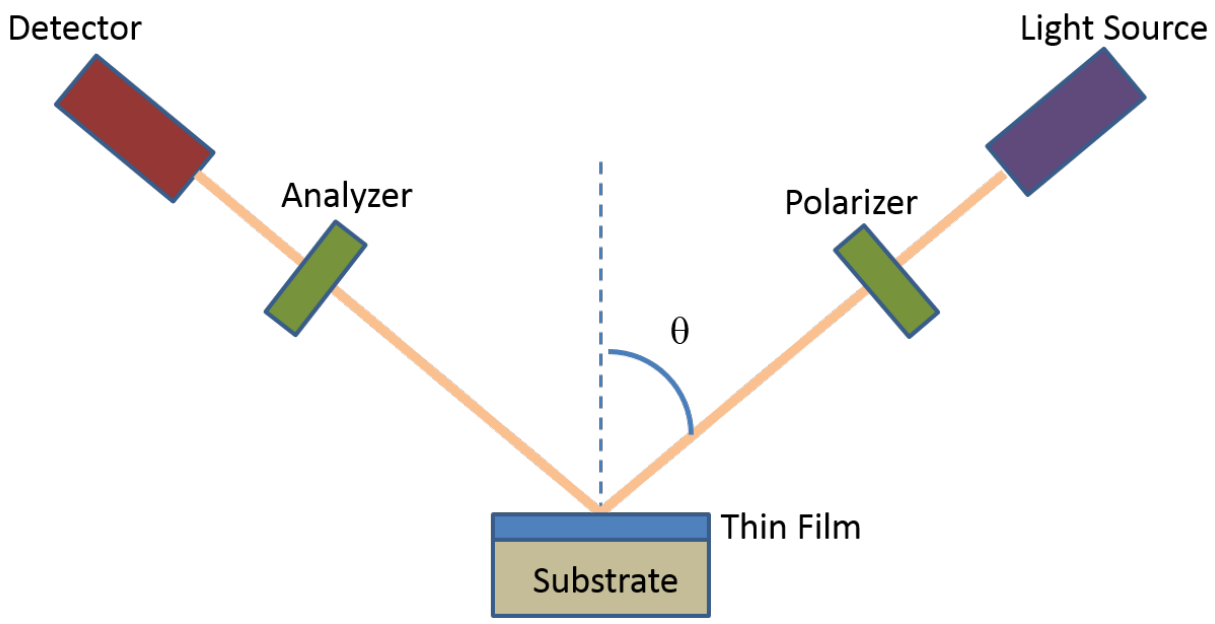

Figure 2-6. A schematic of the components in a typical Ellipsometer

2.3.2 Refractive Index Acquisition by Fitting Models to Data

After the measurement of a sample under test is completed with a set of data in hand, the next step in determining the optical properties is by analyzing the measured data. In general, thin films are deposited on materials such as silicon or glass, or some other types of substrates. The measured data contains optical information from all the transparent layers and the back reflecting substrate of the sample and the information pertaining to the material of interest has to be extracted from this data. The degree of difficulty in this step can be somewhat arbitrary and is highly dependent on the complexity of the film under test. In general it is best to gather as much information as possible such as the type of the substrate, its thickness, whether some oxide layer exists between the substrate and material under test as this will make analysis much easier. In prior it might be beneficial to have an idea of how thick the film under test is. In general, the reduction of the

number of unknowns will greatly aid in the efficiency and accuracy of the determined material properties and, having a good idea of the range of parameters to be acquired in prior, is extremely beneficial.

Most Ellipsometers, nowadays, come with a computer interface and a software package with built in tools to assist in obtaining the pertinent optical properties. Many of these systems will come fully equipped with various minimization algorithms, material files for common materials, and a variety of effective medium theories. After the measurement is completed, one simply builds a model with the associated material files containing dielectric information pertinent in the fitting process. At this point, the fewer the unknown parameters, the more easily an accurate representation is acquired. The typical measure of the quality of the fit is given by the χ^2. Although the quality of fit is a very arbitrary parameter and one has to take many things into consideration such as the width of the spectrum considered. For very wide spectrums in which absorbing regions exist, a χ^2 of 20 might be considered acceptable, whereas for a measurement in the 500-800nm range which for most materials types is not absorbing, one can easily obtain a χ^2 value much less than 1.

It is quite common that due to the deposition process, the properties of the materials under test differ significantly from the bulk tabulated parameters. So, it is not uncommon that advanced modeling techniques need to be applied. These entail performing literature searches to get an idea of equation previously used to acquire good estimates of the dielectric properties of that specific material. The dielectric constants for the metal oxides examined in this dissertation can, in general, be can be modeled by the following dispersion formulas. In general, the classical formula can give relatively good fits for SnO_2, ZnO, and SiO_2, whereas the New Amorphous model is generally

good model to use for fitting TiO_2. The classical dispersion model is described by the following relation[30].

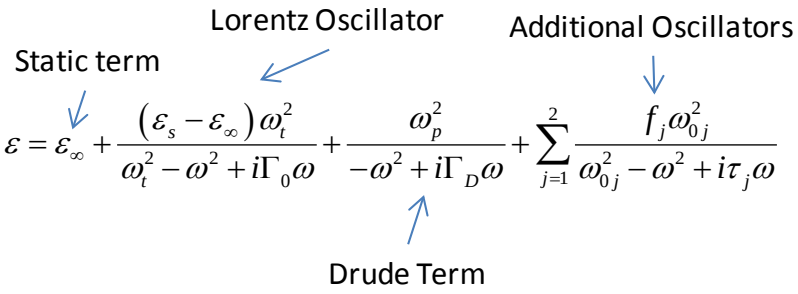

Equation 2-18

The Lorentz oscillator term describes an electron bound to a heavy ion by a spring model with a restoring force. It is widely used to describe transparent dielectrics that are weakly absorbing at most. The Drude term is used to describe the free electrons that may exist due to doping with metals such as aluminum and etc. This is an offshoot of the Lorentz oscillator model without any restoring force, i.e. the electrons are free to move around. The Drude term has a characteristic frequency ω_p, the plasma frequency. The last term, the additional oscillators are extra terms that can be used in the fitting process in improving the quality of the fit due to the fact that real materials are more complex and depending on the deposition process and the composition due to doping or contaminants, additional oscillators might improve the quality of fit because multiple oscillations might actually exist.

The New Amorphous model used in the fitting of TiO_2 is described by the following dispersion relation[31].

$$n(\omega) = n_\infty + \frac{B(\omega - \omega_g) + C}{(\omega - \omega_j)^2 + \Gamma_j^2}$$

$$\begin{cases} \boldsymbol{B_j = \frac{f_j}{\Gamma_j} \cdot \left[\Gamma_j^2 - (\omega_j - \omega_g)^2\right]} \\ \boldsymbol{C_j = 2 f_j \Gamma_j \cdot (\omega_j - \omega_g)} \end{cases}$$

Equation 2-19

With n_∞ being the long wavelength refractive index, ω_j the maximum absorption energy, f_j the oscillator strength, ω_g the band energy, and Γ_j the broadening factor.

When advanced modeling is required, all the parameters in the model can be set as parameters to be found. Many complications can arise and it is good practice to acquire a good bit of background on the material to get a good sense of what values all the parameters should have in general, otherwise one may very frequently encounter fitting results with high quality of fit but with nonsensical terms in the model parameters. It is advisable to first perform fitting in the non-absorbing region with only a Lorentz oscillator term to get the thickness of the film and other parameters such as the thickness for the native oxide on the silicon substrate. Here, one can include effective medium terms for porous systems and other effects such as gradients. Once a reliable fit is achieved in the non-absorbing region, then the fitting wavelength range is increased incrementally into the near infrared region where absorption can occur. For improved quality of fits, generally a Drude term is added if absorption may be present at NIR wavelength.

Several algorithms might be available for finding the parameters that minimize the error of the fit. The most general and most applied algorithm is the Levenberg-Marquardt algorithm. This algorithm uses the steepest descent method by using partial derivatives. This algorithm is very fast however the starting values are very critical. It can easily find itself in a local minimum from which it cannot find itself out of. A benefit of this algorithm is that it returns a correlation matrix and an estimate in the uncertainty in each of the fitted parameters. The correlation matrix provides critical information in determining the uniqueness of the fit. A fit that is highly correlated essentially tells one that the parameter choices are not unique even though an acceptable quality of fit is achieved. In such situations, it is required to return a few steps and get better estimates of the parameters and to examine if some of the parameters are redundant and can be eliminated.

The simplex algorithm is slow in comparison but because it uses the geometric minimization method, it can slowly crawl out of local minima. For this method the choice of initial values is not critical, this is important when not much information is available beforehand. Due to its slow progression, fitting many parameters can take a considerable amount of time but it is good for getting a good idea of the parameters and not good for getting the final solutions due to minimal feedback and fitting accuracy. The Levenberg-Marquardt algorithm in conjunction with the simplex algorithm is a useful and powerful combination. The simplex algorithm would be used to get good estimates of the starting values whereas the prior is used to quickly make adjustments and acquire fast fits with the changes to arrive at improved estimates over a large parameter space. This is because, in practice, it is not uncommon to have to fit 6-11 or so parameters simultaneously. This can be cumbersome and tedious at times to arrive at uncorrelated good quality fits especially for nanoporous systems where different materials are mixed together and where a volume fraction gradient through the thickness of the sample may exist.

2.4 EXPERIMENT

2.4.1 Precursor Synthesis

The method of block copolymer templating is applied to demonstrate that the refractive indices of important functional metal oxides such as SnO_2, ZnO, and TiO_2, and other oxides such as SiO_2 can be effectively controlled “at will”. Pluronic F-127 is used as the block-copolymer for all the engineered nanomaterials. A general scheme common for all the metal oxides explored here is given as follows. Either ethanol, or 2-butanol is used as the solvent in which a metal salt is added

with the addition of the copolymer. In most cases HCl is used as the stabilizer for the metal alkoxide solutions containing Pluronic F-127. In the case of ZnO, ammonium hydroxide is used as the stabilizer. An initial heat conditioning of the precursor promotes the cross-linking of the polymer to create the polymer network. A final heat conditioning removes the polymer components leaving air holes behind. When heating above ~200^{o}C, the metal complexes are converted to metal oxide and form around the block copolymer. Although, the conversion to metal oxide partially happens throughout all the stages, full conversion is achieved, in general, when a temperature of above 300^{o}C is maintained. A chart showing the general procedure is outline below.

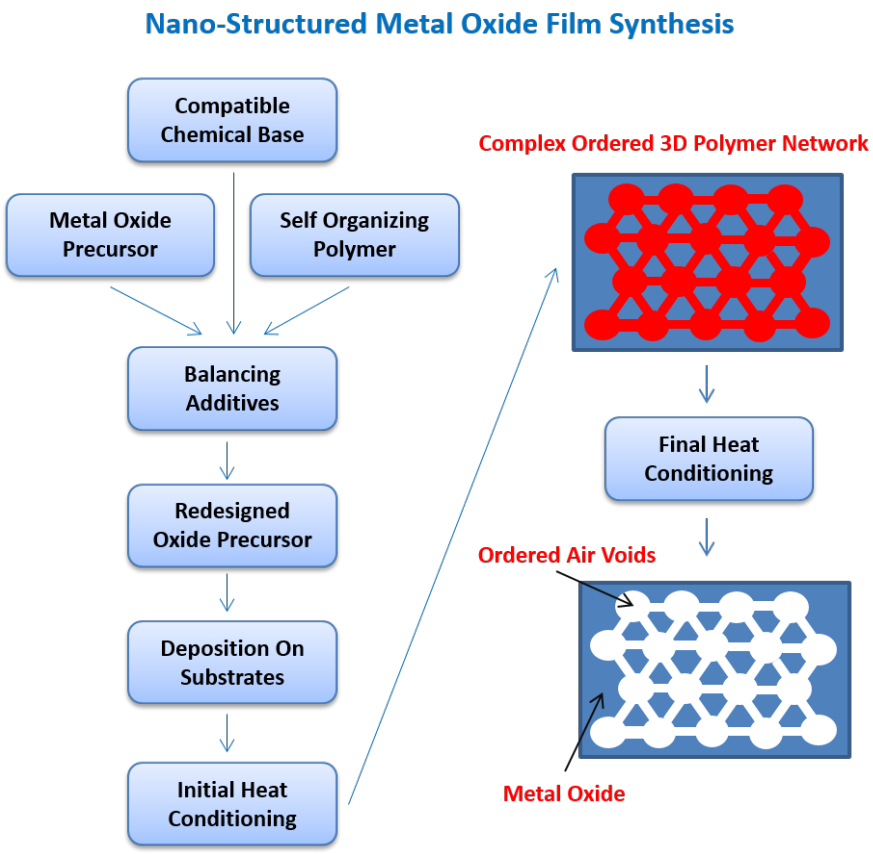

Figure 2-7. A block diagram showing the general scheme in the realization of the various metal oxide nanomaterials.

There are a number of reports that demonstrate a higher degree of order with this type of templating. To increase the degree of ordering, usually additional complex processes are required in carefully adjusted and humidity controlled environments[21, 22, 24, 32]. Maintaining a constant humidity level and circulation can stabilize the hydralization of the sol-gel which can lead to structure stability and maintaining and creating order. For the work presented to explore the refractive index adjustability of the selected functional metal oxides, these processes were not employed as the ordering lengths are not a critical component. The degree of ordering however might be critical in attaining a high degree of repeatability and precision.

It is important to control the amount of water that is introduced into the sol-gel precursors intentionally or unintentionally[24]. Most of the ingredients are hydroscopic, therefore left open in ambient conditions will absorb water from the air. Achieving a stable solution that provides good film quality is highly dependent on this. It was found that after some time the HCl solution used to adjust the pH would degrade by the opening and closing of the bottle lid in ambient air. This lead to the reduction of the concentration of the HCl source and an increase in the water added to the solution. The same thing applies to the use of the other ingredients, as well. Keeping in mind that the degradation of the chemical components can explain difficulties in repeatability over time.

2.4.1.1 SnO_2 Precursor

There are a number of publications dealing with the manufacture of nanostructured tin oxide with Pluronic F-127 as the block-copolymer[21-23, 33]. For the synthesis of SnO2, SnCl4 is used to provide Sn and 37% HCl was used to adjust the pH. Some difficulties were encountered that resulted in bad film quality and were thought to stem from the rapid hydralization of the tin oxide precursor as it was exposed to ambient humid air during the processing. There are a number of possible routes explored in literature for the formation of nanoporous SnO2. Several variations were explored in an attempt to examine the film quality produced by each and it involved changing the Sn source and the solvents employed. Improvements in film quality were obtained when the solvent used was ethanol and the solution concentration was reduced with the addition of an excess amount of HCl. The excess amount of 37% HCl reduced the pH of the solution to about ~0.5 greatly reducing the speed of hydralization. In other words, it reduced the speed at which the tin oxide precursor interacted with water in ambient air.

For the demonstration of refractive index variation in nanostructured SnO_2, three solutions were prepared with the following concentrations of $SnCl_4$, Pluronic F-127, HCl, and ethanol. Solution A with the mole fraction of 1:0.008:2:21.74. Solution B has mole fraction of 1:0.04:7.71:39.58, and solution C with 1:0.016:2:21.7. The solutions were stirred for about 3 hours and left to settle for about a day before use.

2.4.1.2 ZnO Precursor

Zinc oxide is a difficult oxide to form into a porous network and there is not much in literature to aid in this development. The difficulty in the manufacture of porous ZnO is due to its high pH requirements. At low pH values (~4 or less) the solutions are unstable and ZnO particles form too quickly and readily sediment. This rapid formation of ZnO is undesirable especially when combined with block copolymers as it prevents the formation of the desired structure. Pluronic F-127 prefers an acidic environment (pH<2) and ZnO prefers a basic environment (pH>8). This inherent incompatibility made it difficult to realize a nanoporous ZnO.

After some trials, it was found that the precursor containing Pluronic F-127 can be stabilized with an excess amount of ammonium hydroxide. The preparation of a stable zinc oxide solution for the formation of nanoporous ZnO consisted of 7g ethanol, 1g zinc acetate dihydrate, 1g Pluronic F-127 to which 3g of 30% ammonium hydroxide was added. The resultant mixture is stirred for several hours and left to settle for about a day before use.

2.4.1.3 TiO_2 Precursor

The general route for the manufacture of the TiO_2 precursor solutions is very similar to that of SnO_2. Either $TiCl_4$ or titanium isopropoxide is used as the Ti source, with HCl as a stabilizing agent which also helps in the dissolution of Pluronic F-127. Ethanol was used as the solvent in

preparing the initial TiO_2 precursor solutions. The following molar ratios of $TiCl_4$ to Pluronic F-127 to 37% HCl to Ethanol were used. 1:0.075:2.6:33, 1:0.011:3.9:37, 1:0.015:5.2:45.3, 1:0.023:7.8:45.3. Ethanol was first placed into a glass vial to which HCl was added and stirred. To this $TiCl_4$ was added drop wise while stirring, followed by the addition of Pluronic F-127. The mixture was stirred at 60°C on a hotplate until a clear solution was obtained. The solution was cooled to room temperature and aged for 1 day before use.

Upon further exploration, it was found that ethanol based precursor solutions were more sensitive to ambient humidity variations. Therefore, formulations were later developed that used 1-butanol instead. A series of precursor solutions were prepared with the following molar ratios of titanium isopropoxide to Pluronic F-127 to 37% HCl to H_2O to 1-butanol. Ti-1 1:0.004:0.54:3.15:28.4, Ti-2 1:0.0066:0.83:4.43:29.3, Ti-3-1:0.01:1.12:5:30.4, Ti-4 1:0.013:1.43:5.64:31.58, Ti-5 1:0.016:1.43:2.3:32.47. Solutions with 1-butanol as solvent were prepared as follows. First, 10g of 1-butanol was added to a glass bottle to which 1.3g H_2O and 1.3g of 37%HCl were added. To this 5g of Pluronic F-127 was added. This solution was stirred until the polymer completely dissolved and this solution was subsequently used as the polymer source. This method was adapted from reference [24]. In a glass vial 1-butanol was added to which a measured quantity of titanium isopropoxide was added. The solution was stirred and to this a measured quantity of the polymer source was added. The mixture was stirred and left to age for 1 day. If precipitate occurred, the solution was stabilized with the addition of a few drops of 1.5M HCl in water. Using 1-butanol as the solvent requires a lower concentration of Pluronic F-127 to achieve the same refractive index when compared with using ethanol as the solvent.

2.4.1.4 SiO_2 Precursor

The SiO_2 precursor solutions were prepared by using ethanol as the solvent, tetraethyl orthosilicate as the Si source, and Pluronic F-127 as the block-copolymer. The solutions were stabilized with the addition of 37% HCl. Four solutions were prepared SiO_2-A with molar ratio 1:0.0051:3.43:45, SiO_2-B with molar ratio 1:0.0058:4:49.7, SiO_2-C with molar ratio 1:0.0068:5.48:49.7, and SiO_2-D with molar ratio 1:0.0086:5.71:54.3, of tetraethyl orthosilicate to Pluronic F-127 to 37% HCl to Ethanol.

Ethanol was first measured into a glass vial to which a measured quantity of HCl was added, followed by stirring. To this a measured quantity of tetraethyl orthosilicate was added, followed by stirring. Lastly, a measured amount Pluronic F-127 was added. The precursor was stirred on a hotplate at 60°C for 1hr, and cooled to room temperature. The solutions were allowed to age for 1 day before use.

2.4.1.5 3% Palladium Doped TiO_2

The preparation of Pd-doped TiO2 precursor solutions generally followed the same procedure as described for the preparation of the TiO2 precursors, with the addition of Pd. The Pd source used was PdCl2 of which 0.32g was added to a mixture of 6g 1-butanol and 0.76g of 37%HCl. This solution was subsequently used as the Pd source. The precursor had the following molar ratio of titanium isopropoxide to PdCl2 to Pluronic F-127 to 37% HCL to H2O to 1-butanol, 1:0.031:0.013:1.76:5.64:32.9.

2.4.2 Sample Preparation

The substrates used for sample preparation were 1inchx1inch square pieces of boron doped silicon wafers with the 100 orientation and 300-350μm in thickness. The substrates were cleaned prior to coating the films by spraying Ethanol onto their surface while spinning with the spin coater at 5K RPM. The substrates were dried by spinning at this speed for 1 minute. The sol-gel precursor solutions were deposited onto the substrates with a micro litter pipette and, generally, 100μL of the solutions were deposited in the center of the 1inchx1inch square piece of silicon wafer. Immediately after dispensing the solution onto the substrates, they were quickly accelerated to 2500 RPM and held for 30 seconds.

After spin coating, the samples were placed in the center of an oven, far away from touching the walls that contained the heating elements. The annealing procedure consisted of heating to 130^{o}C at 5^{o}C/min and holding this temperature for 1 hour. In the next step, the temperatrue was increased to 400-800^{o}C where it was held for 2 hour. The cooling rate was kept slow to maintain good film quality, ususally at a rate of 3^{o}C/min. Another procedure that consisted of heating directly to 400-800^{o}C at 1°C/minute was examined and the obtained refractive indices indicated no significant difference in the two heating procedures.

2.5 RESULTS AND DISCUSSIONS

2.5.1 Refractive Index Measurements

An example of the prepared nanostructured films on silicon substrates is provided in Figure 2-8. The films shown were spin coated at 2500 RPM and annealed at 600°C. The precursor solutions obtained by careful control of the parameters such as the concentration of the various components, spin coating conditions, annealing conditions, provide very good film quality over a large area. The solution processing of metal oxides with block-copolymers is sensitive to many things, including the environmental conditions. Ideal processing conditions would entail the preparation of the precursors in an inert environment, free of humidity and temperature fluctuations. These condition are difficult to realize in an experimental setting, and hence, one can experience variation from sample to sample simply due to fluctuations in the environmental condition form day to day, or even changes in the ingredients over time due to continuing exposure to ambient air. Therefore, one may easily find that the components in the precursor have to be tuned in order to obtain results similar to ones before.

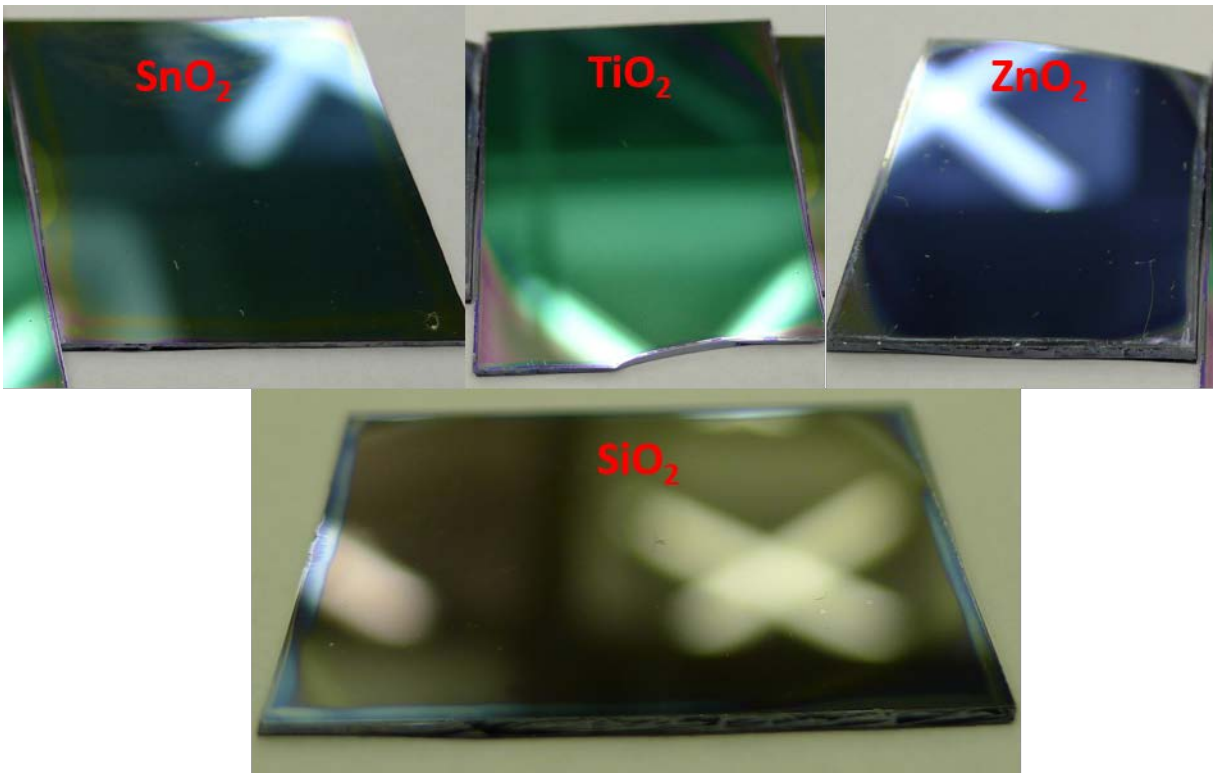

Figure 2-8. Photograph of the manufactured films of SnO_2, TiO_2, ZnO, and SiO_2.

2.5.1.1 Titanium Dioxide

Titanium dioxide thin films with various degrees of porosity were prepared on silicon wafers by spin coating. The obtained films were of good optical quality, sufficient for performing refractive index characterization by Ellipsometry. The samples were annealed at 400°C for 2 hours with a heating and cooling rate of 1°C/minute. The optical properties of the samples were measured with an Ellipsometer at an angle of 70°. A model consisting of a silicon substrate, a 4nm SiO_2 layer, and layer representative of the TiO_2 material coupled with Bruggeman's effective medium theory to model the porosity. The TiO_2 material was modeled with the New Amorphous Model. In general, a χ^2 of less than 10 was obtained for the whole spectral range.

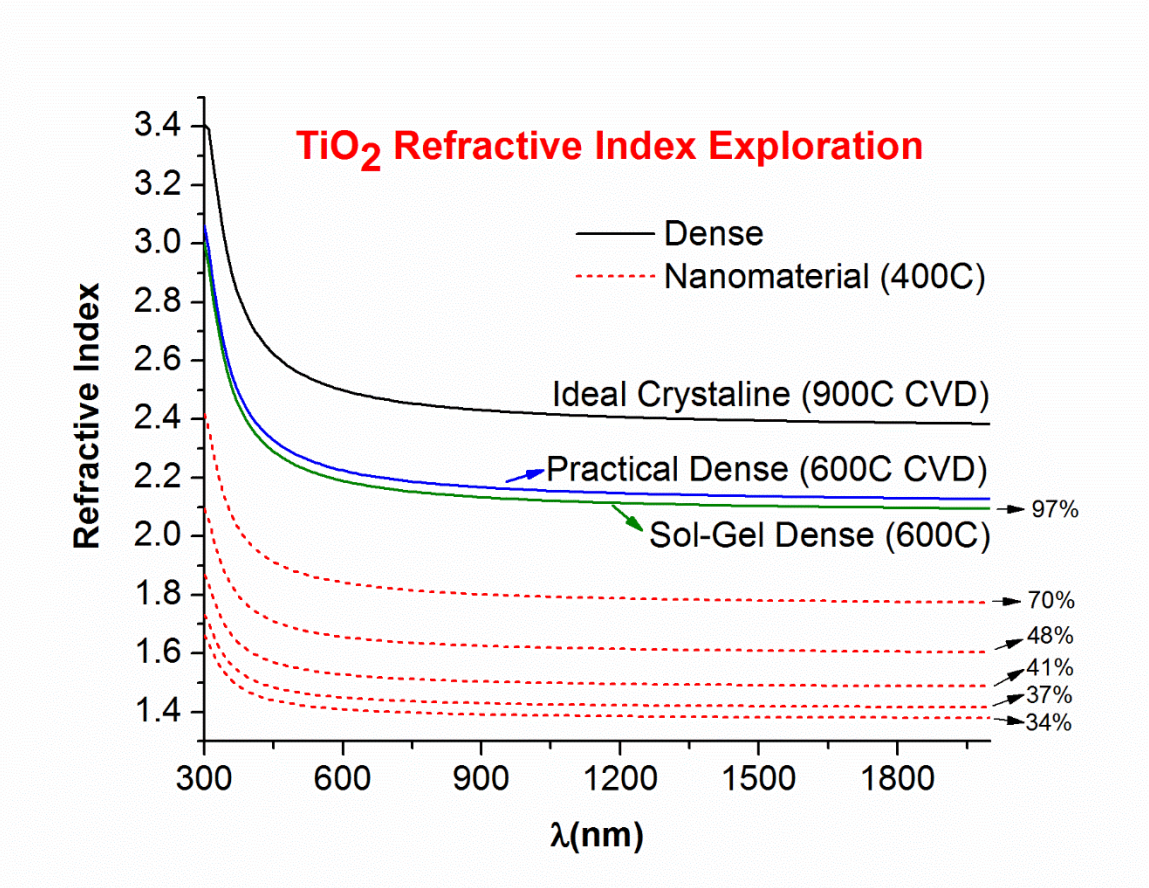

Figure 2-9. Refractive indices of various forms of TiO_2 and TiO_2 nanomaterials.

The refractive indices of various forms of TiO_2 are plotted for comparison in Figure 2-9, including the refractive index of an ideal crystalline TiO_2. The values for the refractive indices by CVD were obtained from references[34-36]. It is evident that templating with Pluronic F-127 has a significant effect on the refractive indices. By simply changing the concentration of the block-copolymer, TiO_2 nanomaterials with refractive indices as low as 1.38 (at a wavelength of 800nm) were obtained. This is in comparison with a value of approximately 2.2 obtained by solution processing. The refractive index of 2.2 was obtained by the recipe presented in the section dealing with anti-reflection coating.

With Figure 2-10, the variation in the refractive indices as a function of the molar ratio between Pluronic F-127 and Titanium, is demonstrated. A successive decrease in the refractive indices is observed until a critical molar ratio. A critical molar ratio is observed around 0.013 when 1-butanol is used as the solvent. Additional increase in the concentration of Pluronic F-127 actually results in a refractive index increase. The mechanism behind this results may be associated with the phase diagram representative of the precursor, which may be similar to the one depicted in Figure 2-2. Although, the actual phase diagram representative of the current precursor is unknown at this time.

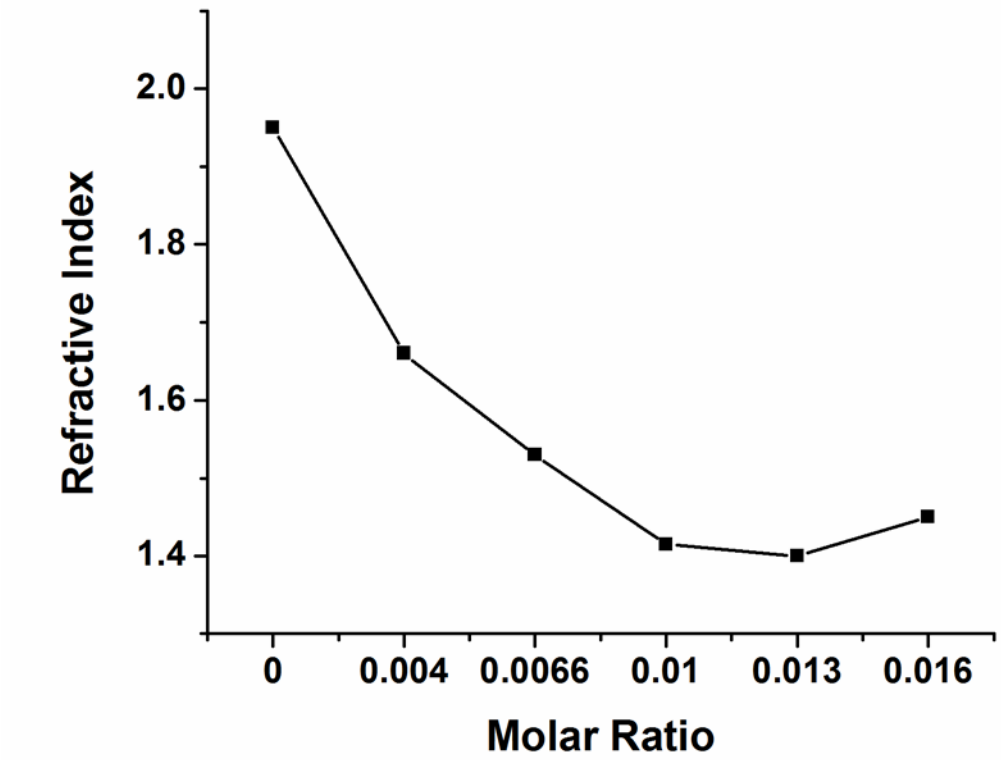

Figure 2-10. Variations in the refractive indices of TiO_2 as a function of the molar ratio between Pluronic F-127 and Titanium at λ=800nm.

2.5.1.2 Tin Oxide

Figure 2-11 shows refractive index measurement results for SnO_2. The optical parameters of the film on the silicon substrate were obtained in the 400-800nm range. A model was created that represented the sample under study, composed of a silicon substrate, followed by a 4nm thick native oxide layer, and last a layer representing the film under test. As described before, the classical model was used in conjunction with Bruggeman's effective medium theory. The fit was performed with only the single Lorentz oscillator part of the classical model. On average a χ^2 of 10 or less was obtained, with the largest amount of uncertainty in the fit of the porosity, which can be on the order of 10%. After fitting, the refractive indices were extrapolated to 1600nm, using the Lorentz oscillator model with Bruggeman's effective medium theory. The reason for the initial limited measurement range is due from the lack of availability of the optical properties of SnO_2 beyond 800nm. The refractive index of the material file for SnO_2 (built into the software package of the Ellipsometer) along with a the refractive index of a 100nm thick sputter coated SnO_2 film estimated porosity of around 3-5%, is included for comparison. Variations in the refractive indices were obtained by controlling the mole fraction of Pluronic F-127 in the precursor solutions. SnO_2-A with mole fraction 1:0.008:2:21.74, B with mole fraction 1:0.04:7.71:39.58, and C with 1:0.016:2:21.7. The refractive index of a D-shaped optical fiber's core at 1550nm is also included. As can be seen, the refractive index of SnO_2-B is lower than the refractive index of the fiber core. Therefore, the precursor for SnO_2-B is later used for integrating the SnO_2 nanomaterial with optical fiber for sensing applications, and it has an estimated porosity of ~60%.

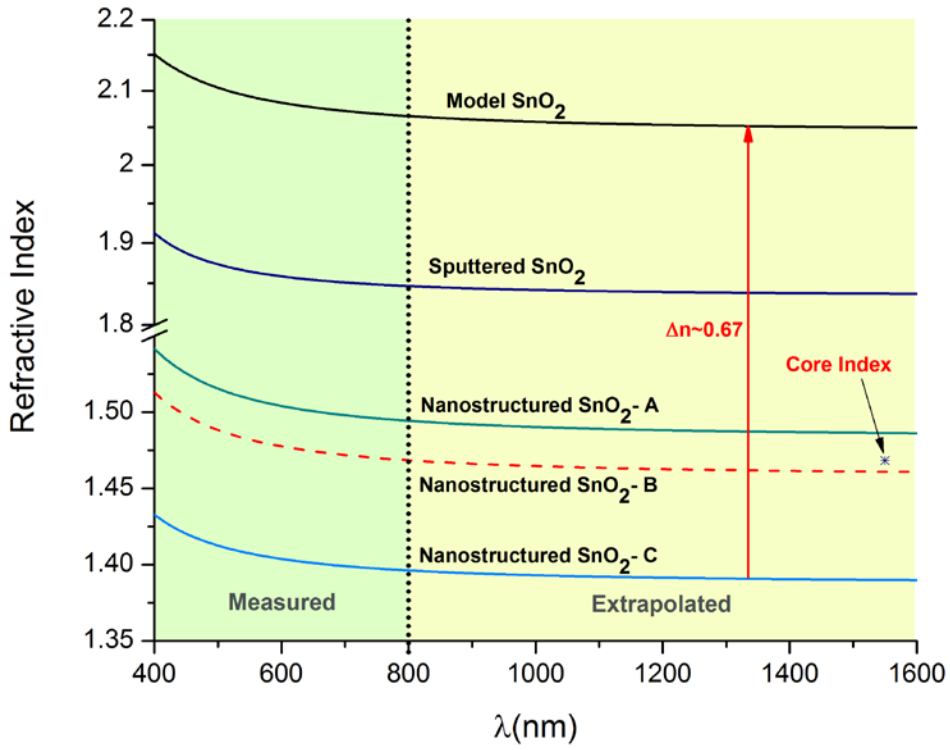

Figure 2-11. The refractive indices of various forms of SnO_2 obtained by measurement. The material file representing SnO_2 is included for comparison, along with the measured refractive index of a sputter coated SnO_2 film. SnO_2-A through C are obtained by templating with Pluronic F-127.

Figure 2-12 shows the results of measurements obtained for another set of samples at which point a direct measurement of the data from 400nm to 1600nm was obtained. The Lorentz single oscillator model with Bruggeman's effective medium theory was used to perform the fit. A good quality of fit was obtained for the whole spectral range. This plot, showing the refractive indices without extrapolation, agree relatively well with the first plot with extrapolation. This is due to the slowly varying nature of the refractive indices of common metal oxides at NIR wavelengths.

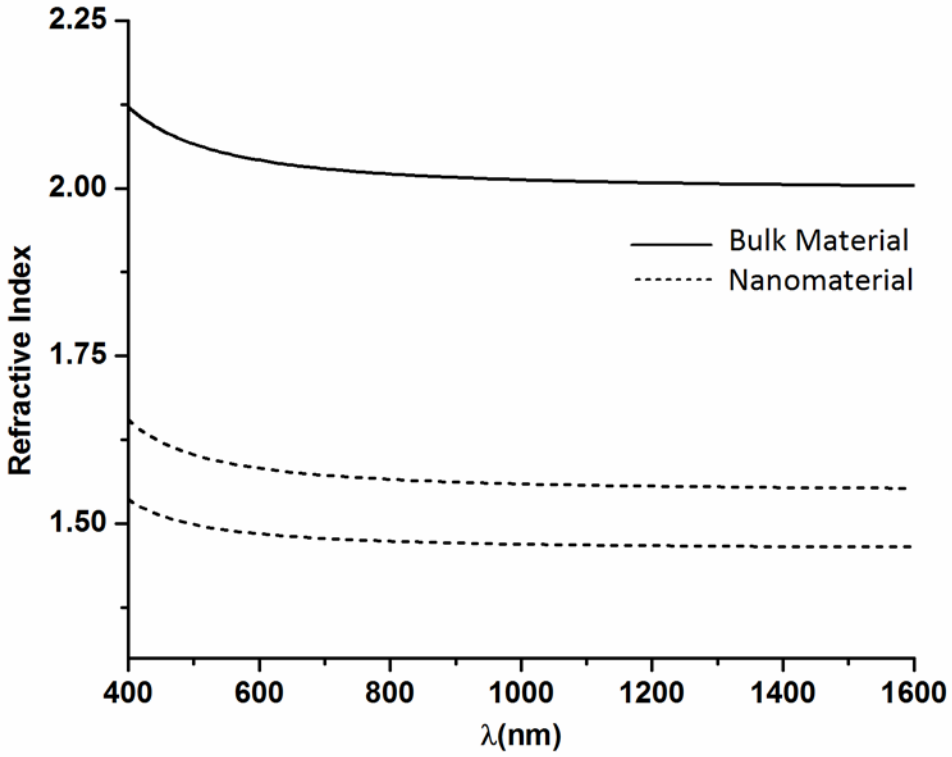

Figure 2-12. Direct measurement of the optical parameters from 400-1600nm and fitting in the whole range to obtain the refractive indices.

2.5.1.3 Zinc Oxide

For ZnO, only one stable solution was prepared at this time. The processed nanoporous ZnO was measured using an Ellipsometer. Ψ and Δ were fitted with a χ^2 of 3 over a broad wavelength range. A good fitting was achieved to a Lorentz oscillator model. The volume fraction of air in the presented ZnO nanostructure is about 70%.

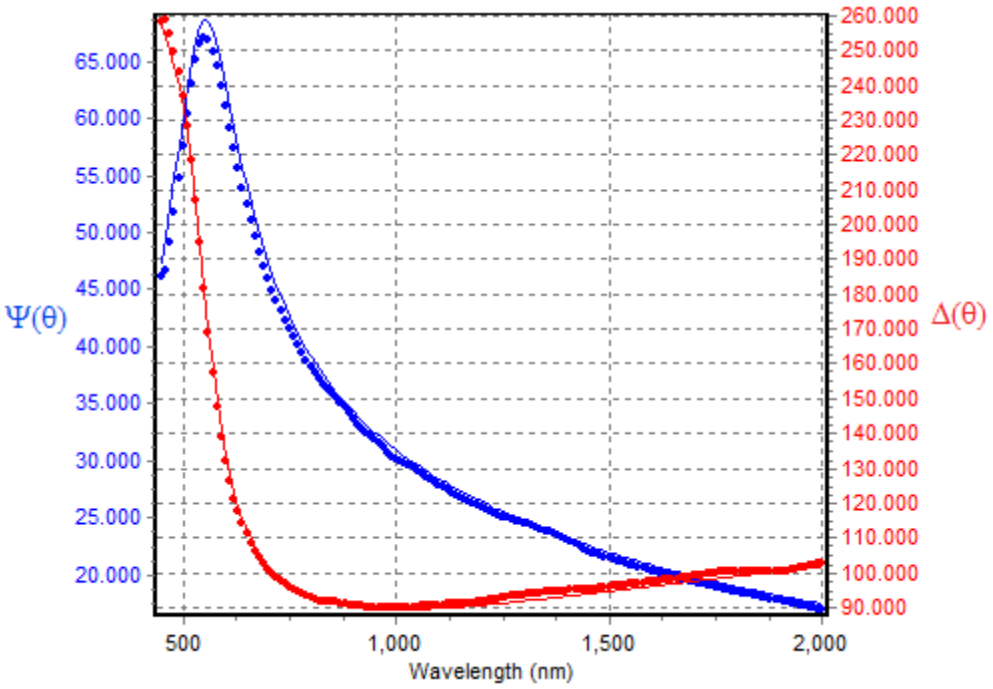

Figure 2-13. Example fitting results showing the quality of the fit. The Ellipsometer parameters (Ψ and Δ) and the model generated data points agree well with one another.

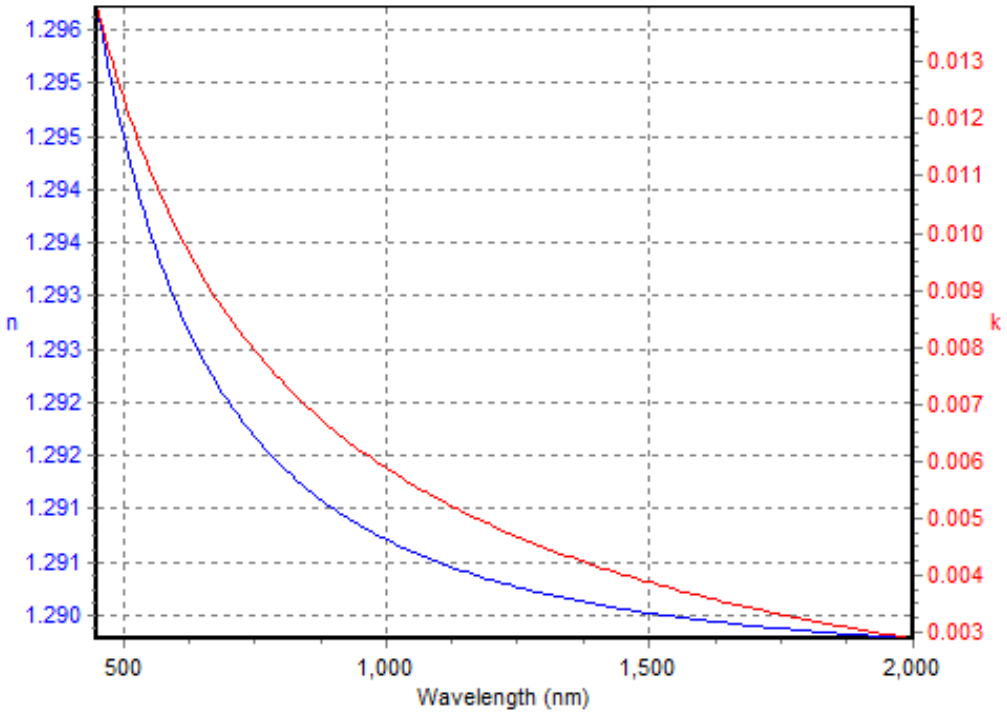

Figure 2-14. The refractive index of the zinc oxide nanostructure obtained by measurement and fitting.

2.5.1.4 Silicon Dioxide

Ellipsometry was performed on the prepared SiO_2 samples. Samples with seven different concentrations of Pluronic F-127 were prepared. The following concentrations of tetraethyl orthosilicate to Pluronic F-127 to 37%HCl to ethanol were used to provide SiO_2 refractive indices in increasing order, 1:0.0084:6.8:51.2, 1:0.0122:8:54.3, 1:0.0149:10.28:63.3, 1:0.0066:4.57:49.74, 1:0058:3.99:49.74, 1:0.0051:3.43:45.22, 1:0.0045:2.86:45.22. The films were deposited on silicon wafer with an estimated native oxide layer of 4nm between the silicon wafer and the SiO_2 films. The thickness of the films were on average ~100nm. The procedure for obtaining the refractive indices was similar to the one followed for the previous oxides. Materials files included with the Ellipsometer software were used to represent the SiO_2 layer, described by the Lorentz single

oscillator model. Bruggeman's effective medium theory was used to characterize the porosity. Refractive index variations down to approximately 1.17 were obtained.

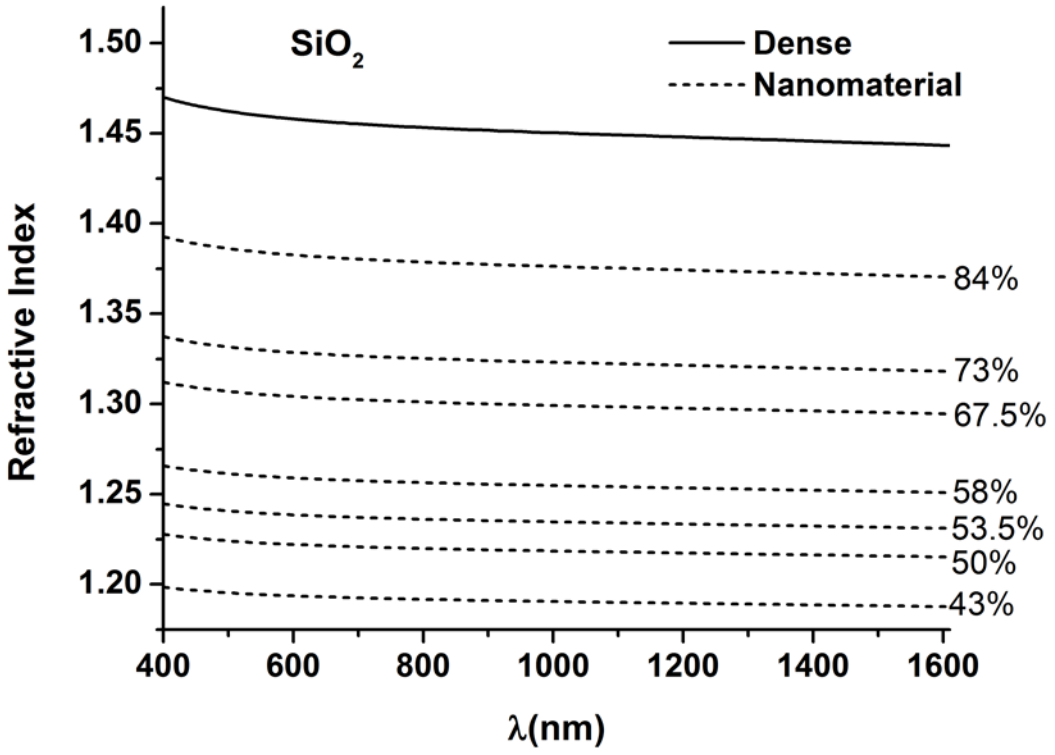

Figure 2-15. The refractive indices of the SiO_2 nanostructures obtained by measurement and fitting.

2.5.2 Annealing Temperature Dependence of the Refractive Index

As discussed in a previous section, the removal of the block-copolymer at lower temperatures (<400C) may pose structural instability and may promote structural collapse at higher temperatures where some degree of crystallization takes place (>500C). An experiment was carried out to examine the effect of the annealing temperature on the refractive indices for TiO_2 (Figure 2-16).

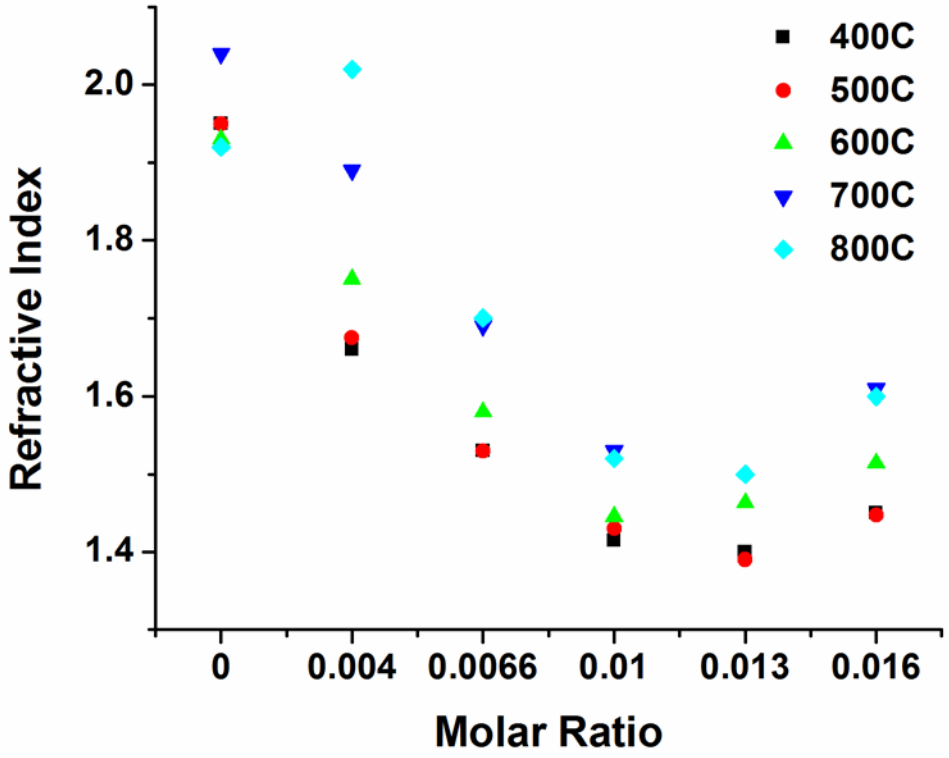

Figure 2-16. Variation in the refractive indices of the TiO_2 nanomaterials annealed at various temperatures as a function of the molar ratio between Pluronic F-127 and Titanium.

There seems not to be a difference in the refractive indices between samples annealed at 400C and 500C. Samples annealed at 600C show an increase in the measured refractive indices, in general. Further increase is noted for samples annealed 700C and 800C. In general, samples annealed at 700C have similar refractive indices to samples annealed at 800C. A more substantial change was expected in the refractive indices between samples annealed at 400C and 800C, given information provided in publications. These results suggest that there will be some degree of structural collapse and densification in the current nanomaterials, but not to a great extent.

2.5.3 Nanostructure Visualization

2.5.3.1 Titanium Dioxide

Scanning electron imaging (SEM) and transmission electron imaging (TEM) we performed on some of the selected samples in order to attempt to examine the features at the ~20nm scale. Due to the scale of the expected features, SEM imaging provided useful images only for a few samples, mainly ZnO, but can be used to examine the porosity on the large scale. SEM imaging would ideally be preferred and this is because it does not require extensively modifications to the preparations methods as one needs to perform for TEM analysis. TEM analysis can be readily used for analyzing features on the 20nm scale but the obtained images representative of the sample prepared for TEM analysis may not be representative of a typical sample.

To examine the underlying structure that is formed by templating with Pluronic F-127 for TiO_2, transmission electron microscope images were obtained. The TiO_2 precursors were deposited on silicon nitride TEM grids, with silicon nitride film thickness of 50nm, containing 9 windows of 0.1x0.1mm. The precursor were spin cast onto the TEM grids with spin speeds of 4K RPM to provide nanomaterials thicknesses of ~50nm. Two Pluronic F-127 concentrations were examined in an attempt to try to uncover the mechanism that results in variations in the refractive index. The two concentrations examined were Ti-3-1:0.01:1.12:5:30.4 and Ti-4 1:0.013:1.43:5.64:31.58. In addition, after spin coating the TEM samples were placed in an oven at 60°C for a hydrothermal treatment.

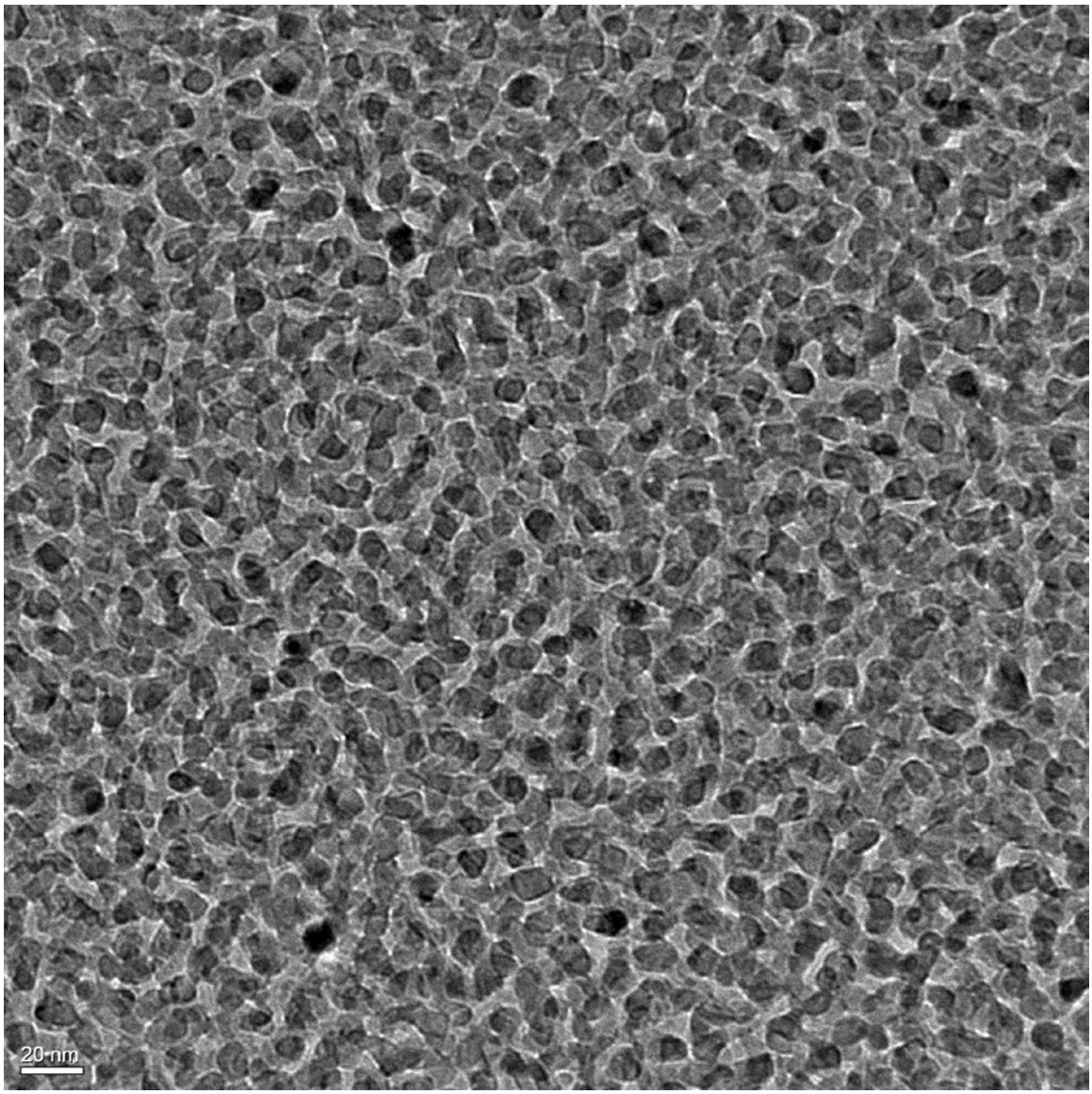

Figure 2-17. Bright field Transmission Electron Microscope image of a TiO_2 sample showing a high degree of film porosity. The precursor concentration used in obtaining this image is Ti-4.

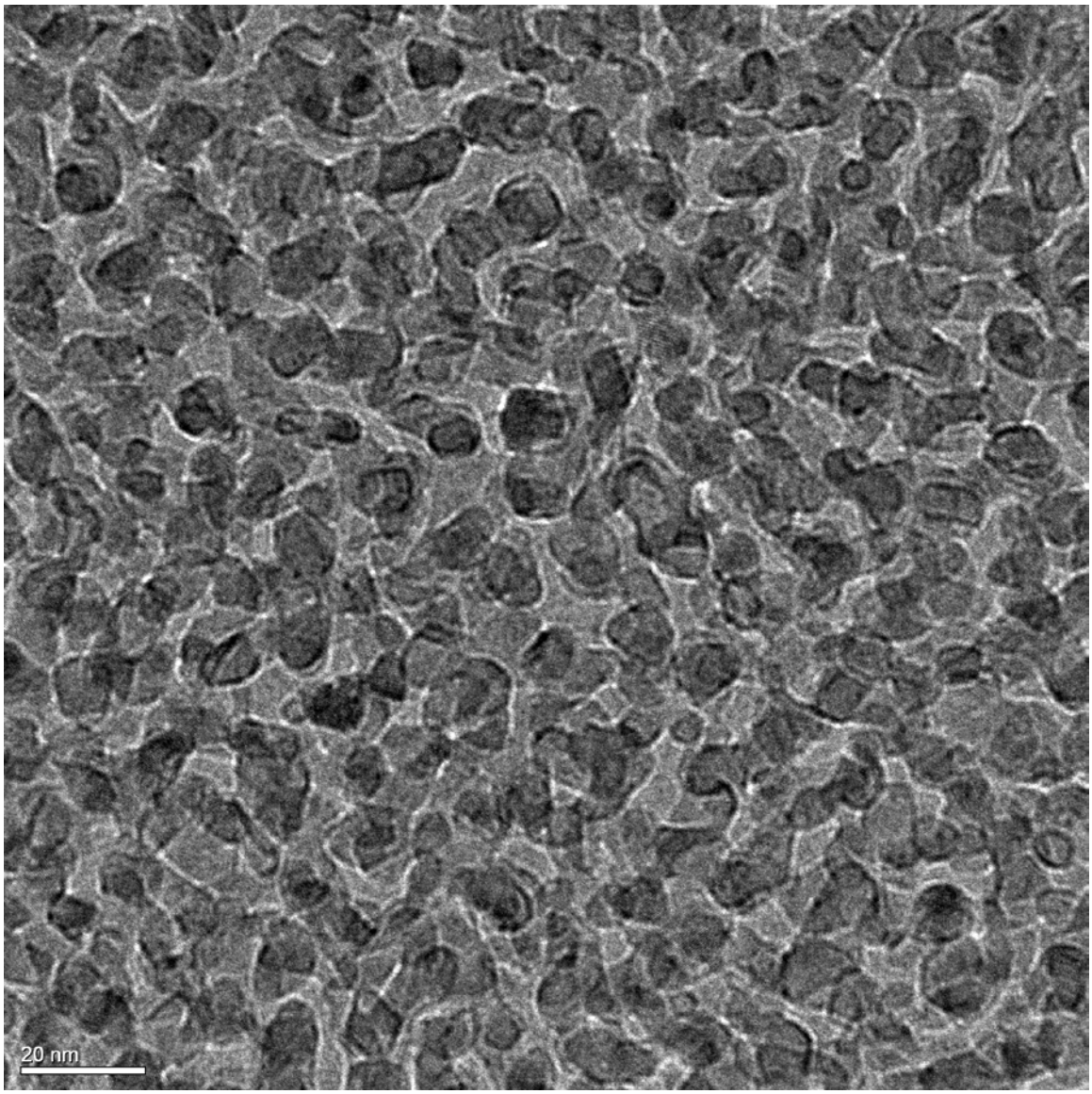

Figure 2-18. Magnified bright field Transmission Electron Microscope image of the same TiO_2 with precursor concentration of Ti-4. The size of the TiO_2 features appear to be <10nm.

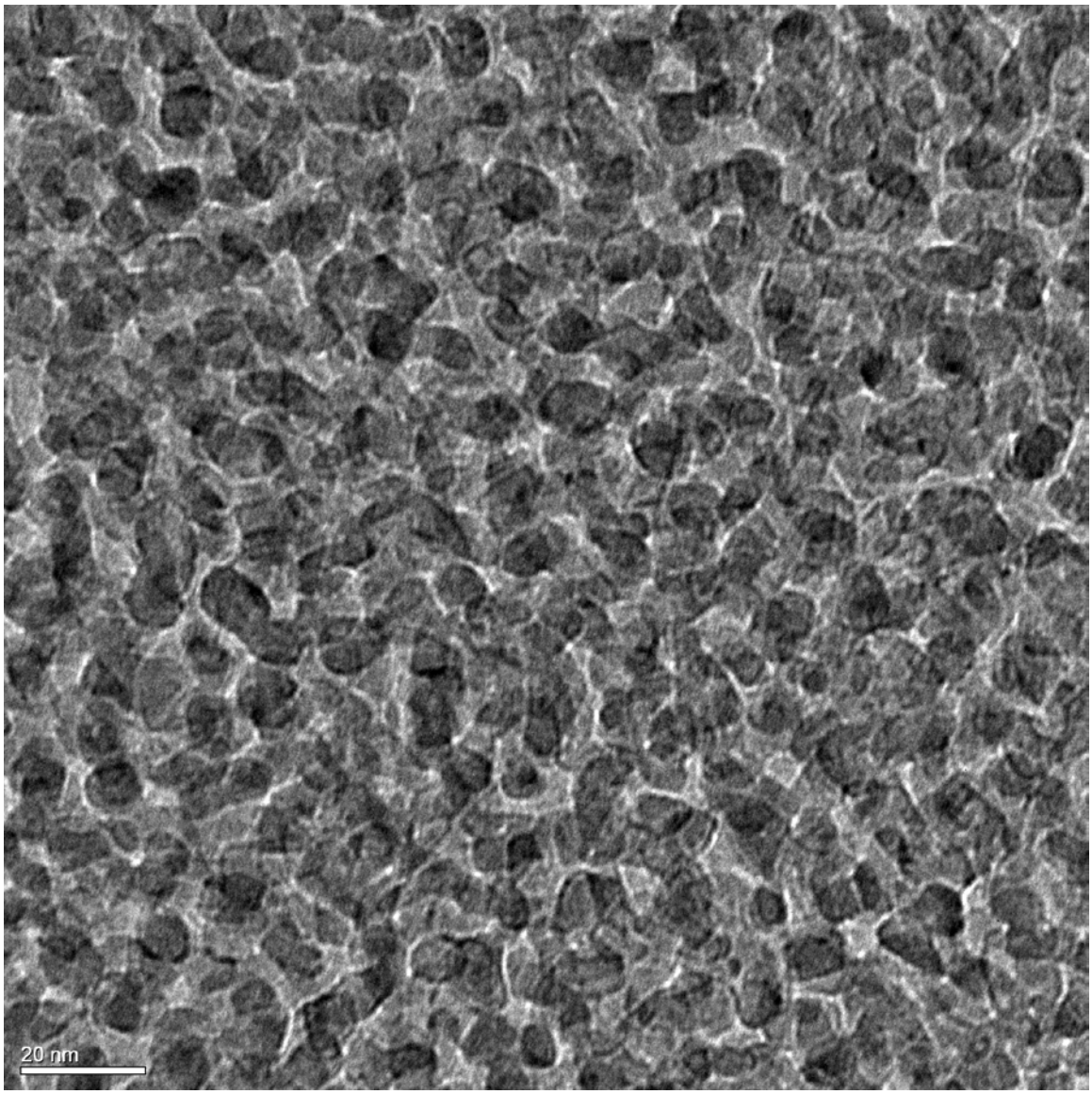

Figure 2-19. Magnified bright field Transmission Electron Microscope image of another TiO_2 sample. The precursor concentration used in obtaining this image is Ti-3.

The two concentrations of TiO_2 examined provide substantial differences in refractive indices. The concentration of Ti-3 (1:0.01:1.12:5:30.4) provides a refractive index of ~1.6 and of Ti-4 (1:0.013:1.43:5.64:31.58) provides a refractive index of ~1.4. In comparing the TEM images for these two concentration, some subtle differences can be noted. It may be argued that the size of

the particles in the precursor with a higher concentration of Pluronic F-127 are smaller, but not with certainty. A previous report suggested that the variations in the refractive index are from changes in the distribution density and size of the micelles formed when templating with Pluronic F-127[26]. Therefore, more study needs to be performed to uncover the mechanism.

2.5.3.2 Tin Dioxide

The analysis performed for SnO_2 was a combination of transmission electron and scanning electron imaging. A prepared SnO_2 nanomaterial coating on fiber was section with focused ion beam (FIB) and lifted out. A protective layered of platinum was deposited on the film prior to sectioning. A tungsten probe tip was used to lift the sectioned film out and electron transparency was obtained over a 10μm wide region.

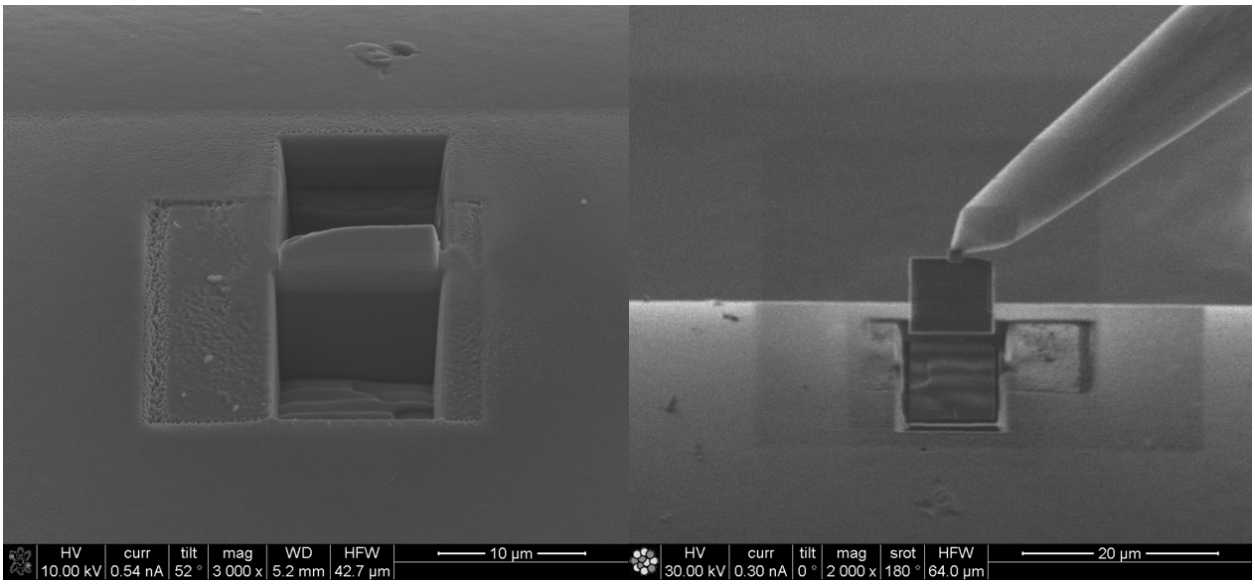

Figure 2-20. Left: Scanning electron microscope image of the sectioned nanomaterial film deposited on optical fiber. **Right:** Image showing the lift-out with a tungsten probe tip.

A scanning transmission electron microscope image using a high angle annular dark field detector was used to image the cross section of the film. A high degree of porosity is clearly visible. A bright field TEM image shows the average particle size, which is on the order of 5-10nm. Dark circular shapes can be observed, indicative of the tin dioxide nanoparticles.

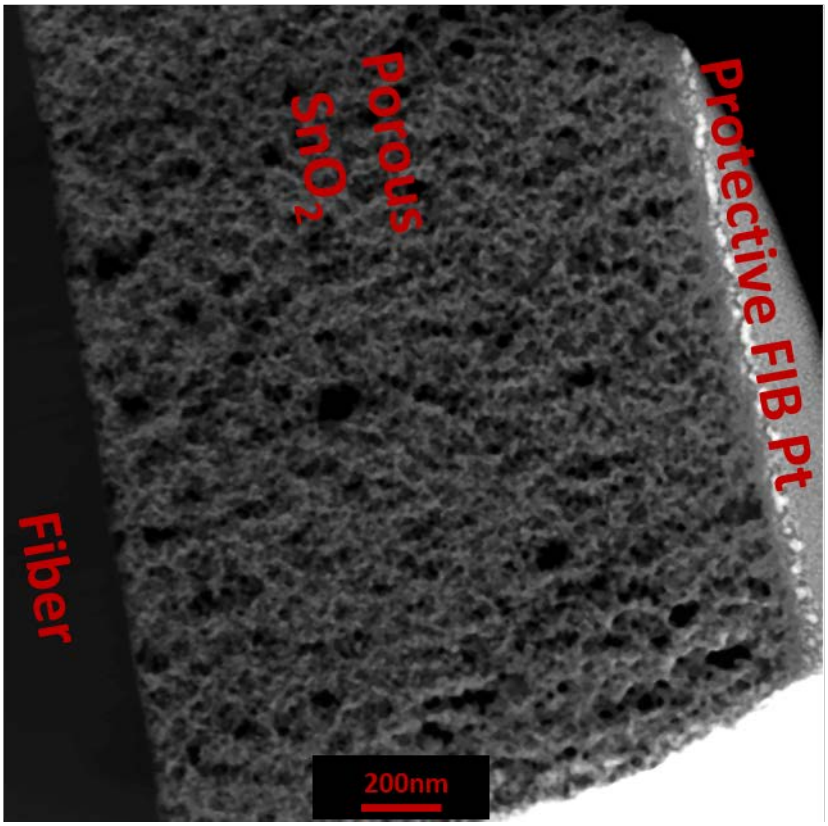

Figure 2-21. Cross sectional scanning transmission electron microscope image of the SnO_2 film using a high angle annular dark field detector. The obtained image shows a high degree of film porosity.

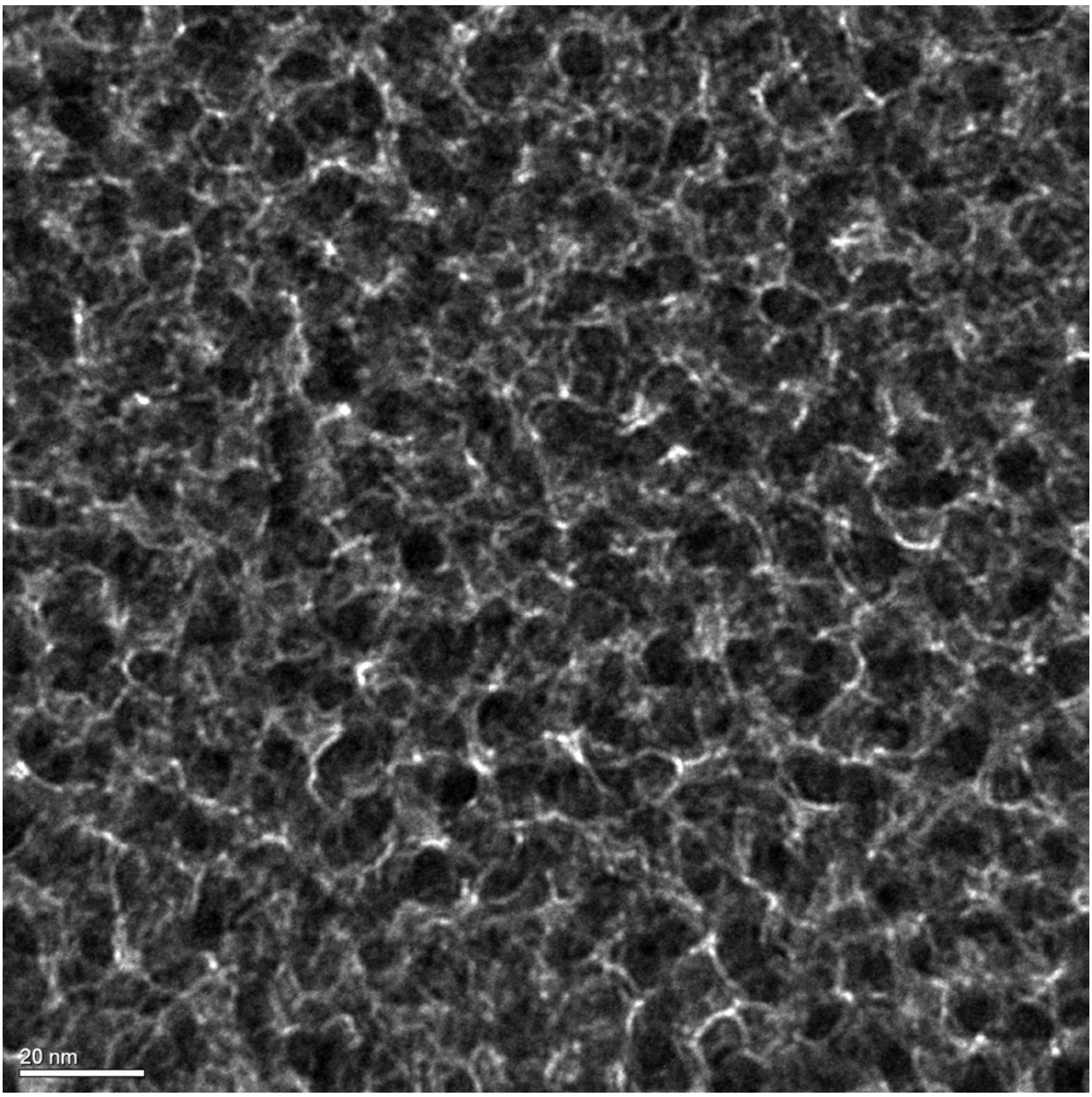

Figure 2-22. Bright field TEM image illustrating an average SnO_2 particle size of approximately 10nm with a large degree of porosity.

2.5.3.3 Zinc Oxide

Figure 2-24 shows an SEM image obtained from analyzing the surface of a prepared ZnO sample deposited on silicon wafer. A large degree of porosity is clearly visible, a characteristic of the very low refractive index measured. In acidic environments it is know that Pluronic F-127 usually forms spherical micelles. In this case, being a highly basic environment, the underlying shape the block copolymer assumes is unknown. Since an SEM image shows the surface features as opposed to a TEM showing the inner structure, it is more difficult to determine the structure from an SEM image. Surfaces most often deteriorate and deform and hide the underlying structure.

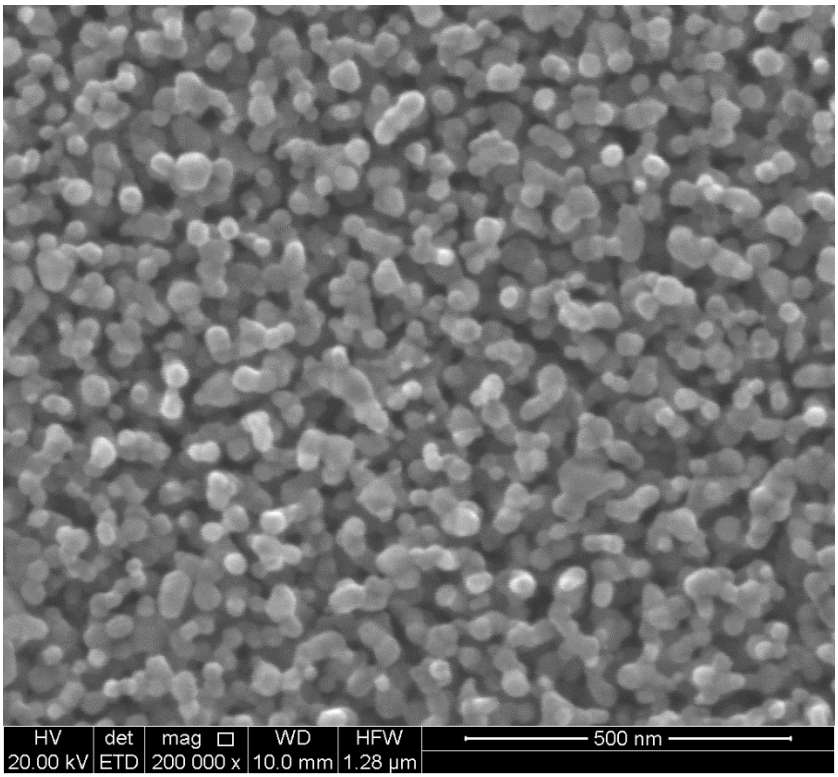

Figure 2-23. SEM image of the resultant ZnO nanomaterial indicating some complex underlying structure with features on the order of 50nm or less.

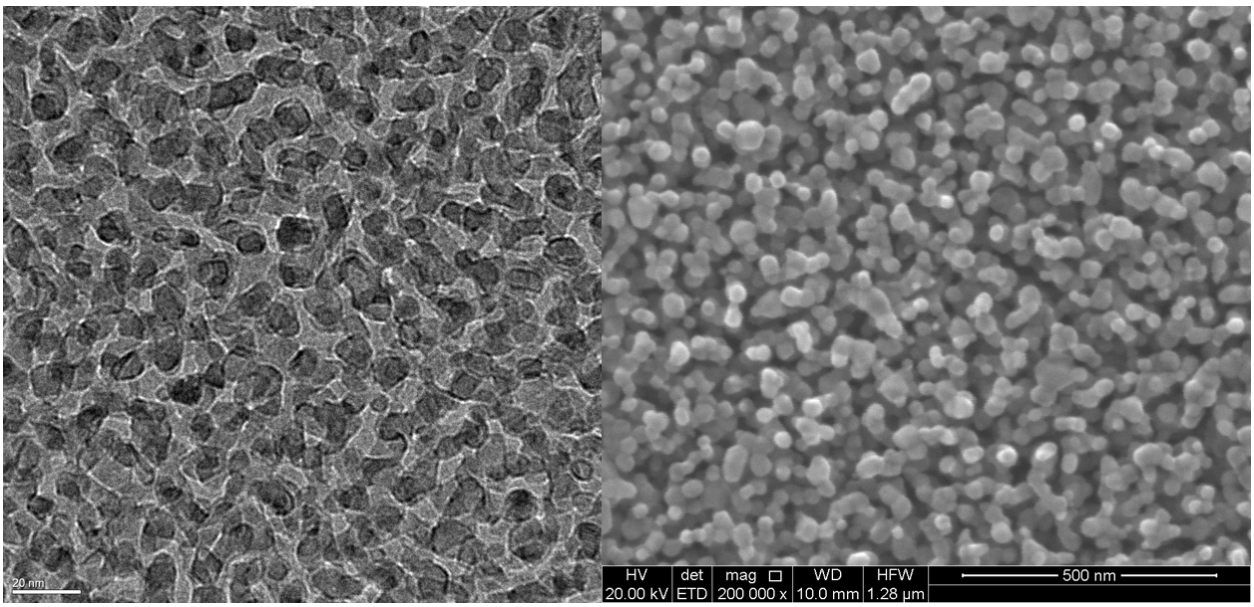

Figure 2-24. Images placed side by side for comparison of a **Left:** TEM image of the TiO_2 nanomaterial and **Right:** SEM image of a ZnO nanomaterial.

It is interesting to compare the SEM image of the ZnO nanomaterial with that of the TiO_2 nanomaterial obtained by TEM (Figure 2-24). With bright field TEM imaging, it is expected that air would appear bright, while TiO_2 should appear darker. Therefore, in the TEM image, lighter gray regions correspond to air and darker gray circles correspond to TiO_2 nanoparticles. With SEM imaging, the opposite is expected in this case. That is, the material should be bright, while air regions should be dark. Therefore, these two images placed side by side should have an inverse relationship. Keeping this in mind, these two images compare to one another reasonable well and complement one another. With this analysis, it is reasonable to assume that the acidic formulation of the precursor for TiO_2 and SnO_2 provide similar structure formation to the basic formulation of the ZnO precursor solution.

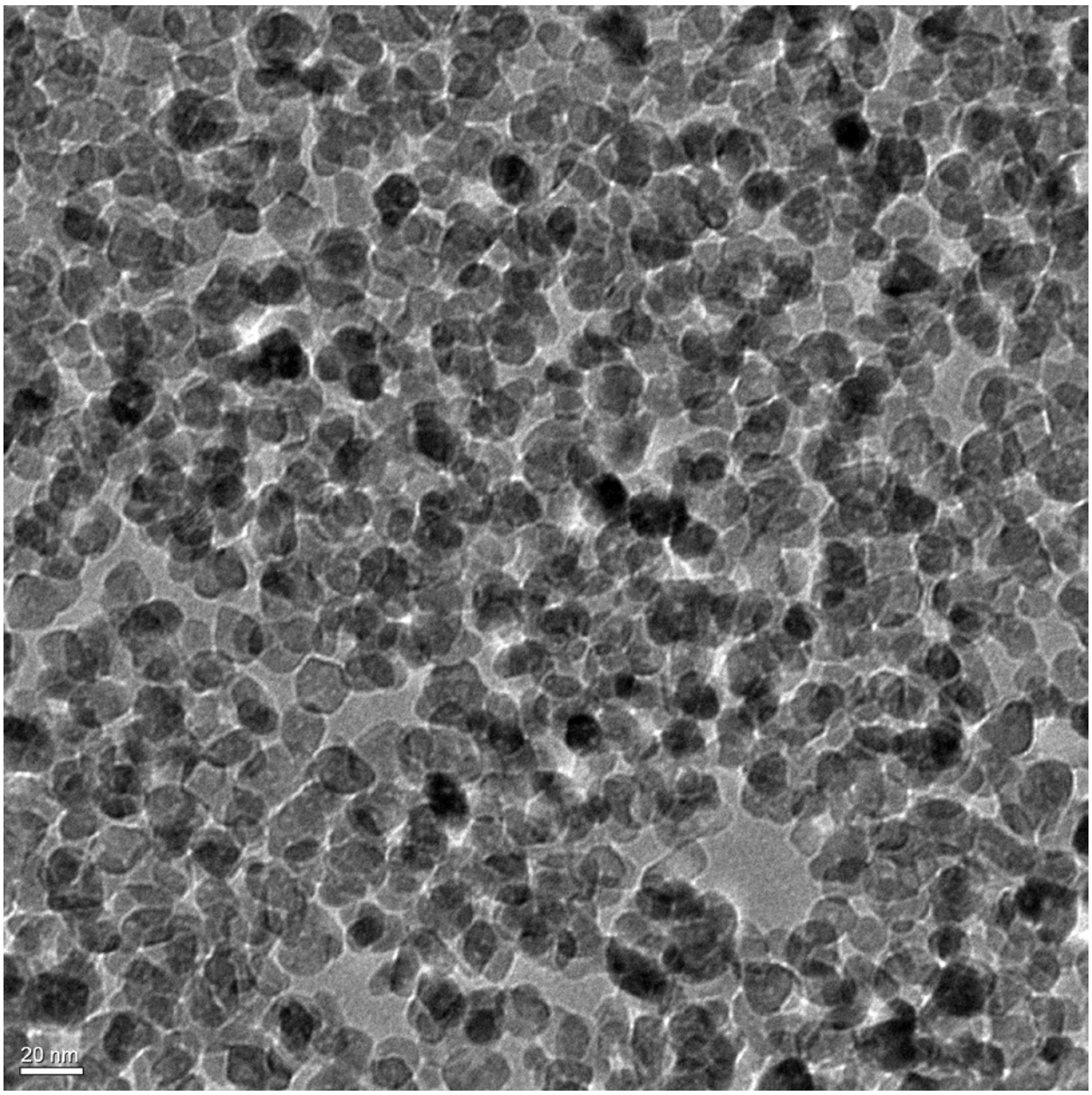

Figure 2-25. Bright field TEM image illustrating an average ZnO particle size of approximately 15-20nm with a large degree of porosity.

A TEM image of the formed ZnO nanostructure was obtained. The image confirms a structure similar to that of TiO_2 but with features sizes in the ~20nm range, with a high degree of porosity.

2.6 CONCLUSIONS

In this section the engineering of the refractive indices of important functional materials was demonstrated. Refractive indices of functional metal oxides such as TiO_2 and SnO_2 were controlled down to such low values as 1.4. Whereas, a ZnO nanomaterial with a very low refractive index of ~1.3 was obtained by developing a novel precursor solution, as such nanostructures of ZnO were not found in prior publications. The capability of the method developed to engineer the refractive index of another important oxide, SiO_2, was well demonstrated, with refractive index tunability down to ~1.17. The importance behind the capability to engineer the refractive index of SiO_2 will be shown in the section dealing with anti-reflection coatings realized by low-index nanomaterials.

The method adopted to manipulate the optical properties of the demonstrated materials by 3D sub-wavelength engineering on the <50nm scale, namely block-copolymer templating by the use of Pluronic F-127, was well suited for the task. Before demonstrating the developed method, the theoretical foundation was laid out and the obtained results agree well with what was expected. As noted earlier, the variations in the refractive indices are thought to be due to the size and density variations of the micelles formed by Pluronic F-127. TEM analysis of nanomaterials that present significant differences in their refractive indices could not confirm this hypothesis.

TEM imaging of such nanomaterials is a difficult task. The films prepared for TEM imaging were ~50nm in thickness which, considering the underlying structure, would consist of only ~3 or so material layers. The conditions under which the samples were prepared did not seem to provide good enough quality as to preserve the structure in enough detail to allow the visual confirmation of the mechanism behind the variations in the refractive indices. This type of an analysis would most likely require precursor and sample preparations under much more careful conditions, preserving the features and the shapes enough to visually confirm size and density variations in the nanomaterials. Despite this, the refractive indices of the examined materials varied significantly from their nominal values. Therefore, the presented method can in such simple conditions as presented here, free of expensive equipment such as sputtering, e-beam evaporation, and chemical vapor deposition, be used to produce high optical quality films. It is a good inexpensive method to effectively manufacture optical materials with refractive indices not available in nature. With the demonstrated method, it is very reasonable to assume that optical materials with refractive indices of any value between 2.2 and 1.17 can be easily manufactured.

3.0 NANOMATERIAL ANTI-REFLECTION COATINGS

3.1 BACKGROUND

In optics and photovoltaics the amount of light that gets reflected from a surface is of practical importance. The propagation of light in different materials is governed by the index of refraction, which, in general, is a complex quantity. At the interfaces of two materials with different refractive indices reflections take place and these in most practical cases, are unwanted effects. In optical components such as lenses, these reflected components can be of significant importance due to losses in power and, not to mention, the distortions caused by reflections for imaging applications. In photovoltaics, reflections mean the loss of incoming light which may be converted into electrical energy, such as in solar cells.

Recent advances have made considerable reductions in the kW h of the energy produced by solar cells, initiating a surge in the exploration of solar energy. Crystalline silicon solar cells make up over 90% of the commercial solar cell market [37, 38], and one of the major efficiency drains is light losses due to reflections. The typical operating wavelength range of silicon solar cells is between 400-1100nm, and a polished single crystal silicon surface reflects about 38% of the light in this range, on average. The convention is to use a single layer quarter wavelength ($\lambda/4$) anti reflection of either TiO_2 or Si_3N_4. These coatings reduce reflections to about 18% and that is at normal incidence, and they typically have a minima at a single wavelength. Considerable research effort has been devoted to tackling the issue of anti-reflection coating [39-43]. Surface texturing has been developed to further reduce these reflections to about 13%. A variety of methods have been explored from the catalytic sol-gel process[44], nano-arrays [39, 40, 45], sub-

wavelength surface structures [46-48], lithography and wet etching [49], a combination of oblique angle deposition with sputtering techniques [50-52], to anodic alumina [53].

The difficulty in manufacturing broadband and omni-directional good anti reflection coatings lies in the fact that nature did not provide us with materials that have a continuum of refractive indices. That is, we cannot simply find a material with any refractive index we want, therefore concessions have to be made when it comes to designs. An ideal anti reflection coating is one that gradually changes its refractive index from the refractive index of silicon to that of air. Several studies have examined the shape of the gradients and their associated reflectivity [52, 54]. Several of the demonstrated methods overcome this lack of refractive index availability by nanostructuring in the sub-wavelength regime.

The idea of changing the refractive indices of materials is not new, it dates back to the Clusius-Mossotti relation and the Maxwell-Garnett effective medium theory and later to Bruggeman's effective medium theory[19]. These theories described changing a material's optical properties simply by mixing two different materials together on a scale that is much less than the wavelength of light. In the past two decades, our ability to manipulate materials three-dimensionally on the <50nm scale, has evolved substantially. Many of the demonstrated highly efficient anti reflection coatings work on the principle of realizing approximations to the ideal refractive index gradients that would yield the best broadband and wide angle anti reflection coatings. And, they do this by structuring materials on the sub-wavelength scale to alter their optical properties [50, 52, 53]. In nature, there are no materials with refractive indices below 1.38 and these methods have demonstrated the manufacture of SiO_2 with a refractive index of 1.05. Although, these method have demonstrated such novel refractive index capabilities and highly efficient anti reflection coating, they require complex manufacturing schemes that may be too

expensive and restrictive for industry to adopt. Therefore, alternative low cost approaches are needed.

In this section, the method of block-copolymer templating is applied to address the issue of cost and the complications associated with the demonstrated methods. An exploration of the feasibility of using block-copolymer templating coupled with a low cost solution processing approach is presented. The design of the anti-reflection coatings is achieved by genetic algorithms and simulated annealing algorithms coupled with the rigorous transmission matrix theory to arrive at optimal designs. Two layer anti reflection coatings with 3% average broadband and omni-directional reflectivity is demonstrated. With further developments in the proposed method, by extending the current refractive index engineering limits, anti-reflection coatings with an increased number of layers resulting in a lowered reflectivity, can potentially be achieved for crystalline silicon. Although not shown here, an increased number of layers with more efficient anti-reflective properties for substrates such as aluminum nitride, that have lower refractive indices, could be obtained with the demonstrated method.

3.2 THEORY

The optimal refractive index profiles needed to achieve the lowest reflectivity requires materials with continuous strong refractive index gradients, and the manufacture of such materials until today has not been demonstrated. Therefore, to approximate these theoretical models, these continuous functions can be discretized and approximated by an arbitrary number of layers. The light transmission and reflection properties of a stack of material layers is explored here. In the following, the main equations are shown without going through the derivation. The derivations

can be found elsewhere[55]. The basic approach is to define the wave equation and solve it by the separation of variables with the appropriate boundary conditions.

Let's start by examining a homogenous dielectric film. In this case the permittivity ε, the permeability μ, and the refractive index n are all constant. If we define the z-axis to be perpendicular to the homogenous film, then θ is the angle that the wave makes with respect to the z-axis and we have $\alpha = n\sin(\theta)$. For a TE plane wave, the following differential equations need to be solved, where U and V are field functions.

$$\begin{cases} \frac{d^2U}{dz^2} + (\boldsymbol{k_o}^2\boldsymbol{n^2cos^2U} = \mathbf{0} \\ \frac{d^2V}{dz^2} + (\boldsymbol{k_o}^2\boldsymbol{n^2cos^2V} = \mathbf{0} \end{cases}$$

Equation 3-1

The solutions of these equations are

$$\begin{cases} \boldsymbol{U(z) = Acos(k_o nzcos\theta) + Bsin(k_o nzcos\theta)} \\ \boldsymbol{V(z) = \frac{1}{i}\sqrt{\frac{\varepsilon}{\mu}}\cos\theta[Bcos(k_o nzcos\theta) - Asin(k_o nzcos\theta)]} \end{cases}$$

Equation 3-2

In enforcing the boundary conditions we get the following in matrix form, with $\rho = \sqrt{\frac{\epsilon}{\mu}\cos\theta}$

$$\boldsymbol{M(z)} = \begin{bmatrix} \boldsymbol{cos(k_o nzcos\theta)} & \boldsymbol{-\frac{i}{\rho}sin(k_o nzcos\theta)} \\ \boldsymbol{-i\rho sin(k_o nzcos\theta)} & \boldsymbol{cos(k_o nzcos\theta)} \end{bmatrix}$$

Equation 3-3

In the case of TM waves, we just simply have to replace ρ with q, q being

$$\boldsymbol{q} = \sqrt{\frac{\boldsymbol{\mu}}{\boldsymbol{\varepsilon}}\boldsymbol{\cos\theta}}$$

Equation 3-4

In the preceding the characteristic matrix for an interface between two materials was described. Now, if we have a number of thin films stacked on top of one another, obtaining the characteristic matrix is a simple manner of developing the characteristic matrix for each material and multiplying

them together. Therefore, if we have N layers of thin films, the characteristic matrix for the overall system is

$$\boldsymbol{M(z_N) = M_1(z_1)M_2(z_2 - z_1) \ldots \ldots M_N(z_N - z_{N-1})} \qquad \textbf{Equation 3-5}$$

To obtain the transmitted and reflected components of the incoming light, a bit more work is needed. Let's suppose that the stack starts at z=0 and ends at z = z_N and this stack is bounded on each side by semi-infinite media. Let's define E_o as the incident amplitude, R as the reflected amplitude, and T as the transmitted amplitude. The stack has a first layer and a last layer with ε_1 μ_1 and ε_N μ_N representing the permittivity and the permeability, respectively. The incoming wave will be incident at an angle of θ_1 and the transmitted wave will have an angle of θ_N with respect to the z-direction. Given these, the transmission and reflection coefficients can be written as, where the m_{ij} are the components of the overall characteristic matrix[55].

$$\mathbf{r} = \frac{(\mathbf{m_{11} + m_{12}\rho_N})\boldsymbol{\rho_1} - (\mathbf{m_{21} + m_{22}\rho_N})}{(\mathbf{m_{11} + m_{12}\rho_N})\boldsymbol{\rho_1} + (\mathbf{m_{21} + m_{22}\rho_N})} \qquad \textbf{Equation 3-6}$$

$$\mathbf{t} = \frac{\mathbf{2\rho_N}}{(\mathbf{m_{11} + m_{12}\rho_N})\boldsymbol{\rho_1} + (\mathbf{m_{21} + m_{22}\rho_N})} \qquad \textbf{Equation 3-7}$$

Given that we have the transmission and reflection coefficients, the transmissivity and the reflectivity can be obtained as follow

$$\mathbf{R} = |\mathbf{r^2}| \qquad \textbf{Equation 3-8}$$

$$\mathbf{T} = \frac{\boldsymbol{\rho_N}}{\boldsymbol{\rho_1}}\left|\mathbf{t^2}\right| \qquad \textbf{Equation 3-9}$$

3.3 EXPERIMENT

3.3.1 Designing the Anti-Reflection Coatings

The refractive index of crystalline silicon is about 3.4 and the refractive index of air is roughly 1. This large index difference results in about a 38% reflection of the incoming light on average in the 400-1100nm range over a range of angles from 0-80°. Ideal anti reflection coatings previously theoretically demonstrated such as the gradient index quantic profile is too difficult to manufacture with today's technology and therefore, approximations need to be used. Instead of having a single material layer whose refractive index continuously varies from that of silicon to that of air, several layers can be used with distinct refractive indices.

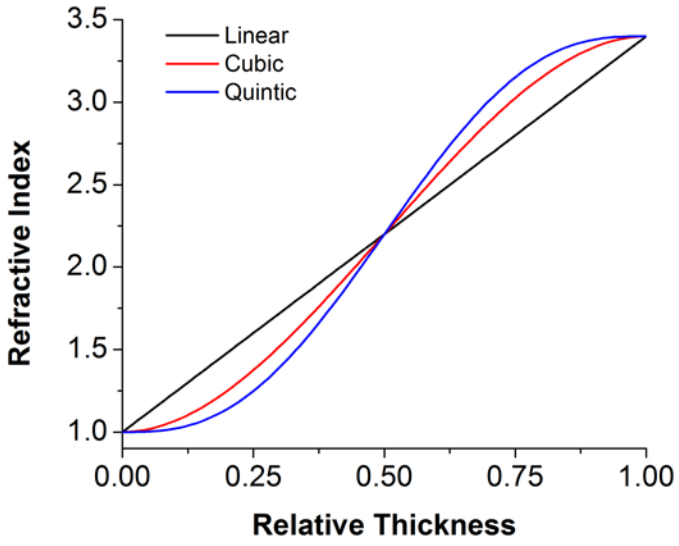

Figure 3-1. Various refractive index profiles for minimizing the reflections of a silicon substrate in air. The quantic profile is the one with a reflectivity R<1% over the entire visible spectrum[54].

The question is, how should one go about choosing the thickness of each layer and its refractive index to minimize the amount of the reflected light given a wavelength range and angular span? This has been explored before by several groups that used the transfer matrix approach in conjunction with advanced minimization techniques such as the genetic algorithm [56], simulated annealing algorithm [57], and the ant colony algorithm[58].

The idea is to put all the concept together and examine the optimal reflectivity of various anti-reflection coatings that are possible to make with our developed method of block copolymer templating. The design of the anti-reflection coatings here is accomplished by using the transfer matrix method coupled with the genetic algorithm and the simulated algorithm. A matlab code was developed that implements the transfer matrix method and can be used to solve for the reflectivity of a multilayer film on a silicon substrate. The genetic algorithm and the simulated annealing algorithm is built into matlab and was coupled with the developed transfer matrix algorithm. Due to horizon effects which limit the angular spread of sunlight to 75° on either side of the normal to the surface of the earth, there is no need to consider angles beyond this.

In preparation of carrying out the design, material optical properties were gathered from literature and confirmed experimentally by Ellipsometry[34-36]. Given that we are interested in creating a discretized refractive index gradient from the silicon surface (index ~3.4) to air (index ~1), a combination of the TiO_2 and SiO_2 was chosen. TiO_2 is a good choice since it can have a relatively high value for the refractive index for an oxide, can be around 2.6 depending on the preparation conditions. The high index of TiO_2 will allow us to get close to the refractive index of the substrate. SiO_2 is a good choice because it has a relative low refractive index in comparison and will allow us to get close to the refractive index of air.

Functions were fit to the real and imaginary parts of the refractive indices in the 400-1100nm range, with high quality of fits, generally with an R^2 value of 0.99 or higher. These functions were then used in the transfer matrix algorithm to account for the dispersive and absorptive properties of the materials. In setting up the algorithm, TiO_2 was chosen as the first layer that is in contact with the silicon substrate, followed by SiO_2 layer or layers, depending on the number of layers used.

Both the genetic algorithm and the simulated annealing algorithms are good at finding themselves out of local minima and are good choices for finding roughly the location where the minima occurs. These algorithms are generally coupled with other minimization techniques that can get more precise values of the minimums at the locations returned. The function evaluated to find the average reflectivity is the following

$$\mathbf{R_{avg}} = \frac{\mathbf{1}}{\boldsymbol{\Delta\lambda\Delta\theta}} \int_{\boldsymbol{\lambda_{min}}}^{\boldsymbol{\lambda_{max}}} \int_{\boldsymbol{\theta_{min}}}^{\boldsymbol{\theta_{max}}} \mathbf{w}(\boldsymbol{\lambda}, \boldsymbol{\theta}) \times \frac{\mathbf{R_{TE}}(\boldsymbol{\lambda},\boldsymbol{\theta}) + \mathbf{R_{TM}}(\boldsymbol{\lambda},\boldsymbol{\theta})}{\mathbf{2}} \mathbf{d\theta d\lambda} \qquad \textbf{Equation 3-10}$$

This function, representing the average reflectivity over an angular span and wavelength range, is a function of the wavelength, angle of incidence, polarizations, the refractive index, and the thickness of each layer. Although, not used for the demonstration presented here, the weighing function w in the R_{avg} function can be used to preferentially tune the reflectance with wavelength and angle. That is, to account for the intensity variations in the solar spectrum as a function of wavelength, or to account for variations in the internal quantum efficiency of solar cells as a function of wavelength, etc. With the genetic algorithm, these variables were minimized for the wavelength range of 400-1100nm and angular span of 0 to 75 degrees. The minimization was performed again with the simulated algorithm to ensure consistency of the found solutions. The table given below summarizes the results of the simulations. Here, the v_i are the volume fraction of the materials, the h_i are the thicknesses of the material thin films.

Table 3-1. Design results of the transfer matrix method coupled with the genetic algorithm and the simulated annealing algorithm for increasing number of layers. The percent fraction of the layer material with the corresponding film thickness are listed for an angular range of 0-75° and wavelength range of 400-1100nm.

Layers	0	1	2	3
v1		81.3%TiO_2	77.3%SiO_2	20%SiO_2
v2			100%TiO_2	99%SiO_2
v3				100%TiO_2
h1		88.45nm	125.759nm	223nm
h2			68.65nm	107nm
h3				68nm
Ravg	35%	13.60%	6.15%	4.70%

Figure 3-2 shows the average reflectance of crystalline silicon without any coating up to three layer anti-reflection coatings. The general trend is that the more layers are used in the simulation, the more it is required to have materials with refractive indices that approach the two boundaries, that of silicon (~3.4) and that of air (~1). For a three layer simulation, 20% SiO_2 is required to obtain an average reflectance of 4.7%. This corresponds to SiO_2 having a refractive index of 1.08 from its nominal value of ~1.45 at 800nm.

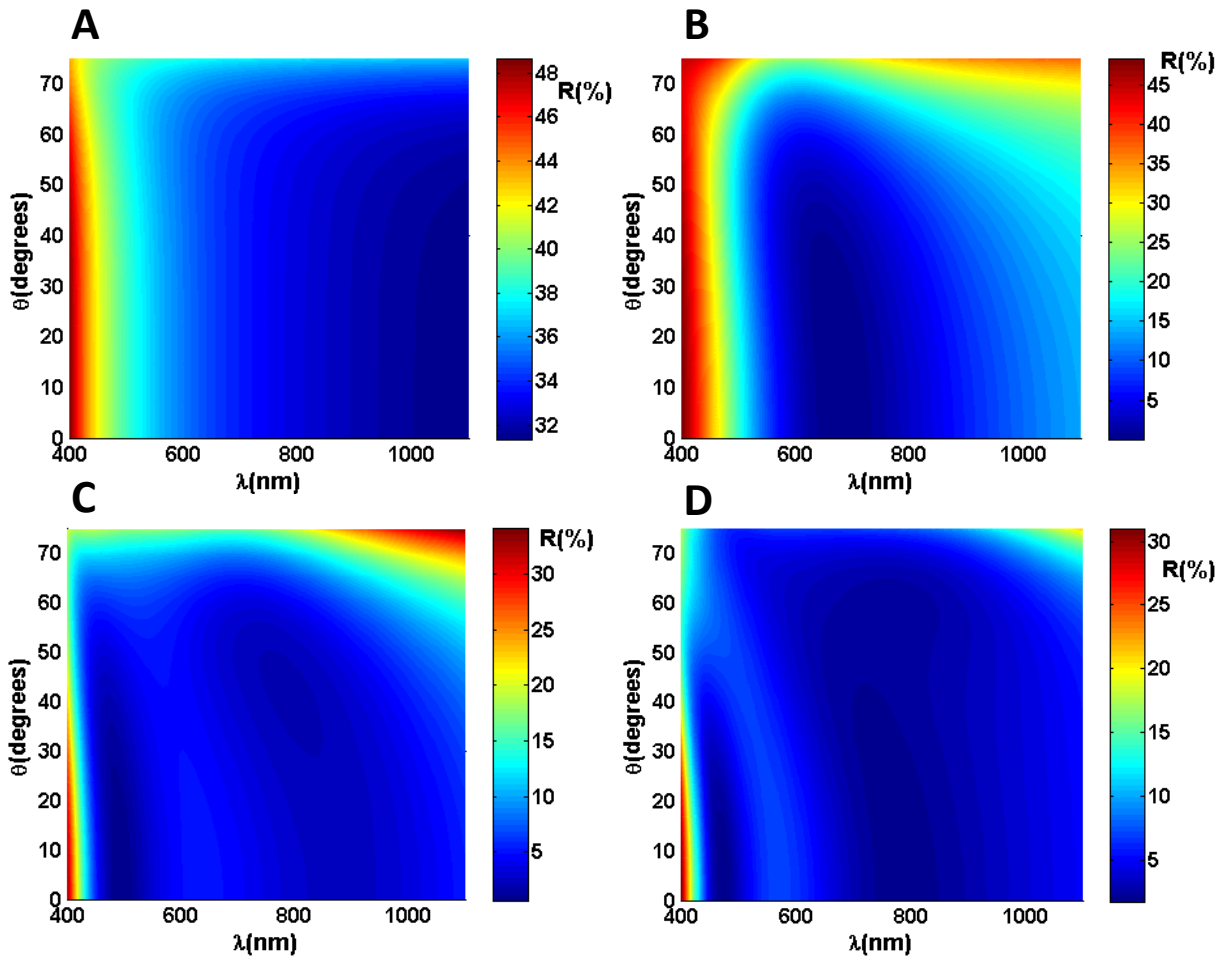

Figure 3-2. Simulation results using the genetic algorithm and the simulated annealing algorithm. **A.** Silicon reflectivity without AR coating, average R = 35%. **B.** One layer TiO_2 coating, average R = 13.6%. **C.** Two layer coating, average R = 6.15%. **D.** Three layer coating, average R = 4.7%.

With the currently chosen block-copolymer, there is a limit on how low the refractive index can be, given the current precursor ingredients and processing conditions. We have established a minimum volume fraction for TiO_2 and SiO_2 experimentally. The lowest volume fraction that we can achieve for TiO_2 and SiO_2 is 40%. These correspond to a TiO_2 refractive index of 1.4 and SiO_2 index of 1.17. In addition, we have a limited capability to measure the manufactured samples

due to light source and spectrometer limitations. Therefore, for practical purposes, a redesign was carried out for a limited wavelength and angular range of 400-700nm and 0-60 degrees.

Table 3-2. Design results of the transfer matrix method coupled with the genetic algorithm and the simulated annealing algorithm for increasing number of layers. With this simulation the current limits in refractive indices are included. The percent fraction of the layer material with the corresponding film thickness are listed for an angular range of 0-60° and wavelength range of 400-700nm.

Layers	0	1	2	3
v1		83.5%TiO_2	51.1%SiO_2	40%SiO_2
v2			100%TiO_2	73.7%SiO_2
v3				100%TiO_2
h1		63.94nm	112.7nm	200nm
h2			56nm	120nm
h3				57.4nm
Ravg	38%	6.64%	2.8%	3.60%

The table above shows the obtained design values for up to 3 layers. It is evident that given the current limits on the refractive index tunability, there is no benefit of coating more than 2 layers. If the index of TiO_2 can be made higher, and that of SiO_2 made lower, coating more layers will have improvements. In the minimization, each layer constitutes two variables, the index of the film and the thickness of the film. Therefore, a 3 layer film has 6 variables that represent thickness and refractive index. The refractive index is obtained by taking the materials complex refractive index and adjusting its value with Bruggeman's effective medium theory, which simply shifts the values of the indices up and down, leaving the shape of the dispersion intact. In addition, the minimizing function is then averaged over the spectral width and angular span of interest. The

returned value is then used as feedback to adjust the 6 variables to obtain a global minimum. The figure below shows the obtained designs with the practical restrictions applied in the minimization.

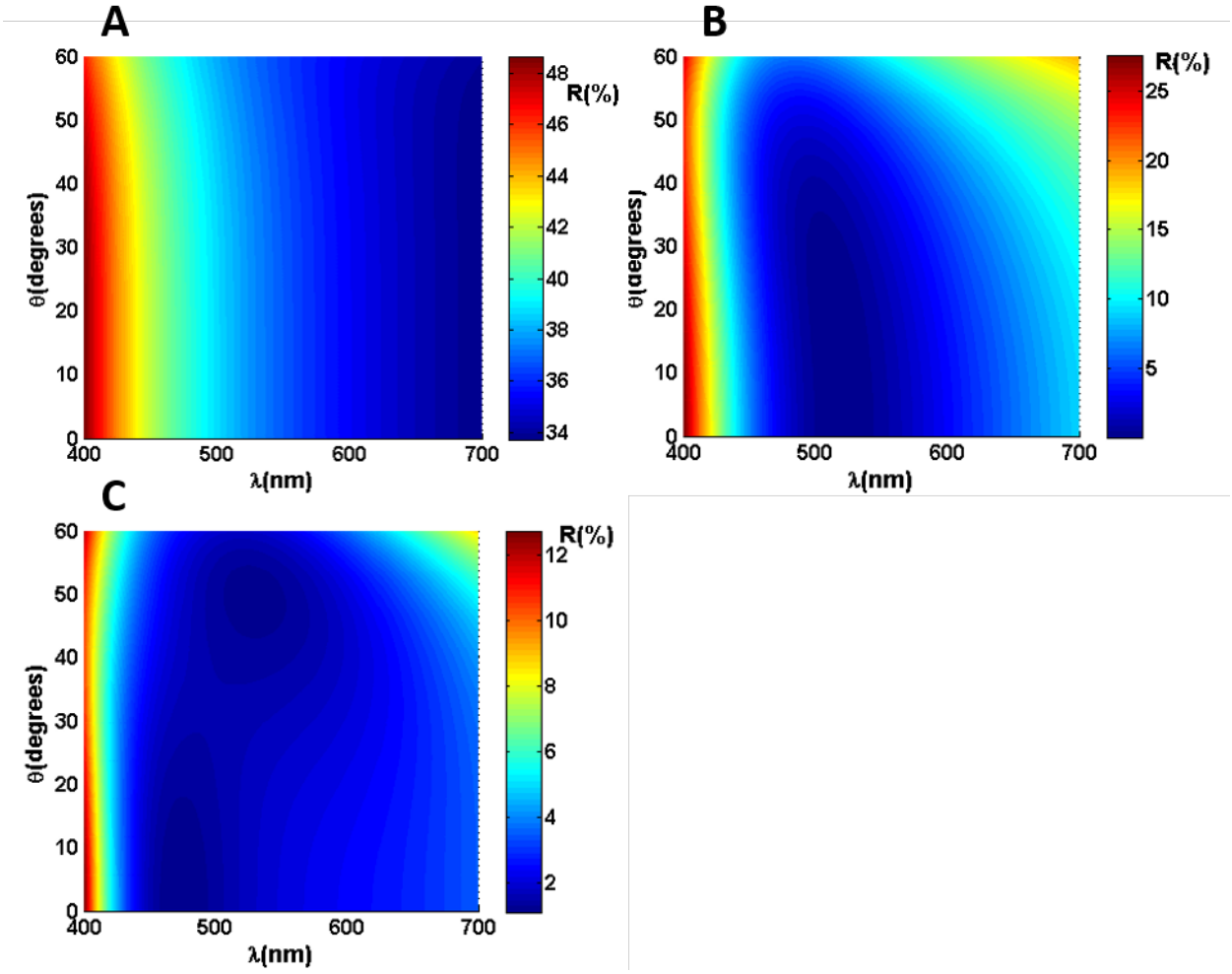

Figure 3-3. Simulation results using the genetic algorithm and the simulated annealing algorithm for the wavelength range of 400-700nm and angular range of 0-60°. **A.** Silicon reflectivity without AR coating, average R = 38%. **B.** One layer TiO_2 coating, average R = 6.64%. **C.** Two layer coating, average R = 2.82%.

3.3.2 Film Processing and Characterization

The solution for the preparation of dense TiO_2 consisted of titanium isopropoxide, monoethanolamine and 2-methoxyethanol in the following molar ratio 1:2:42.6. The refractive index of TiO_2 and SiO_2 can be altered by using block-copolymer templating, as described in more detail in the previous section.

Given that we now have design results for the thicknesses and the refractive indices of each layer, we can go ahead and manufacture them. Silicon wafers of orientation 100 were cut up into squares of 1 inch by 1 inch. These were subsequently cleaned with ethanol and dried by spinning for one minute at 5K RPM. To manufacture a one layer coating, a TiO_2 precursor solution providing the appropriate thickness was spin cast on the silicon substrate. Two methods are available to control the thickness of the film. How much solvent is used has a significant effect on the film thickness but it is difficult to control precisely. This method is used to roughly find the optimal value.

Controlling the spin coating speed can fine tune the acquired film thicknesses. For example, to manufacture a 75nm dense TiO_2 layer a precursor solution with molar ratio of 1:2:30, titanium isopropoxide to monoethanolamine to 2-methoxyethanol with a spin coating speed of 3000 RPM is used. To get the 75nm coating, two layers are spun and after each coating a drying step is used which consists of heating on a hotplate set to 300°C for 10 minutes. A two-step coating for dense TiO_2 ensures good film quality, since experimentally it is found that a one-step coating of 75nm TiO_2 does not provide good film quality.

Manipulating both the refractive index, which is a function of porosity, and the film thickness requires a bit more work. The general precursor consists of ethanol as the solvent, tetraethyl orthosilicate as the Si source, Pluronic F-127 as the block-copolymer, and 37% HCl as

the stabilizer. All these components are interdependent on one another and changing one will have an effect on the other, and in general the precursor has to be rebalanced by controlling the amount of HCl. For example, to make a 100nm SiO_2 film with a refractive index of 1.2 at the wavelength of 800nm, the molar ratio of tetraethyl orthosilicate to Pluronic F-127 to HCl to ethanol, 1:0.043:2.86:27 is used and spin cast at 2500 RPMs for 30 seconds.

After the successive layers have been deposited onto the silicon substrates, an annealing procedure is applied. The samples were placed in an oven at the center, to ensure uniform heating, and heated to 600°C at a rate of 1°C/minute. At 600°C the samples were held for 1hr and were cooled to room temperature at the same rate. After this, the samples were ready for analysis.

Measurements were carried out with a custom optical setup (Figure 3.4) composed of a white light source, optics to adjust the beam size and collimate the white light as much as possible, and a spectrometer.

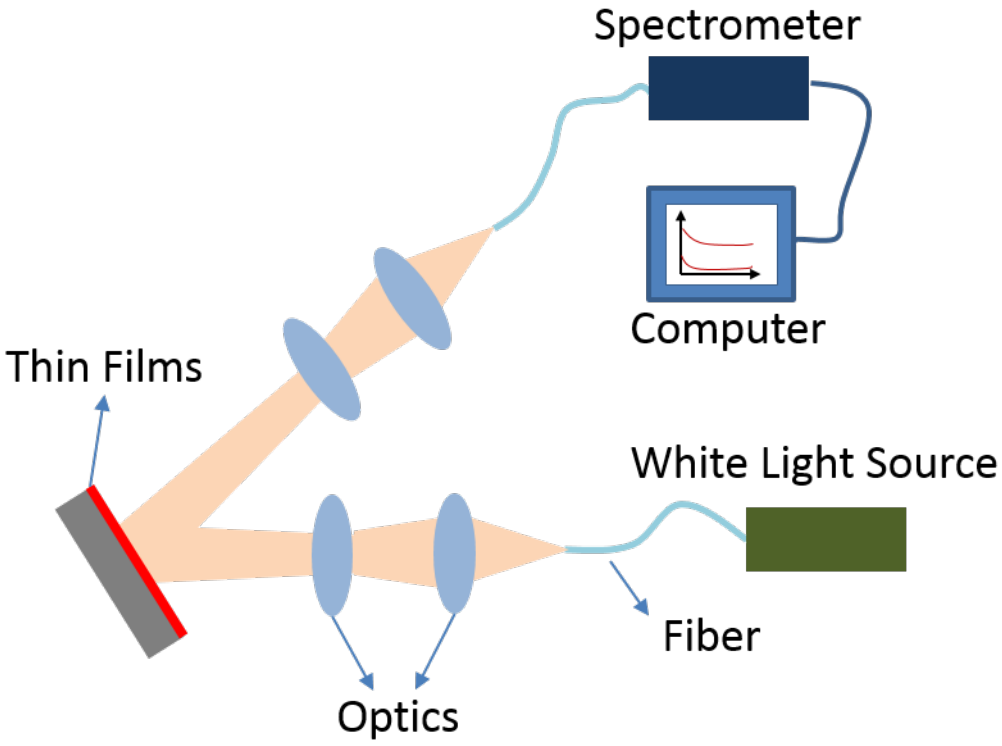

Figure 3-4. Schematic of constructed measurement apparatus for determining the reflectance of multilayer anti-reflection coatings.

3.4 RESULTS AND DISCUSSIONS

Given the steps outlined, one layer and two layer coatings that are relatively close to the design conditions were manufactured. A photograph was taken of the 3 samples (Figure 3.5), one is for bare silicon, the second is of a one layer TiO_2 coating, and the third is of a two layer TiO_2 and SiO_2 coating on silicon substrate. For taking the photographs, by using an LCD screen an image was

projected onto the samples as to allow uniform light distribution aiding in obtaining relative reflectance information.

Figure 3-5. Photograph of 3 samples illustrating the reflectance. **Left:** Bare silicon with a 2nm native oxide layer. **Middle:** A one layer TiO_2 layer. **Right:** A two-layer anti reflection coating.

The photograph of the single TiO_2 layer (middle) shows that the overall reflections are reduced and that the reflection is stronger in the ultraviolet region of the spectrum, which can be seen from the greenish look of the image. On the other hand, the right image, the image of the two layer anti-reflection coating, shows a significant reduction in reflectance as it is much darker while still appearing greenish blue in color.

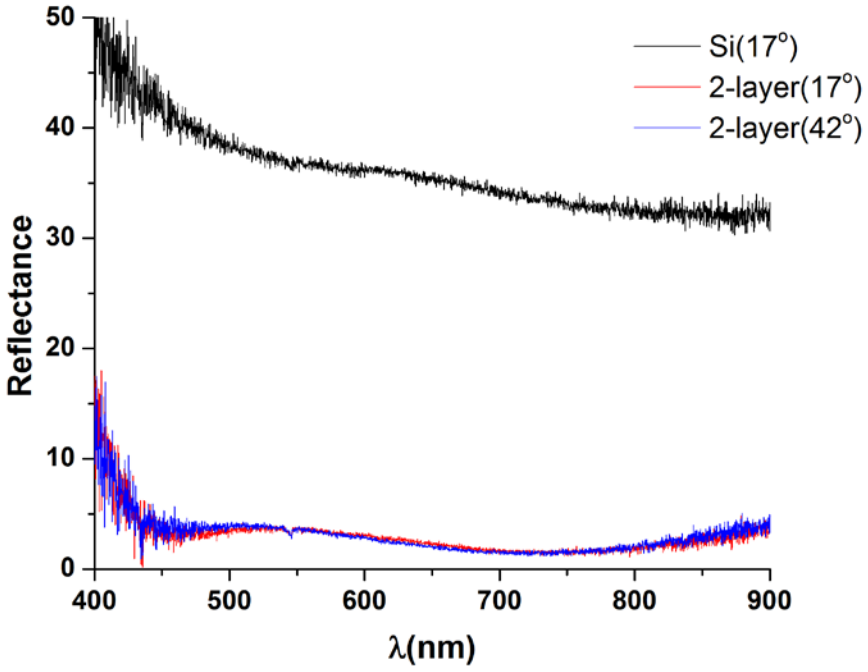

Figure 3-6. The measured reflectance of bare silicon and a two-layer anti reflection coating on silicon. For the two-layer coating, two measurements were obtained: one at 17°, and one at 42°.

A sample of bare silicon and a two-layer anti reflection coating composed of a TiO_2 layer and a SiO_2 layer are characterized. By Ellipsometry the thicknesses of the films were obtained to be 59nm for the TiO_2 layer and 107nm for the SiO_2 layer. The average value of the measured reflectance was computed at 17° to be 3%. This compares reasonably well with the 2.7% predicted by simulation. The slight deviation can be accounted for by the thickness variations and the measured refractive indices. Measuring refractive indices and film thicknesses by Ellipsometry will have a certain amount of uncertainty associated with them. This is especially true for measuring the refractive indices of thin films with sub-wavelength 3D nanostructures. The largest

uncertainty, in general, of the fitted quantities is associated with the estimated porosity and can be as large as 10%.

3.5 CONCLUSIONS

Thus far, I have demonstrated a novel method for the manufacture of high quality low cost anti reflection coatings. The method is based on being able to tune the refractive indices of functional materials in the deep sub-wavelength regime by 3D nanostructuring. The three-dimensional aspect is of practical importance for ensuring wide angle operation. It ensures that there is not a significant amount variation in the refractive index as a function of angle due to the underlying 3D symmetry in the composing nanostructures. Although, here only up to two-layer coatings were demonstrated, it is very much possible to expand the work to 3-layers and so on. The current limitation is entirely from the minimum refractive index achievable with the current method. Some other combinations of block-copolymers and solvents can quite likely provide much lower refractive indices for SiO_2, much lower than 1.2. Block-copolymer templating can be quite complex and hence, there are many parameters to explore. Therefore, solutions must exist that can further reduce the refractive index of silicon dioxide. Achieving a refractive index value of 1.08 would allow the manufacture of optimized 3-layer coatings that would provide a highly functional and low cost method to produce antireflection coatings in the 400-1100nm window with an angular acceptance of 0-75°, with a mere 4.7% reflectance on average. In comparison with other demonstrated techniques that require costly methods such as e-beam evaporation and sputtering, the demonstrated method is a highly desirable alternative. All the complications are essentially in the making of the proper chemical precursor, after which it is a simple manner of

coating and heating. The precursor can be dip coated, spin coated, and even sprayed onto surfaces and is very scalable and can be processed on curved surfaces with ease, as well. With some developments, it is highly likely that with spray coating gradients can be achieved. That is, the concentration of the block-copolymer, or of some other form of templating method, can be altered in time during the spraying process to realize continuous refractive index profiles, such as the quintic profile. Advancements of this nature could provide significant reductions in the reflectance of practical devices, such as optical lenses, LCD displays, practical glasses (car windows), and solar cells.

4.0 NANOMATERIAL INTEGRATED OPTICAL FIBER SENSORS

Materials with tailored conductive, absorptive, emissive, and surface properties have been well explored. In conductometric sensors, the surface and conducting properties are of great interest[12, 59-64]. Surface enhanced functional metal oxide sensors have seen decades of developments and have been widely commercialized. Generally termed porous metal oxides, these materials can greatly enhance the surface properties required for improved sensory responses with a chemical species of interest[2, 14, 59, 64-68].

One application of refractive index engineered of metal oxides is integration with optical fiber. This merger of two advanced technologies has the potential to expand the sensory capability of optical fibers to include numerous chemical and biological species. Optical fiber technology has been around for some time and so as its exploration for sensory applications. Optical fiber sensors can detect a number of things such as temperature, pressure, bending, gyroscopic, refractive index, and various other responses that can be acquired by applying some physical distortion to the fiber that changes the guiding conditions providing readily detectable signal variations. The inert nature of silica limits its use for the detection of chemical and biological species. As the sensory applicability of optical fibers advanced, new types of modifications such as writing fiber Brag gratings or long period gratings in the fiber lead to the expansion of their detection abilities to sound and vibration and etc.

Progress in the exploration of fiber sensing has led to the coating of different materials in contact with the fiber core, thus far with somewhat limited success. Palladium coated fiber Bragg gratings are a popular research topic for the detection of hydrogen[69]. In these types of sensors, when the palladium coating is exposed to hydrogen it expands. This expansion is transduced into

an optical signal by the grating through stretching. The basic idea behind these types of modifications it to include materials as transducers between the light in the fiber and the desired environment to be sensed. One of the important ways light in the fiber interacts with the sensing material is through evanescent coupling and when exposed it induces measurable changes in the light.

There are a few successful reports of optical fiber sensors employing some sensory material coatings but the important details such the mechanism that allows high refractive index materials to be coated on fiber[70-78], were simply not discussed. This is because as per the design of optical fiber, which nowadays is the product of decades of developments, the material components making up the fiber do so in a precise way with carefully doped core and cladding components to provide their functionality. The coating of another material without careful consideration of such parameters as thickness and refractive index can, in most cases, be quite detrimental and light will quickly escape the fiber leaving nothing behind to detect with[79]. It comes naturally to try to incorporate these highly developed and functional sensing metal oxides into the optical fiber sensing platform to greatly extend their sensory capabilities.

The decades of advances that metal oxides have seen in enhancing and finely tuning their sensory abilities in conductometric sensors adapted to a more robust sensory platform such as optical fiber could bring forth rapid advances in sensory technology and expand the reach of fiber detection schemes to encompass virtually all things that can be detected. Fiber detection schemes can be used at hundreds of kilometers from the source and can be highly distributed. This merger could advance the realization of smart building and superstructures in which virtually anything can be detected form structural properties, to vibrations, to sound levels, to air quality, to humidity, the presence of hazardous chemicals and gasses, and the list goes on. This can be all done with the

same fiber which can multiplexed and switched between the different types of sensors towards the realization of unparalleled sensory feedback.

The importance of such things is difficult to imagine but one does not have to look far. Without the precision sensors working in the background, automobiles, airplanes, and pretty much any advanced machinery would not be what it is today. It is difficult to say how many different sensors exist in the human body working in unison to allow us to function. Without them we could not walk, talk, touch, feel, taste, see, and simply be as we are. But, to realize such things, advances in sensor technology are needed.

The difficulty of merging functional metal oxide sensory materials with optical fiber lies at their fundamental refractive index incompatibility. These metal oxides have, in general, refractive indices of around 2, whereas the refractive indices of optical fiber are around 1.46. The difference between the two may not seem like much but one only has to examine the refractive index differences between the core and cladding of fiber, generally on the order of 0.5%, to realize that these differences are extremely large. So, before coating these highly desirable materials, something else has to be done. To merge this gap, in this work a method for successfully integrating the two advanced components is presented with simulations to examine the fundamental issues followed by practical realizations. This is accomplished by using the refractive index tailoring technique developed for on-fiber compatibility designs. Besides the conventional transmission and refractive index type analysis, a time of flight type characterization was performed, typically termed distributed sensing, by frequency domain reflectometry. The latter type of measurement has the potential for the realization of a single optical fiber sensors that can function as a linear combination of hundreds of sensors, and can potentially be used to measure sensory gradients across a single sensor.

4.1 BACKGROUND

Optical fiber, in general, is composed of two silica materials arranged cylindrically where a difference in the refractive indices of its two components is achieved by a slight doping difference. At the center of the fiber is the core, which has a refractive index that is slightly higher than that of the cladding (the outer material). Because the refractive index of the core is lightly higher, there is an angular condition called the critical angle that allows light to be totally internally reflected at the interface of the core and cladding to keep the light in the fiber.

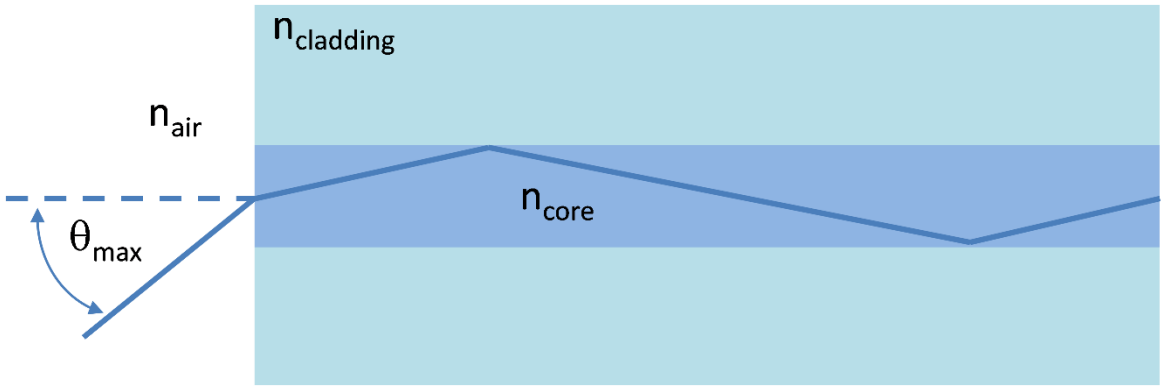

Figure 4-1. A simplified schematic of optical fiber and the critical angle. The critical angle determines the maximum acceptance angle at which light can be launched into the fiber.

This critical angle is a function of the difference in the refractive indices, given by

$$\theta_c = \sin^{-1}\frac{n_2}{n_1} \qquad \textbf{Equation 4-1}$$

The light rays that couple into the fiber are given by the basic equation, indicating an allowed angular range

$$\mathbf{NA = n \cdot \sin\theta_c = \sqrt{n_{core}^2 - n_{clad}^2}} \qquad \textbf{Equation 4-2}$$

As an example, a single mode fiber with a core index of 1.468 and cladding index of 1.46 has a critical angle of 84° from the line normal to the interface. The small index differences and the type of the material are specifically engineered to exhibit low losses for propagation over very large distances. Fibers with small index differences are generally referred to as weakly guiding due to the fact that the longitudinal components of the fields are much weaker than the transverse components, and that the guided waves are essentially parallel with the fiber axis. For light to be bound in the fiber, the propagation constant has to be smaller than the wavenumber in the core ($\beta<n_{core}k_o$) and larger than the wavenumber in the cladding ($\beta>n_{clad}k_o$). Where the propagation constant is defined as $\beta=k_o n_{effective}$. The field distributions in the fiber are then obtained by defining a characteristic wave equation in cylindrical coordinates with the appropriate boundary conditions. The solutions of these equations are a family of Bessel functions[80].

$$u(r) \propto \begin{cases} J_l(k_T r), & r < a(core) \\ K_l(\gamma r) & r > a(cladding) \end{cases}$$

$$k_T^{\,2} = n_{core}^{\,2} k_o^{\,2} - \beta^2 \qquad \textbf{Equation 4-3}$$

$$\gamma^2 = \beta^2 - n_{clad}^{\,2} k_o^{\,2}$$

The different possible modes in the fiber propagate at different angles, with each mode having an associated propagation constant.

$$\beta_{lm} \approx n_{core} k_o \left[1 - \frac{(l+2m)^2 (n_{core}^{\,2} - n_{clad}^{\,2})}{M} \right] \qquad \textbf{Equation 4-4}$$

To illustrate the variation in the intensity distributions of the various modes, the figure below shows these distributions for various values of l and m, where l=0 and m=1 is the fundamental mode. In the telecommunication window, the typical core diameter of single mode

fiber is 8μm and multimode fiber is 50μm or greater. Single mode fibers are designed to allow the propagation of only the fundamental mode. These propagating modes, as shown, are discrete and exist only for integer values of l and m. In between the propagation modes there is a continuum of radiation modes that leak the light out of the fiber. Therefore it is ideal to couple light into the guided modes as, otherwise, the optical losses will be large.

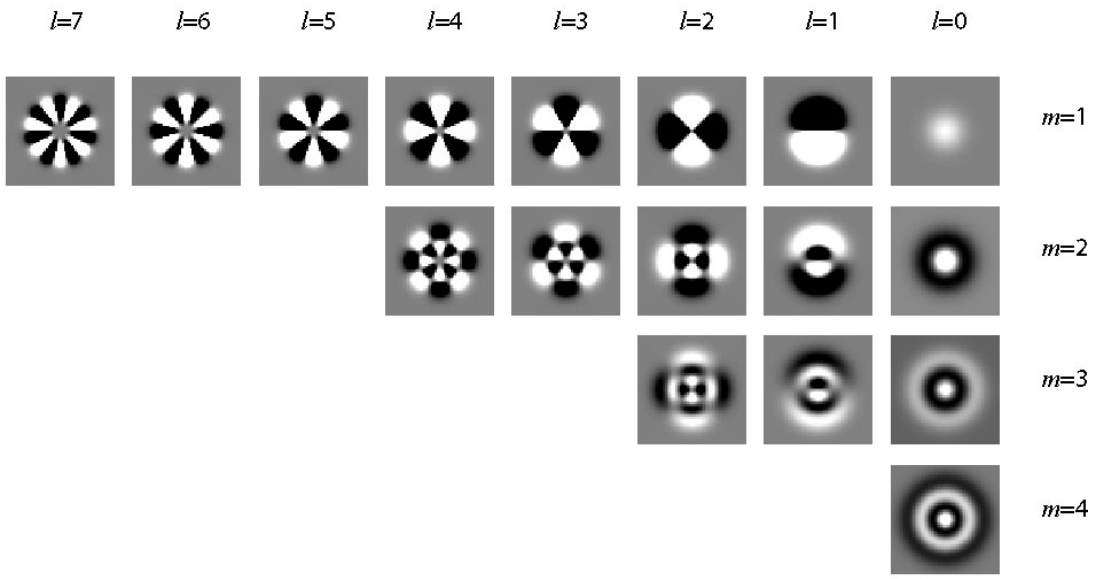

Figure 4-2. An illustration of the various modes that can exist in optical fibers[81]

When light is totally internally reflected at the core cladding interface, light does not abruptly turn around, instead it penetrates into the cladding material in the form of an evanescent wave. This type of a wave is non-propagating and decays exponentially away from the interface. The penetration depth of the evanescent waves is given by the following expression,

$$\delta = \frac{\lambda}{2\pi\sqrt{n_{core}{}^2 \sin^2\theta - n_{clad}{}^2}} \qquad \textbf{Equation 4-5}$$

where θ is the angle of the mode measured from the normal to the interface. Higher order modes have a θ that is smaller, therefore, these penetrate deeper into the cladding of the fiber.

4.1.1 Absorptive Sensing

To take advantage of the confined light inside the core for sensing, various configurations are possible to interact light with an external sensing material. A sensory material can be placed on the end of the fiber to interact directly (Figure 4-3 A). This type of direct interaction would, in general, yield the strongest response, however, the light recovery in this scheme requires a number of additional optical components and imposes some design difficulties.

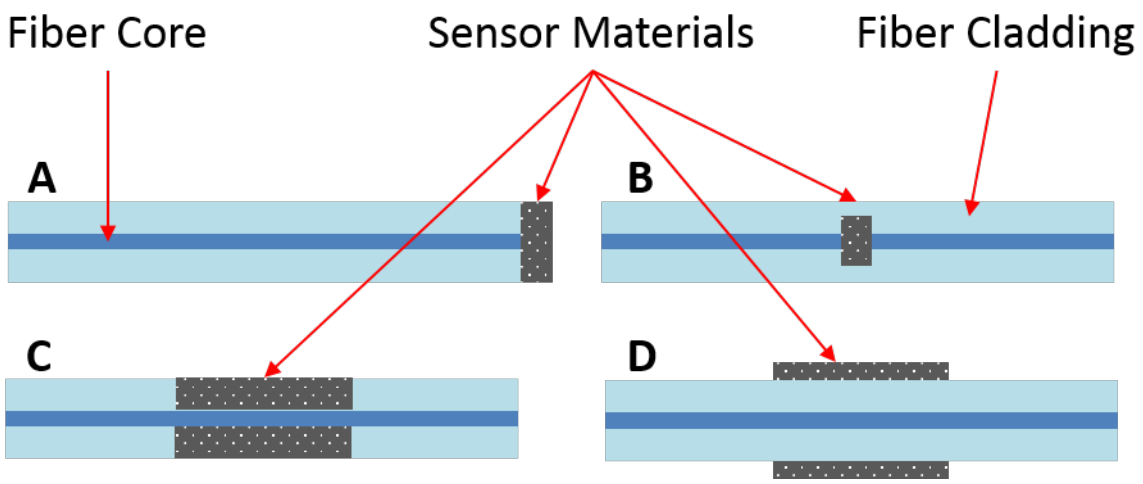

Figure 4-3. An illustration of the possible implementation schemes of sensing materials with optical fiber. **A:** Fiber with material coated on a polished end. **B:** Fiber with a section partly removed and replaced with a sensing material. **C:** Part of the cladding is removed and replaced by a sensing material. **D:** material Sensing material is coated on top of a cladding material.

To eliminate some of these issues, with some processing a part of the fiber can be removed and the sensing material can be placed inside the fiber, replacing some section of the fiber core (Figure 4-3 B). In such a configuration, no external optical components are needed. Depending on the type of the design, this can be as long as ~1 millimeter before the light intensity collected at the other side of the material by the core has diverged and scattered too much. In another configuration, the evanescent light can interact with a sensing material where it is coated on the cladding of the fiber (Figure 4-3 D) or part of the cladding material is removed and is replaced with the sensing material (Figure 4-3 C). To achieve good sensitivities with the configuration depicted in Figure 4-3 D, long period fiber gratings are generally employed which scatter light out of the core into cladding modes that can interact more strongly with the sensory material through the evanescent waves. The configuration shown in (Figure 4-3 C) is ideal and has many benefits in comparison, such as it is in line with the fiber and it does not require additional components for its operation.

The weaker interactions through evanescence can be compensated for as arbitrarily long portion of the fiber can be coated if the material's refractive index is adjusted and optimized. Second, this configuration can also be placed in active cavities in which the interaction lengths can be amplified by dozens of times. So, in general, the evanescent configuration schemes are less cumbersome in design as all the sensory information is available in the fiber and is compatible with the typical instruments used in fiber interrogation. In the characterization of the refractive index engineered metal oxide sensors demonstrated here, the evanescent type interaction is exploited by coating the sensory material in contact with the core.

In is important to note that when coating sensory materials in contact with the fiber core there are design requirements that need to be carefully considered. Such as the refractive index of

the sensory material in comparison with the refractive index of the core and cladding values. These intricacies will be discussed in more detail later.

4.1.2 Refractive Index Based Sensing

In conjunction with absorptive type sensing, a refractive index based response may be present. In such cases fiber Brag gratings can be used to determine the magnitude of such responses. A fiber Bragg grating is a periodic disturbance in the refractive index of the fiber core such to create a constructive interference for some portion of the spectrum, resulting in a sharp peak in the reflected light centered on the resonance wavelength. The location of the peak of the fiber Brag grating (FBG) depends on constants such as the period of the disturbance (Λ) and the effective refractive index of propagating mode $\Delta n_{eff} = \frac{\Delta\lambda}{2\Lambda}$. The effective refractive index depends on a number of things one of which is the refractive index of the surrounding material and the environment. Therefore, fiber gratings written in optical fiber can be used to characterize changes in the refractive indices as these changes result in shifts in the peak position of the reflected resonance peak of the grating.

4.2 INTEGRATING SENSORY MATERIALS WITH OPTICAL FIBER

To date, successful demonstrations of fiber optic sensors utilizing metal oxides are realized by thin film coatings as in this domain the index compatibility issues can be mitigated[72-78]. Typically, the thickness of the high-index sensing film should be less than ¼ of the wavelength in the metal oxide sensing film ($\lambda/4$) to preserve guiding in the fiber's core[79]. This places restrictions on the

usable film thicknesses (typically less than 120 nm). This is due to the fact that the refractive indices of important sensory metal oxides (TiO_2, SnO_2, ZnO, etc.) is typically >2. Whereas, the typical optical fiber is made of silica and doped silica with refractive indices <1.47. Functional sensory metal oxides, having refractive indices significantly greater than the refractive indices of fiber materials, are effectively incompatible for use with optical fiber. Except under certain circumstances of very thin films or when the refractive indices of these sensory materials are engineered such that they are lower than the refractive index of the fiber core.

As detailed in the previous section, light guiding in the fiber is due to total internal reflection which requires the condition that the refractive index of the fiber core is lower than that of the cladding material. If this condition is not maintained, then light will leak out of the fiber as there will be no guiding modes to couple to. In such conditions only leaky modes exist in which light is progressively lost from the fiber. An important parameter in describing light propagation in optical fiber is the propagation constant, which is a function of the effective refractive index of the fiber, $\beta = n_{eff}\frac{2\pi}{\lambda}$. The effective index is a function of the wavelength and the propagating mode and is an important parameter to consider especially when connecting two different fiber together.

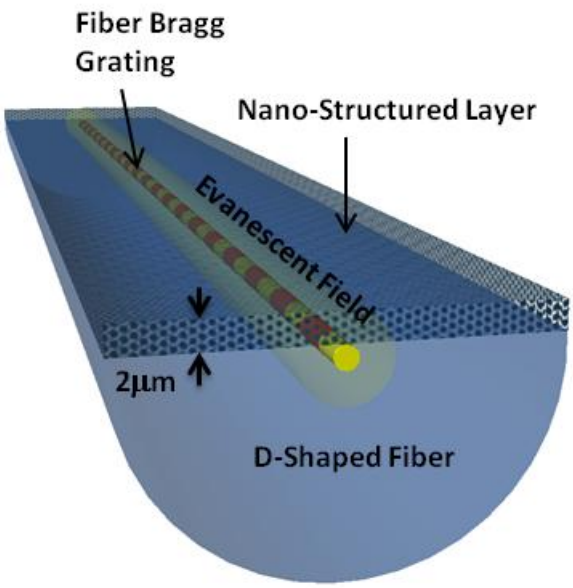

Figure 4-4. Schematic of D-shaped fiber coated with a sensory nanomaterial, with an in-fiber Brag grating.

A schematic of D-shaped fiber coated with a nanomaterial in contact with the fiber core is illustrated in Figure 4-4. D-shaped fiber is a good platform for sensing applications since half of the cladding material is retained for mechanical support, allowing for ease of handling. When a part of the fiber cladding is removed and replaced with another material, in essence, it is the same principle as connecting two different fibers together.

As mentioned before, some have explored thin films coatings on fiber for sensory applications. Given this, there is a fundamental question that needs to be asked. How is it that thin films with material refractive indices ~2 can be coated on fibers with refractive indices ~1.46, without completely destroying the guiding of the fiber? The principle of operation of high index thin film coatings has not been well characterized to date and, thus, I am going to examine it here. Fundamentally, it has to relate to the concept of effective mediums. That is, given a certain film thickness and wavelength of operation, it most likely works under the effective medium theory.

Generally, thin film coatings have thicknesses of ~100nm with operating wavelengths of ~1550nm. The penetration depth is going to be much larger than the film thickness under such circumstances. Therefore, it is reasonable to assume that the fundamental mechanism behind why thin film coatings work is due because light propagating in the fiber, which is coated with a thin sensory material, will see an effective index that is much lower than the film's refractive index. That is, a 1D effective medium is generated by making the thickness of the film small, much smaller than the wavelength, and smaller than the penetration depth of light into the cladding material. Now, to describe this quantitatively would be quite cumbersome, especially for the complicated geometry that is presented here. Therefore, instead, numerical simulations are performed to examine such conditions.

Mode analysis simulations were performed with COMSOL, with full wave finite element analysis, to examine how the different film thicknesses and their associated refractive indices influence the distribution of the fundamental mode of the constructed fiber sensor. In Figure 4-5**.** Left the power density distribution of the fundamental mode is shown for a film thickness of 2μm and film refractive index of 1.5, at a wavelength of 1550nm. At this film thickness, the penetration depth of light is comparable to the film thickness and, therefore, the resultant effective index is higher than what it would be needed to maintain total internal reflection. Therefore, the fundamental mode that can exist in this structure is going to be primarily in the sensory coating. In Figure 4-5. Right a configuration is shown in which the refractive index of the coated film is reduced to be slightly lower than the refractive index of the core, and it is approximately equal to the refractive index of the cladding material. In this case, the fundamental mode is not disturbed too much away from its nominal distribution.

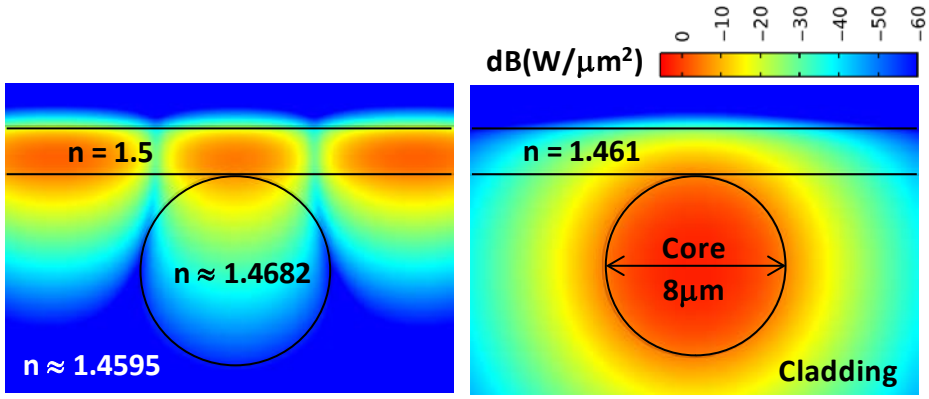

Figure 4-5. Left: Light intensity distribution in D-shaped fiber when coated with a sensing material of non-optimized index, a configuration in which light leaves the core of the fiber. **Right:** Light intensity distribution in D-shaped fiber when coated with a sensing material of optimized index, a configuration in which light guiding is preserved in the fiber.

To create a complete picture, simulations were performed for a large range of film thicknesses and film refractive indices. Combinations that resulted in providing effective indices that were very close to the effective refractive index of the fiber before modification, were kept. Figure 4-6 show these values. That is, the refractive index and its associated film thickness that result in an effective refractive index that is equal to the nominal effective index. The nominal effective index is the designed effective index of the fiber. This effectively confirms that indeed one can coat high index thin films on fiber, by replacing part of the cladding material, and can still not only maintain the guiding condition, but effectively mode match the coated and uncoated sections of the fiber. This is an interesting results whose functionality has not been well established. Although, as stated before, it is most likely due to averaging effects that arise when the film thicknesses are considerably smaller than the penetration depth of the light.

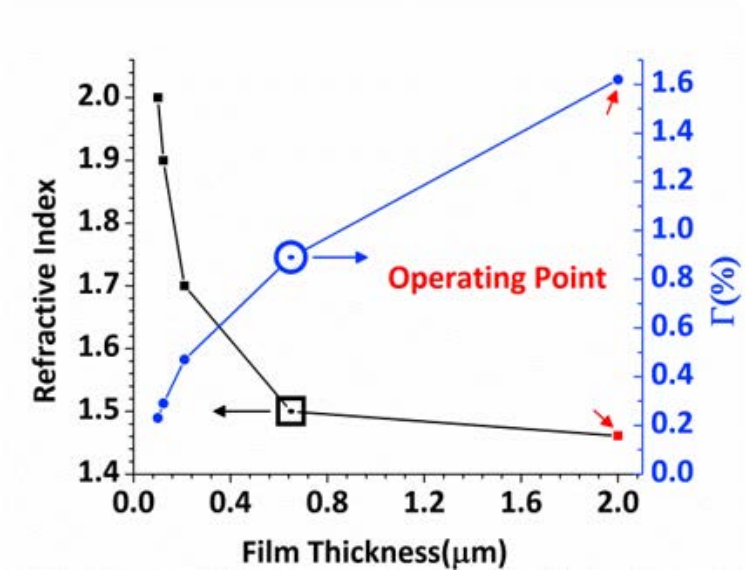

Figure 4-6. The dependence of the refractive index on the thickness of the sensory films in order to maintain the effective refractive index of the sensor at the nominal value. The simulation were examined for an operating wavelength of λ=1.55μm.

This figure states that if you are going to coat a material with a high refractive index, its thickness needs to be very small. On the other hand, if the refractive index is smaller than the core's refractive index, the film can be arbitrarily thick as any relationship between those two properties has been removed. To measure the importance of film thickness for sensory purposes, a parameter called the confinement factor is used. It is, in essence, the ratio of the power that exists in some region of interest (S_1 to S_2) to the total power present. It is obtained by integrating the power density in the sensory film or the region of interest and the whole region, and diving one by the other[80].

$$\Gamma = \frac{\int_{S_1}^{S_2} u^2(r)dr}{\int_{-\infty}^{\infty} u^2(r)dr} \qquad \textbf{Equation 4-6}$$

To return to the previous discussion, sensory coatings can be integrated with optical fiber in two ways. One way is to use very thin films and the other is to use thick films whose refractive indices have been engineered to be lower than the refractive index of the fiber core. Form the optical perspective, thick films should interact more strongly as they trap more of the evanescent light in their region, as illustrated by the right hand side of Figure 4-6. The improvements gained simply from the perspective of optical interactions is approaching an order of magnitude when thick low index nanomaterials are used instead of high index thin films

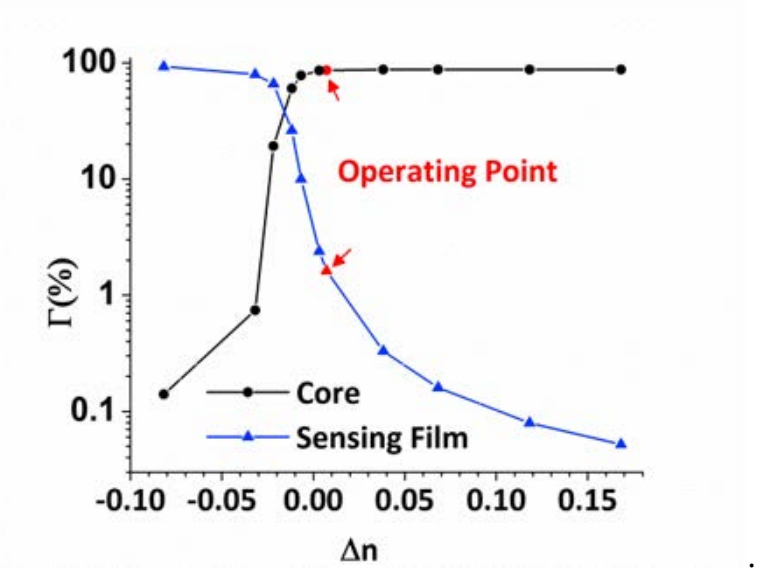

Figure 4-7. Examination of the dependence of the confinement factor on small variations in the difference between the refractive index of the core and the refractive index of the film ($\Delta n = n_{core}-n_{film}$).

In Figure 4-7 the effect of small changes in the refractive index of the sensory film on the overall confinement factors is shown. The x axis is $\Delta n = n_{core} - n_{film}$, where the core index is a constant. The red data points indicate the nominal operating point of the fiber, before modification.

It is, to first order, the condition that is to be achieved by engineering the refractive index of the sensory film while holding its thickness constant at 2μm. This condition results in the sensory material having a refractive index of 1.461. This will also ensure that the effective index after modifying the fiber will not deviate significantly from the nominal value, minimizing the optical losses by ensuring mode matching between the sensory and unmodified portion of the fiber.

4.3 SENSORY MECHANISM

4.3.1 Chemiresistive Sensors

Metal oxides are an important class of functional materials for application in chemical and biological sensing and seen decades of developments. The typically sensory use is conduction based, that is, the conductivity (resistivity) of the metal oxide changes when exposed to the desired chemical species of interest. Therefore, these types of sensor are generally termed chemiresistors.

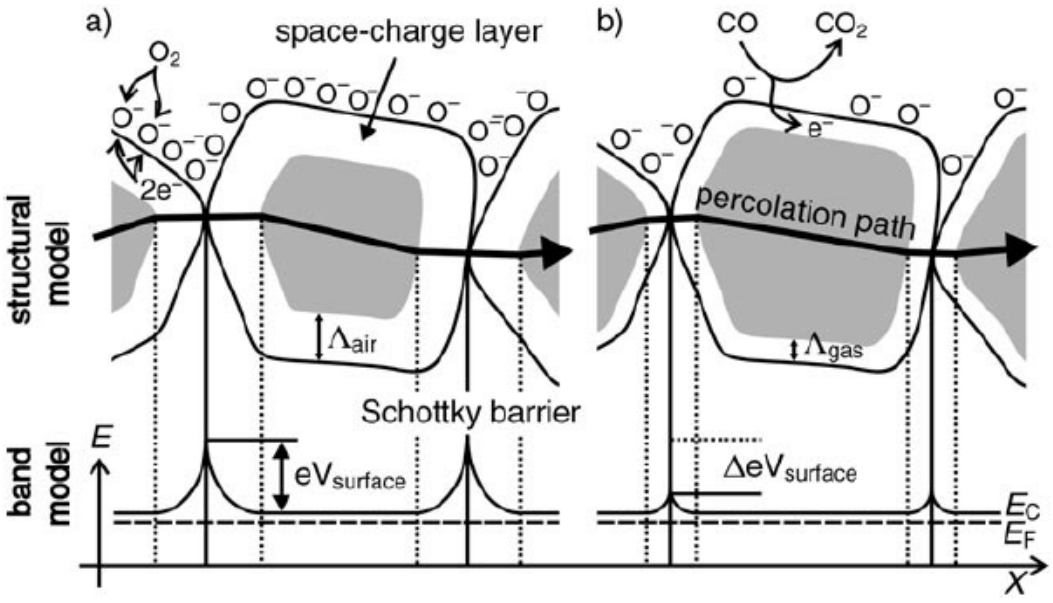

Figure 4-8. Overlaid band model with the nanostructure illustrating the sensory mechanism of a polycrystalline metal oxide **a)** initial state and **b)** after exposure to CO[66].

In chemiresistors the typical response mechanism involves the removal of surface adsorbed oxygen by a reactive gas. These types of sensory materials are composed of grains in contact with one another and each grain is surrounded by a space charge layer. The space charge layer, typically between 1-10nm, is the interaction penetration into the material. In an air ambient environment oxygen and various other chemical species that may be present are adsorbed onto the surface, creating this so called space charge layer, as illustrated in Figure 4-8. In this example oxygen is adsorbed onto the surface of a metal oxide material creating the space charge layer. Depending on the type of the material, whether it is n-type or p-type, some of the conduction electrons are bound resulting in either an increase or decrease in conductivity[67]. When the target gas species, in this case CO, is present it combines with the surface adsorbed oxygen releasing back into the

conduction band the previously bound electrons. For an n-type material, this results in an increase in electrical conductivity. Whereas, for a p-type material this results in a decrease in electrical conductivity because the conduction electron will recombine with the majority carrier which, in this case, are the holes. For example, carbon monoxide will interact with a surface adsorbed oxygen to form carbon dioxide, releasing an otherwise bound electron back into the conduction band[66]. It is important to note that the type of the reaction is of importance, as well. The typical sensory mechanism is due to oxidation reduction and re-oxidation.

This type of analysis also shows the importance of nano-structuring and porosity. The conduction paths taken are in the form of percolations paths. That is, the electrons will find the path of least resistance through the interconnecting material grains (Figure 4-9). Smaller grains should have faster sensory responses from the perspective of the penetration depth of the space charge layer. It takes a longer time to interact more deeply into the material. Therefore, controlling the grain size such that the entire grain gets modulated can provide useful enhancements. One, the slow deep processes are eliminated resulting in a fast responding sensor, and the second is that the entire material is used as the sensor. Not just the 1-10nm surface volume. Therefore, highly porous materials that allow fast mobility of the analyte through the structure are ideal and will ensure fast and strong sensory responses[66, 67]. In essence, nanostructuring on the 10nm scale will greatly increase the surface area which directly increases the sensory response, while at the same time speeding up the process. Such structuring will also eliminate the Schottky potential barriers that come about from semiconductor metal semiconductor junctions, resulting in an optimal flat band model.

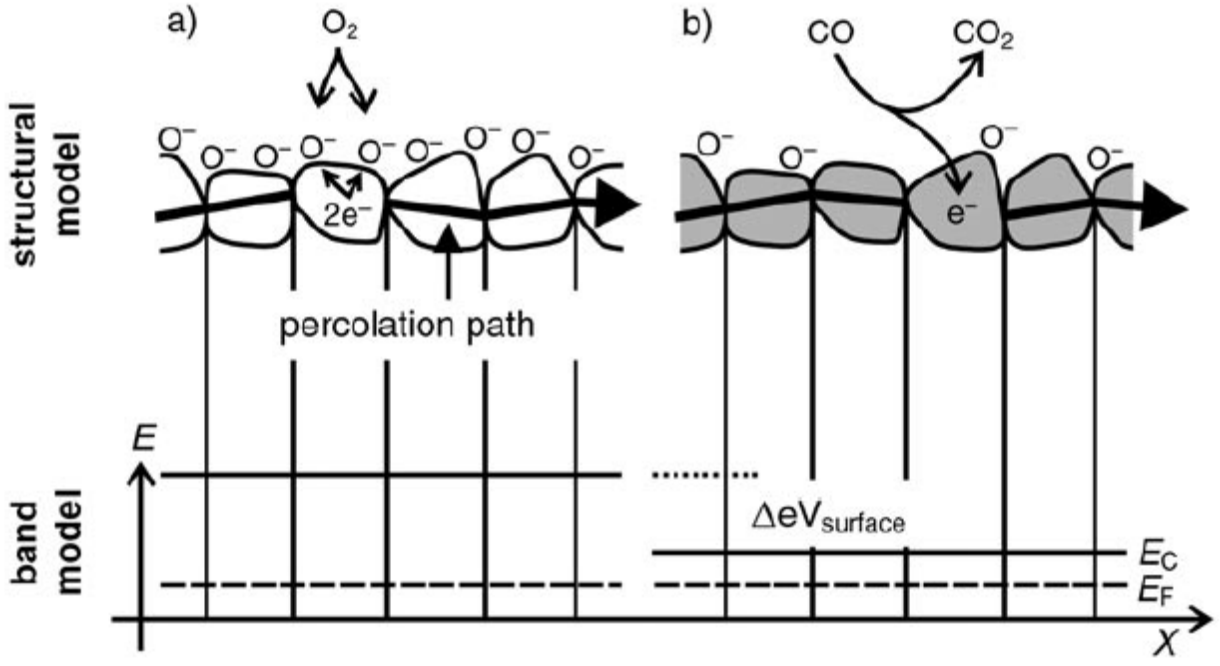

Figure 4-9. Overlaid band model with the nanostructure illustrating the sensory mechanism of a polycrystalline metal oxide **a)** initial state and **b)** after exposure to CO. In this case the grain size is smaller than the modulation depth, fully utilizing the sensing structure[66].

The electrical response of Chemiresistive type sensor can be enhanced further by incorporating noble metal sensitizers. The rate of response, the magnitude of the response, and the selectivity to chemical species can all be altered by this action[63, 82]. Two types of sensory responses have been described by sensitization with noble metals such as Pt, Pd, and Ag. Depending on the sensitizer and the environment, a chemical sensitization, electrical sensitization, or a combination of the two may be present. In chemical sensitization, the promoter activates a test gas and enhances its catalytic oxidation (spillover effect), without affecting the conductive behavior of the semiconductor directly. It merely increases the rate of the interaction. In the electronic type sensitization, the promoter modifies the conductive behavior of the semiconductor

by a direct electrical interaction through a charge transfer process. Such as changing the oxidation state of the noble metal promoter which will modulate the width of the space charge layer of the semiconductor[63].

4.3.2 Metal Oxide Integrated Fiber Sensor

The as described sensory response of chemiresistive sensors is the prominent theory, although, the governing fundamental mechanism is still under debate. Despite this, their operation is well characterized by experiments over the past few decades. On the other hand, integrating these metal oxides with optical fiber for sensory applications is relatively novel and the expected sensory responses are not well established. Therefore, what can be expected from what we already know of chemiresistors? We know that there will be a modulation of the concentration and mobility of the electrons in the conduction band. How will this interact with light? We know from Drude's theory that light at near infrared wavelength should interact with the free electrons[83, 84]. This will happen by what is known as intraband absorption which is the excitation of an already excited electron to a higher state. So, in other words, the modulation of the concentration of free carriers should result in the modulation of the observed absorption of near infrared light. But, this may not be the whole story.

Chemiresistive sensors typically have issues with cross sensitivity by responding to many different chemicals, and requiring additional work to isolate the response to a specific analyte[85]. Solutions such as the electronic nose and alike have been developed that essentially tackle the issue the way the human nose seems to, which is by pattern recognition. Therefore, if there might be a refractive index response in addition to an absorptive response of metal oxides when exposed to a chemical species, this may provide another detection mechanism. This additional sensory

mechanism may be another way to address cross sensitivity. Optical fiber gratings are very sensitive to modulations in the refractive indices of the surroundings. Therefore, by including fiber Brag gratings in the constructed sensors, a possible refractive index response can be examined.

The low refractive index nanomaterials will be structured on the 10nm scale, approximately. Hence, the entire structure, or close to it, will be modulated in the presence of a chemical species. Therefore, the entire material will behave as its surface, in better words, the surface effects dominate. Given the relative complexity of this, it is difficult to predict whether there should be a refractive index response, and, if there is, at what magnitude. From the Kramers-Kronig relation we know that a change in the imaginary part of the refractive index will have an associated change in the real part of the refractive index. How does this translate to our system in which the surface effect dominate? In order to address these fiber Brag gratings are written into the nanomaterial integrated fiber sensors which will allow for the measurement of refractive index changes that come about from the surface adsorption and desorption of a chemical species. On an important note, the refractive indices of gasses are different from the refractive index of air by very small amounts. Therefore, the effect on the refractive index of nanomaterials by replacing air in the holes by another gas should be very small and it is not the change that is of concern here

Furthermore, palladium thin film coated optical fibers with Fiber Brag Gratings have been well explored for hydrogen sensing[86-88]. The fundamental mechanism is based on the reaction between palladium and hydrogen forming palladium hydride, resulting in a conductive modulation and a lattice expansion[89]. This lattice expansion results in a change in the refractive index, when examined on the macroscopic scale[88]. Therefore, palladium doped TiO_2 nanomaterial integrated

optical fiber poses a unique mix of the underlying physics. This combination is explored to determine the type of the sensory mechanism.

4.4 EXPERIMENT

4.4.1 Fiber Grating Fabrication

To produce the fiber Bragg grating, D-shaped fiber was first soaked in high pressure hydrogen at 1600 psi for 2 weeks. A type II Fiber Bragg Grating (FBG) was inscribed by a phase mask (2.5x1cm with 1060nm period) with a 248nm KrF laser source (GSI Lumonics PM-844) with a cumulative fluence of ~6,000 pulses at ~50mJcm^{-2}.[90, 91] The FBG sensor was then annealed at 120^{o}C for 24 hours to diffuse out all the residual hydrogen. The fiber Bragg Gratings were manufactured in the lab by colleagues.

4.4.2 Sensor Fabrication

Precursor solutions providing refractive indices in the vicinity of 1.461 at a wavelength of 1550nm were selected and used for the manufacture of the integrated fiber sensors. The SnO_2 nanomaterial precursor used had the molar ratio of 1:0.04:7.71:39.58, of $SnCl_4$ to Pluronic F-127 to 37% HCl to Ethanol. The TiO_2 precursor solution used had a molar ratio of 1:0.013:1.43:5.64:31.58, of titanium isopropoxide to Pluronic F-127 to 37% HCl to H_2O to 1-butanol. The palladium doped TiO_2 coating had a molar ratio of 1:0.031:0.013:1.76:5.64:32.9, of titanium isopropoxide to Pluronic F-127 to $PdCl_2$ to HCl to H_2O to 1-butanol. The addition of 3mol% of palladium had no

discernable effect on the refractive index of TiO_2. It is expected that PdO nanoparticles are distributed throughout the TiO_2 matrix, in a very small quantity.

Prior to coating the precursor, the D-fiber with the FBG was etched with a buffered HF solution for 21 minutes to remove the 3μm cladding material (5:1 40% NH_4F to 49%HF ACS Reagent Grade, Sigma Aldrich), exposing the core on the flat side of the fiber (extreme care should be taken as HF is very dangerous). The fibers were coated by pulling them through the precursor in a petri dish at an approximate rate of 5mm/s.

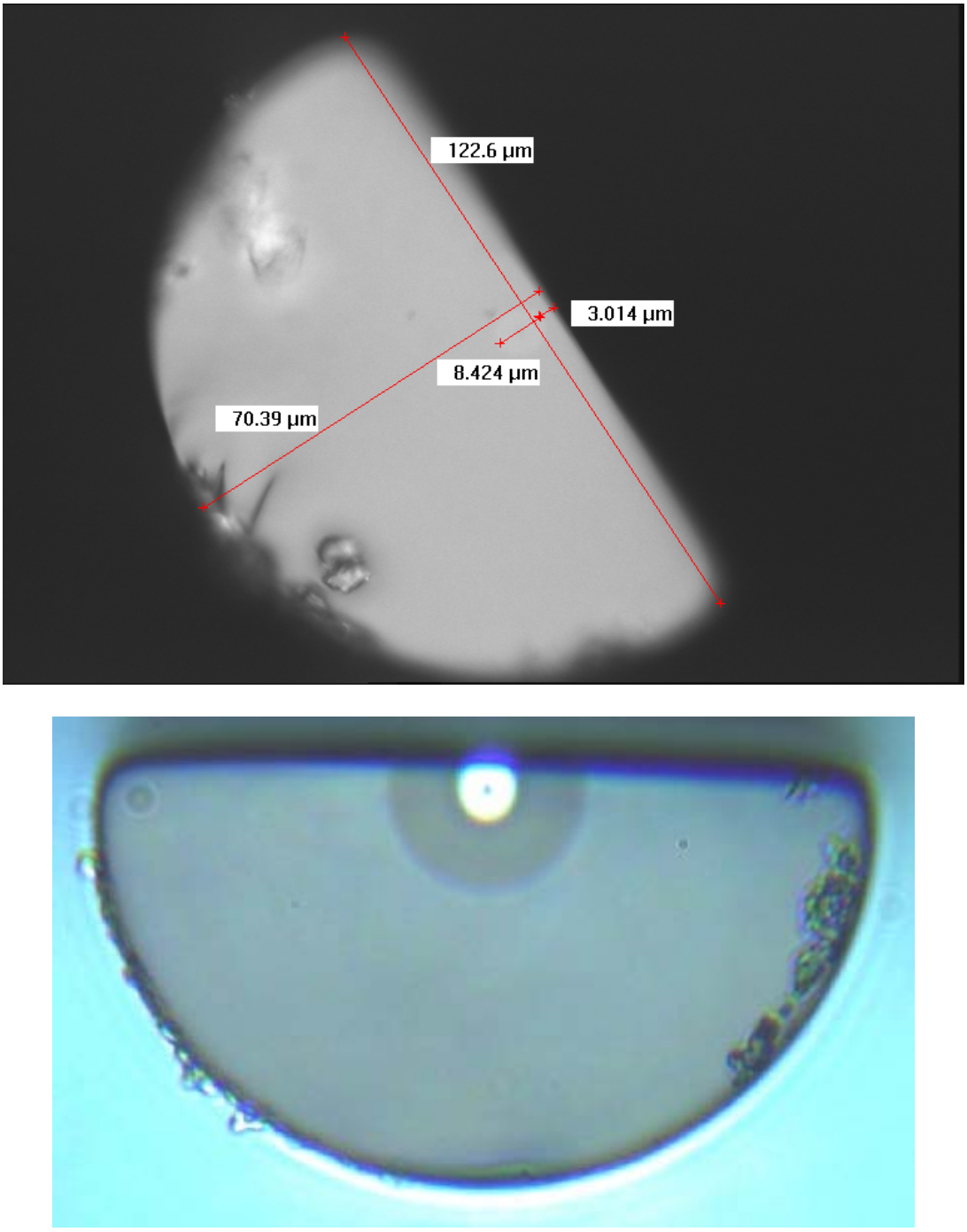

Figure 4-10. Top: SEM image of D-shaped fiber showing the approximate dimensions. Having a core diameter of approximately 8µm with a residual cladding of approximately 3µm in thickness on the flat side of the fiber. **Bottom:** Microscope image of the D-shaped fiber after etching, indicating that the core is indeed exposed on the flat side of the fiber. The bright center is the core of the fiber.

The coating length of the SnO_2 nanomaterial on fiber was 7cm, whereas the coatings for TiO_2 and Pd-doped TiO_2 were 15cm in length. The fiber Brag gratings were position to be in the center of the coated section of the fiber. The coated samples were then left to dry in air overnight. This was followed by a temperature treatment (annealing) in which the sample was placed in a controlled environment furnace and heated. To start with, the temperature was increased at 5°C/minute to 130°C and held for 1 hour. Followed by ramping (3°C/minute) to 600°C, where it was held for 2 hours. Afterwards, the sample was cooled to room temperature at a rate of 3°C/minute.

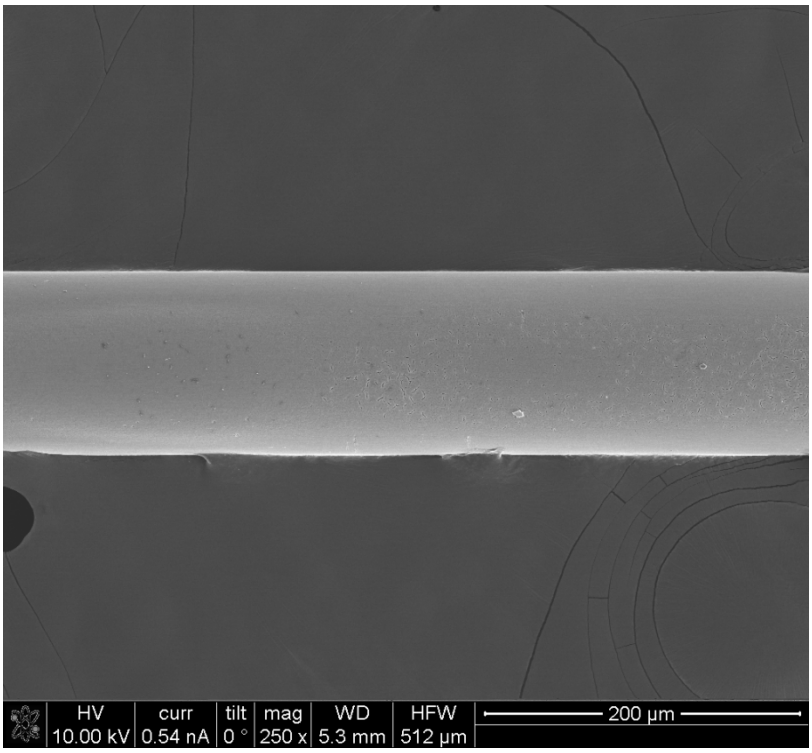

Figure 4-11. SEM image showing a SnO_2 nanomaterial coated section of the fiber, showing that good film quality can be obtained over a wide region.

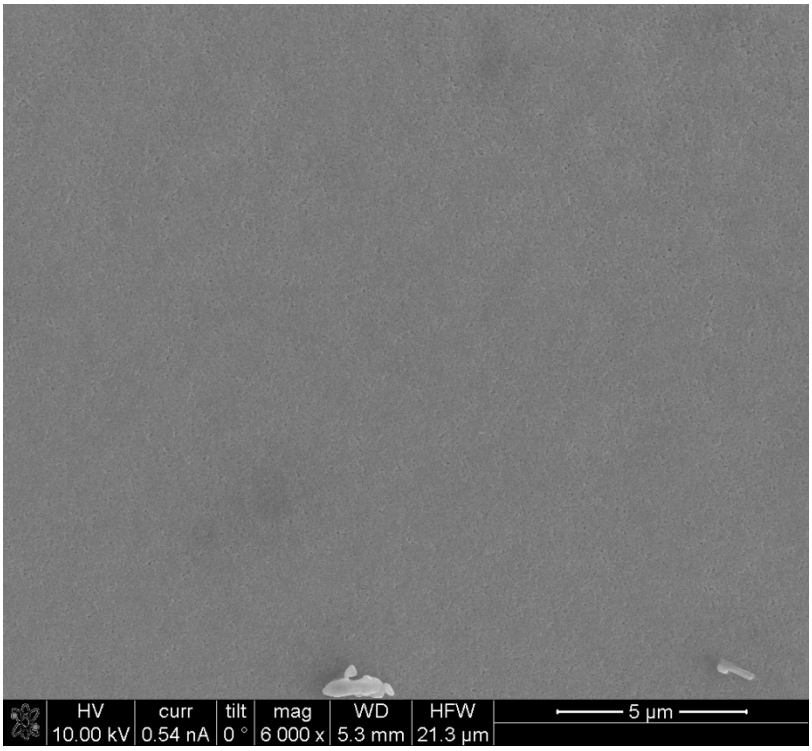

Figure 4-12. Magnified SEM image of the SnO_2 nanomaterial coated on D-shaped fiber.

After performing the sensory analysis, the fiber was broken into several parts and several different types of imaging were performed. One of which was the cross sectional examination of the sensor. Figure 4-13 shows the cross sectional view of the fabricated fiber sensor and a magnified image showing the film thickness and geometry with respect to the optical fiber core.

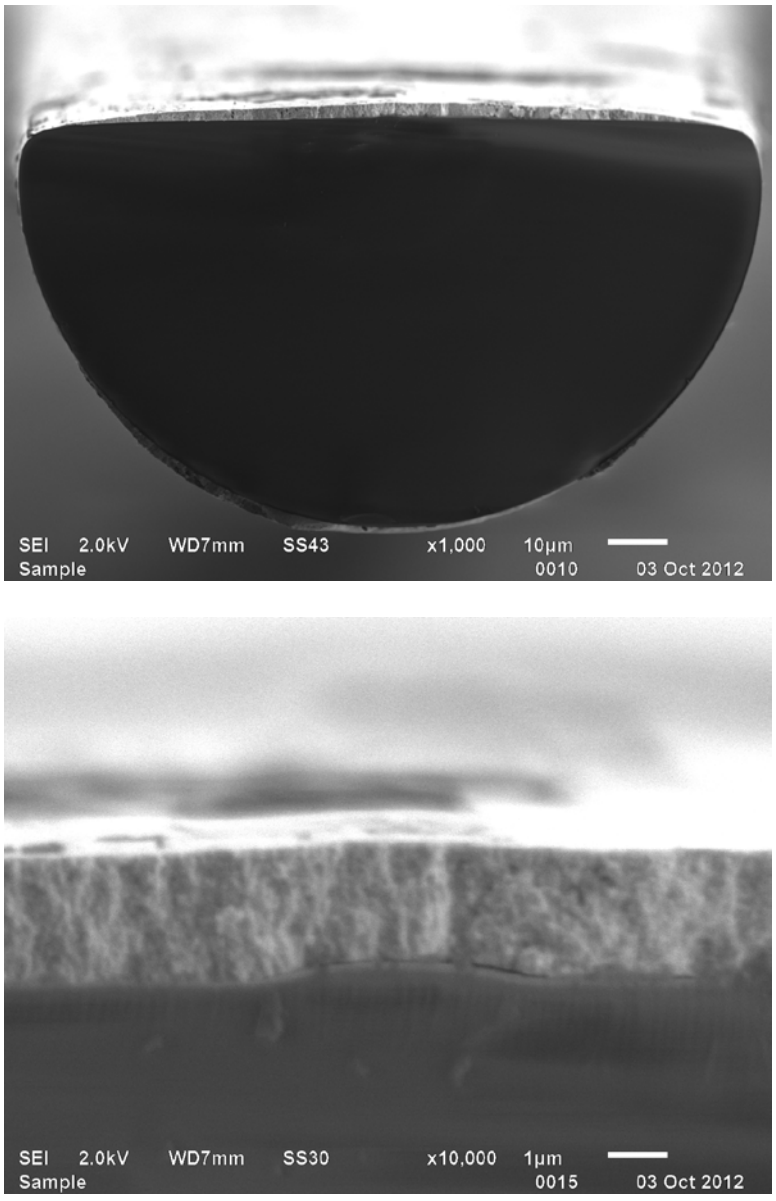

Figure 4-13. Top: Cross sectional SEM image showing the coated SnO_2 nanomaterial film on D-shaped optical fiber. **Bottom:** Magnified view of the region above the fiber core, indicating a film thickness of ~2µm. The curved central protruding region is the fiber core on which the nanomaterial film was coated on top of.

A constructed Pd-doped TiO_2 optical fiber sensor was cut into small sections using a fiber cleaver, and imaged using a scanning electron microscope. Figure 4-14 illustrates the dimensions of the features with a film thickness above the core of the fiber of approximately 2μm.

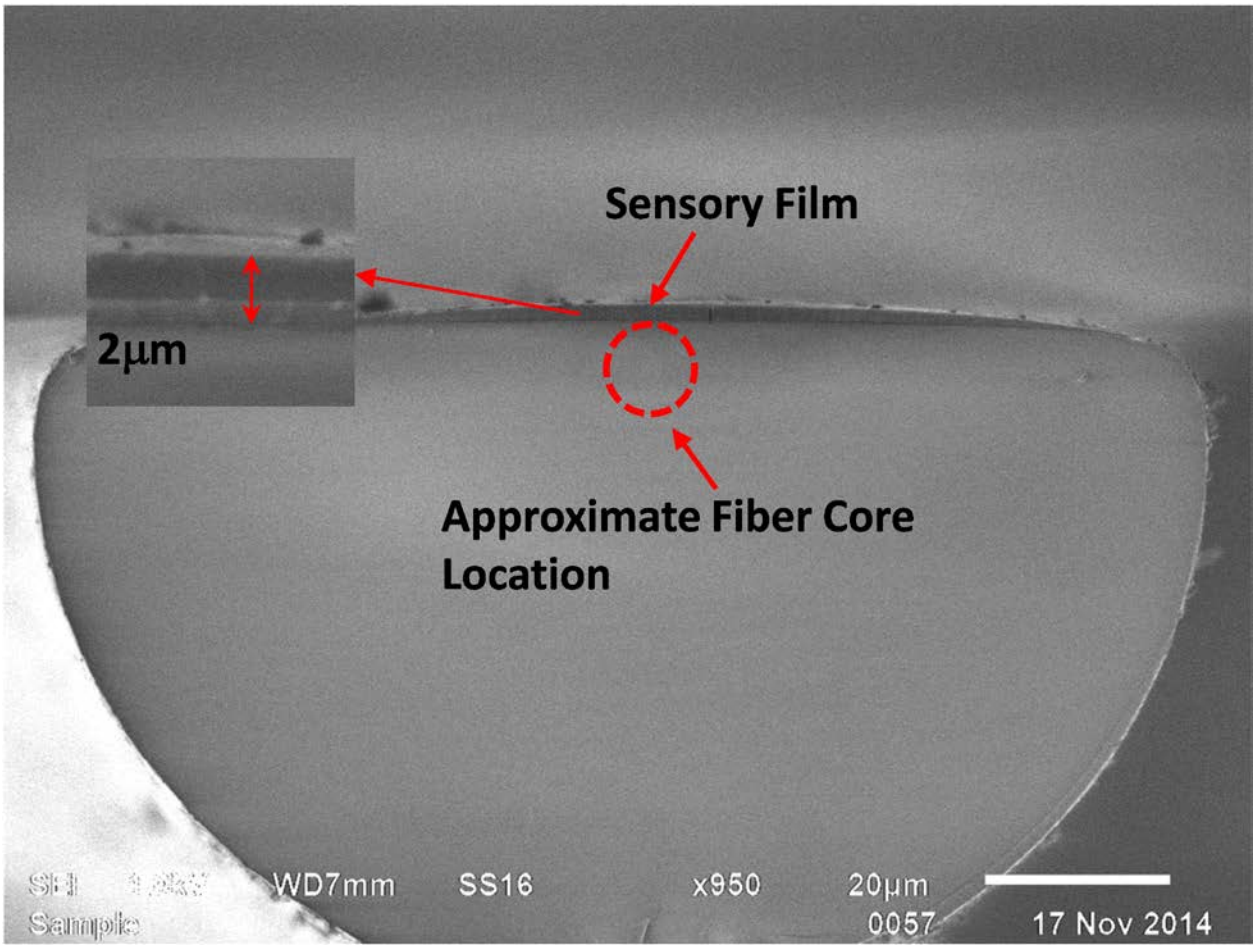

Figure 4-14. Cross sectional SEM image showing the coated Pd-doped TiO_2 nanomaterial film on D-shaped optical fiber.

4.4.3 Experimental Setup

An experimental setup was constructed to aid in the characterization of the nanomaterial integrated optical fiber sensors. The main component in the setup is the controlled environment furnace as shown in Figure 4-15 as it allowed for the controlled exposure of the fabricated samples to various gasses and mixtures of gasses at temperatures up to 800°C. The length of the heating element is 35cm with a 1cm in diameter passage through the center. A 6mm in diameter quartz tube was placed inside the heating element whose ends were terminated with fittings that allowed for the input and output of the gasses. The optical fiber sensors were placed in the quartz tube and rubber ferrules with the appropriate fittings were used to tightly seal the fiber inside the chamber.

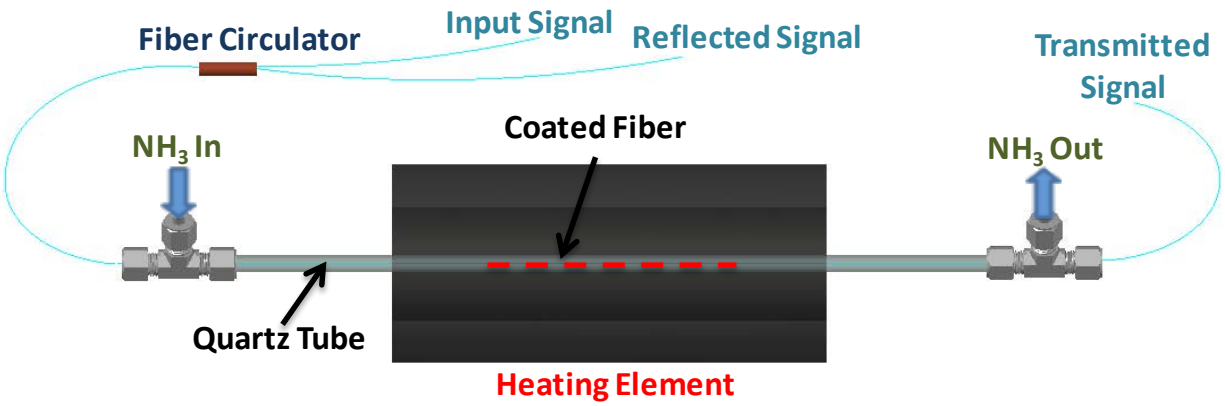

Figure 4-15. Experimental schematic used in the testing of the fabricated sensor

The outlet of the system was fed into a fume hood, allowing for the safe removal of otherwise hazardous gasses. The gas inlet was controlled by precision digital flow controllers, allowing for gas flows in the range of 1SCCM up to 500SCCM.

The placement of an optical fiber circulator at the input end of the fiber allows for the separation of the forward and backwards propagating components of the light. The backward propagating components are due to reflections by the fiber Brag grating, which are then analyzed with and optical spectrum analyzer (OSA, Agilent 86140B). The transmitted component of the light is collected with an OSA or an InGaAs photo detector and recorded with the help of LabVIEW. The light source used was an amplified spontaneous emission source (MPB EBS-7210) with appreciable optical power in the 1520-1610nm range. A fusion splicer (Ericson FSU 995 FA) and a manual fiber cleaver (Fujikura CT-30) were used to cleave and connect the fiber ends.

In the case of distributed sensing measurements one end of the fiber sensor was directly connected to a Frequency Domain Reflectometer (Luna OBR 4600). This instrument served as the light source and analyzer with a computer interface. This measurement technique allows for the characterization in the variations of the Rayleigh backscattered signal amplitudes. Distributed sensing is a relatively novel type of optical fiber sensing which, by using a time of flight type of analysis coupled with an analysis of the backscattered Rayleigh signal, can provide information on the various changes that may occur across the length of an optical fiber.

4.5 RESULTS AND DISCUSSIONS

4.5.1 Nanostructured SnO_2 Optical Fiber Ammonia Sensor

The FBG reflection peak was monitored during the coating and heat treatment processes. The peak disappears immediately upon the coating of the precursor due to its high refractive index in

comparison with the core of the fiber. When the temperature reaches 200°C and shortly after, the grating peak begins to return due to the removal of the structure directing component (Pluronic F-127). Indicating that the refractive index is forming to be lower than the refractive index of the core of the fiber. The fiber sensor coated with the SnO_2 nanomaterial was exposed to a constant flow (200 SCCM) of 10% NH_3 and 90% N_2 mixture at atmospheric pressure for 3 minutes, followed by a 3 minute recovery period in dry air (200 SCCM).

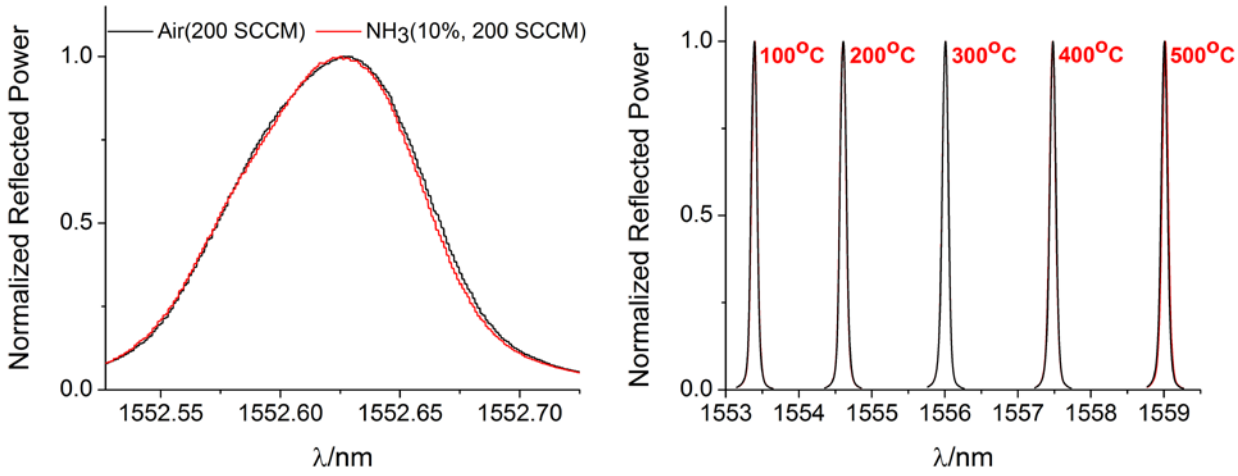

Figure 4-16. Left: FBG resonant peak response of the sensor at room temperature to 10% NH_3. No shift in the resonance peak is observed, indicating that there is a not a significant refractive index response. **Right**: Resonant peak response of the sensor up to 500°C, showing no detected peak shift.

Monitoring the reflected signal by an optical spectrum analyzer (OSA) showed that the resonance peak of the fiber Brag grating did not change when exposed to 10% NH_3. Possible shifts in the resonance peak were examine from room temperature up to 500°C, as shown in Figure 4-16. Given the limits of the optical spectrum analyzer combined with the narrow grating peak, it is reasonable

to estimate a detection limit of 10pm. Based on the simulated results it is expected that 1.62% of the incoming light interacts with the sensory material. With this it can be estimated that the change in the refractive index has to be smaller than ~$5x10^{-4}$ in order to be below the instruments detection capability.

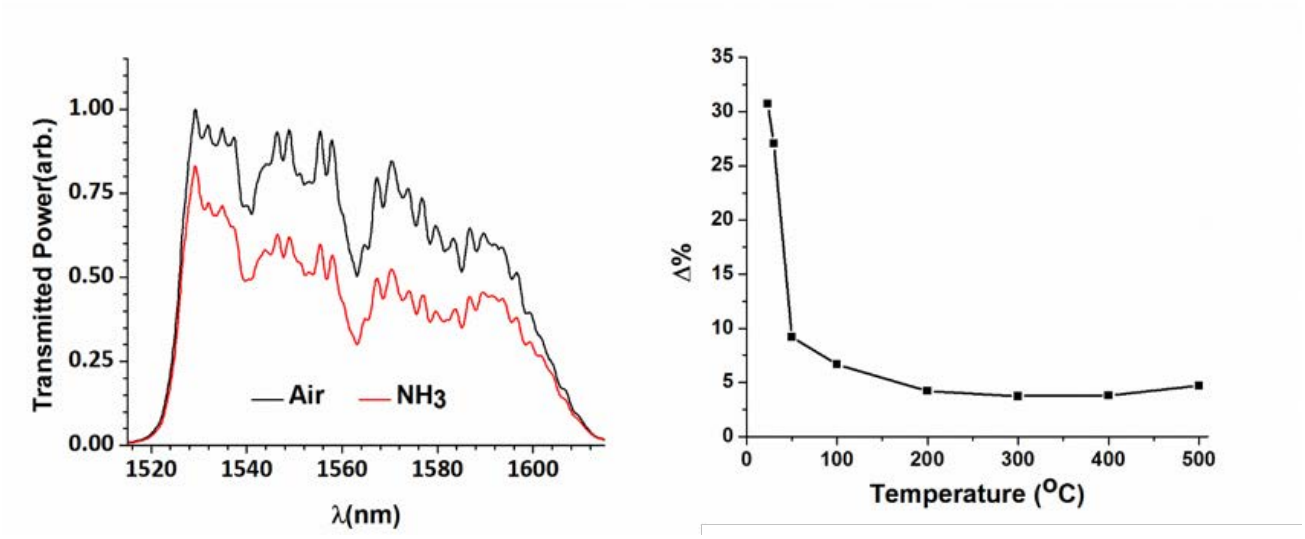

Figure 4-17. Left: Transmission analysis of the response of the sensor at room temperature to 10% NH_3, indicating a strong loss in the transmitted power. **Right:** Percent loss in the transmitted power from room temperature up to 500°C.

In examining the transmitted signal under the same exposure conditions a notable change in the transmitted power is observed (Figure 4-17) in the wavelength range of 1520-1610nm. The spectrums were integrated numerically to determine that a 30% reduction in optical power is observed in the spectral range at room temperature. Again, we know that 1.6% of the light interacts with the sensory coating through evanescence and that the coating length is 7cm in length. This provides an overall absorption coefficient of 3.1cm^{-1} at room temperature. The magnitude of the

response was examined up to 500°C as shown in Figure 4-16. A sharp decrease in the measured response is observed when approaching temperatures in the range of 100°C. This is contrary to what one would expect as in general chemiresistive sensors are heated to ~300°C to achieve peak sensitivity. Although, previous publications have reported thermal responses of SnO_2 nanostructures that differ from what would normally be expected, such as in nanoclusters and nanowires[65, 67, 92].

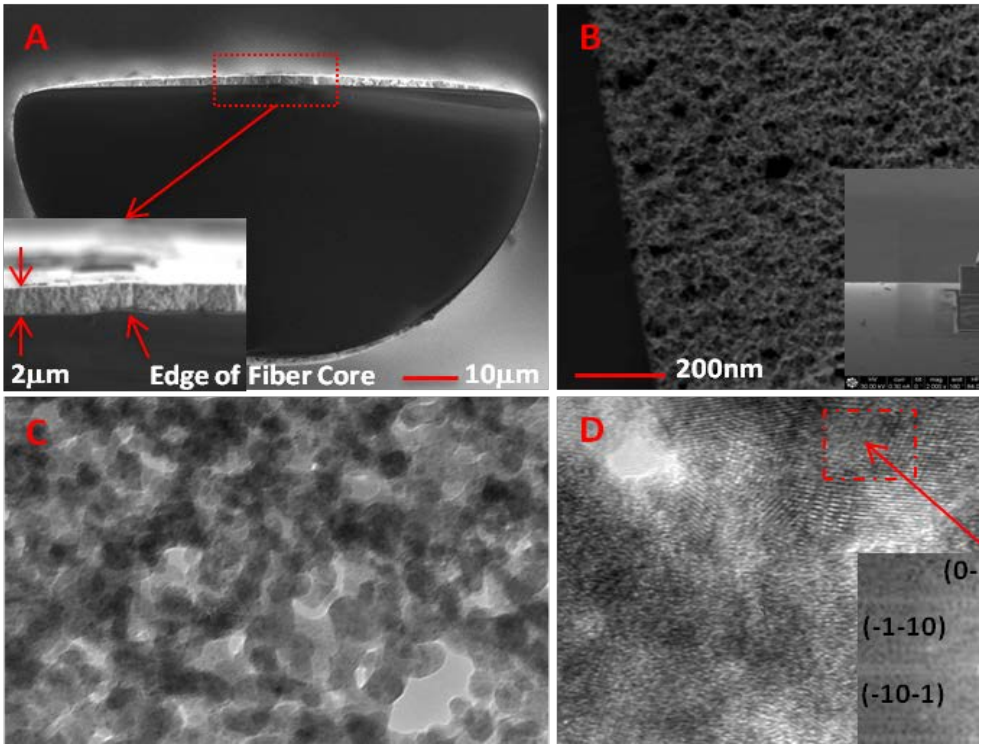

Figure 4-18. A: Cross sectional SEM image of the constructed sensor. B: STEM image of the entire film thickness along with an SEM image (inset) illustrating the FIB lift-out. C: Bright field TEM image illustrating an average SnO2 grain size of approximately 10nm. D: High resolution TEM imaging of the crystal structure of SnO2 with FFT inset indexed to the [1-1-1] zone axis of the casserite crystal structure.

After characterizing the sensory response of the prepared SnO_2 nanomaterial integrated fiber sensor, the fiber was cut into pieces and an imaging analysis was conducted to examine the underlying structure and features. Cross sectional SEM imaging shows that the thickness of the coated nanomaterial in contact with the fiber core is approximately 2μm in thickness (Figure 4-18). The inset highlights the portion directly above the fiber core, where the core is the slight curved protrusion on which the nanomaterial film rests. A scanning transmission electron image was obtained for the entire film thickness with an inset that shows the lift out process of a portion of the nanomaterial coating from the surface of the fiber (Figure 4-17. B). A protective layer of Pt was deposited on the surface prior to sectioning with a focused ion beam. Scanning transmission electron (STEM) images of Figure 4-17. C: show a large degree of film porosity through z-contrast, having features of ~20-50nm in diameter. Bright field TEM imaging shows an average SnO_2 grain size of approximately 10nm (Figure 4-17. D:). The Fast Fourier Transform (FFT) inset obtained from the high resolution TEM image indicates an underlying casserite crystal structure.

4.5.2 Nanostructured Pd-doped TiO_2 Hydrogen Sensor

After the annealing process has completed the fabricated sensor was heated to 600°C where it was exposed to 0.5% hydrogen in nitrogen. Given that this is the first exposure, after some minutes there is a sharp drop in transmission. The reason behind this is believed to be both chemical and electrical in nature. That is, adsorbed oxygen is removed from the surface of the TiO_2 and the PdO particles by chemical action. Followed by the disassociation of the hydrogen molecule and its subsequent dissolution into the Pd particles, forming palladium hydride[93, 94]. Both of these mechanisms will result in increasing the conductive property of the TiO_2 nanomaterial.

At a concentration of 0.5% Hydrogen in Nitrogen and at 600°C, the sample is held for 1hr. This is followed by heating to 700°C and applying a square wave modulation to the gas concentration with a 30 minute interval, where the on state is 0.5% hydrogen in nitrogen and the off state is pure nitrogen. The flow rate is maintained at a constant value of 40SCCM. Generally it takes about 3hrs for stabilization to occur such that the successive amplitudes in the signal remain relatively constant. Once relatively stable, the temperature was varied and held for enough time to obtain a few successive cycles. The dynamics of the sensor are shown in Figure 4-19 indicating a reduction in the response magnitude and an increase in the response time when the temperature is reduced.

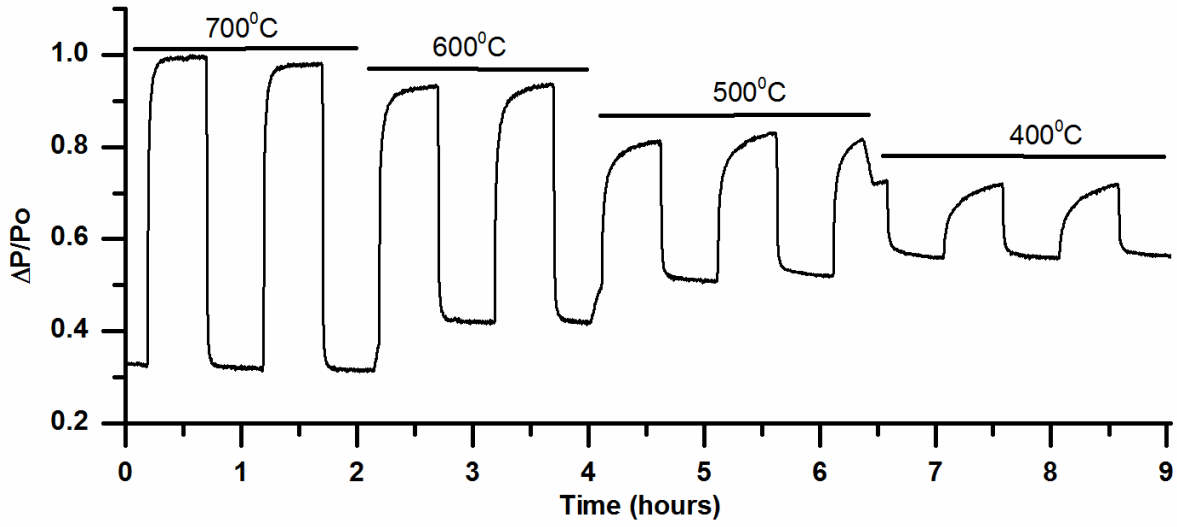

Figure 4-19. Response dynamics of the 3mol% Pd-doped TiO_2 nanomaterial coated optical fiber sensor exposed to 0.5% hydrogen in nitrogen and recovered with nitrogen.

This plot shows the normalized relative change in the measured optical power, measured with an InGaAs photo-detector over the spectral range of 1520-1610nm. The observed behavior may be explained as follows. Without the presence of oxygen, with nitrogen cycling an electrical type response is expected. In nitrogen the expected state of the noble metal promoter(Pd) is in the form of particles distributed throughout the TiO_2 matrix. Upon exposure to hydrogen, hydrogen is disassociated and dissolved into palladium to form palladium hydride. Palladium hydride has a lower work function, facilitating the charge transfer from TiO_2, increasing the overall conductivity by increasing the free carrier concentration and or the free carrier mobility[66, 93, 94]. This, in turn, modulates the transmitted optical power by free carrier absorption.

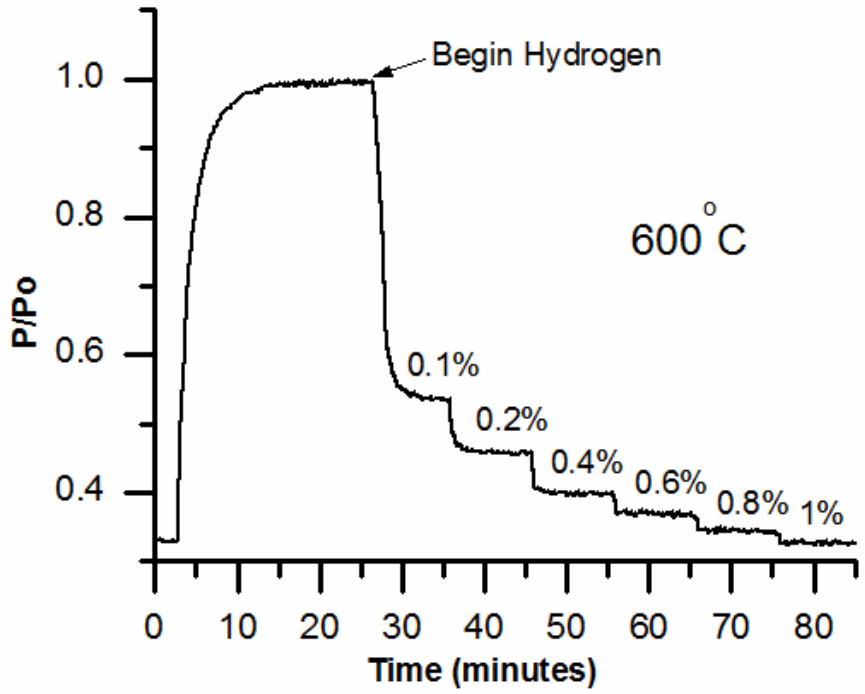

Figure 4-20. Sensor response as a function of hydrogen concentration at 600C

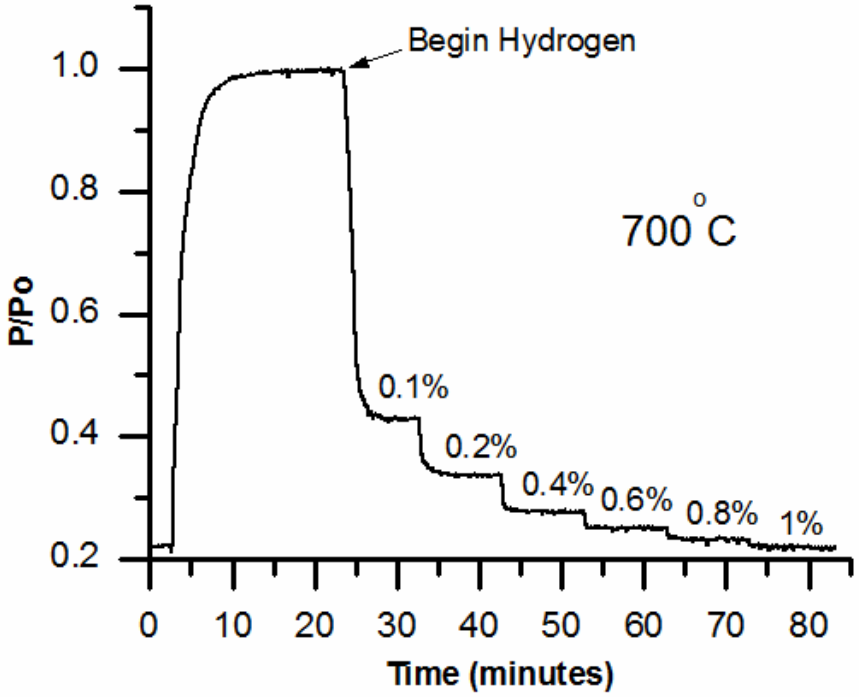

Figure 4-21. Sensor response as a function of hydrogen concentration at 700C

Two sets of data were gathered, one at 700°C and one at 600°C, showing the response of the constructed sensor as a function of the hydrogen concentration (Figures 4-20 and 4-21). The explored concentration range was from 0% to 1% as it can be seen that the change in the magnitude of the response reduces to the point of barely observable at 1%. There is a large jump in the strength of the response between 0% and 0.1%. With the experimental setup used and the concentration of gasses present, 0.1% hydrogen in nitrogen was the minimum value that could be achieved.

The magnitude of the response was characterized down to 200°C with 100°C increments (Figures 4-22). It is interesting to note that the magnitude of the response changes significantly in an almost linear fashion. At 200°C when exposed to 0.5% hydrogen in nitrogen, a ~8% in the transmitted power is observed. Whereas at 700°C, at the same concentration there is a measured change in the transmitted optical power of ~70%. Given the previous description, this could simply state the solubility of hydrogen in palladium as a function of temperature.

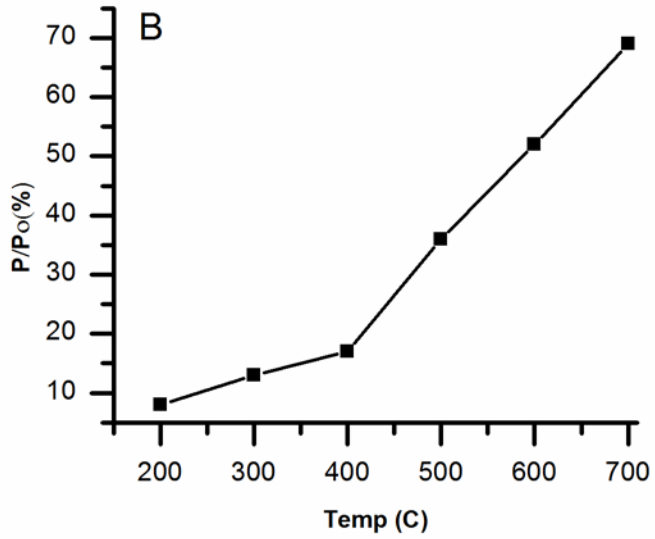

Figure 4-22. Response magnitude of the constructed sensor to 0.5% hydrogen in nitrogen, as a function of temperature.

In examining the reflected resonance peak of the fiber Brag grating, at 600°C exposed to 2.5% hydrogen in nitrogen, no observable displacement in the location of the peak is noted. 2.5% Hydrogen exposure induces a large change of approximately 6dBm in the magnitude of the reflected peak, but no discernable shift in the center wavelength. The dissolution of hydrogen in

the palladium lattice to form palladium hydride is known to result in a volume expansion[94]. Therefore, it is reasonable to conclude that if there is expansion in the Pd particles, it is significantly small, given that a very small amount of Pd is used, 3 mole % and the current detection limit. It may be also possible that Pd has been entirely dissolved into the TiO_2 lattice and exists as atomic defects. Although, this is just mere speculation given the lack of expected response and the fact that fiber Brag gratings are particularly sensitive to refractive index changes. An electronic type interaction would result in the modulation of the conductive property of the TiO_2 nanomaterial and in the expansion of the Pd nanoparticles. The expansion of the nanoparticles should change the refractive index of the matrix due to modulating the volume fraction. A conductive change will result in the modulation of the absorptive property which, from the Kramers-Kronig relation should also influence the real part of the refractive index.

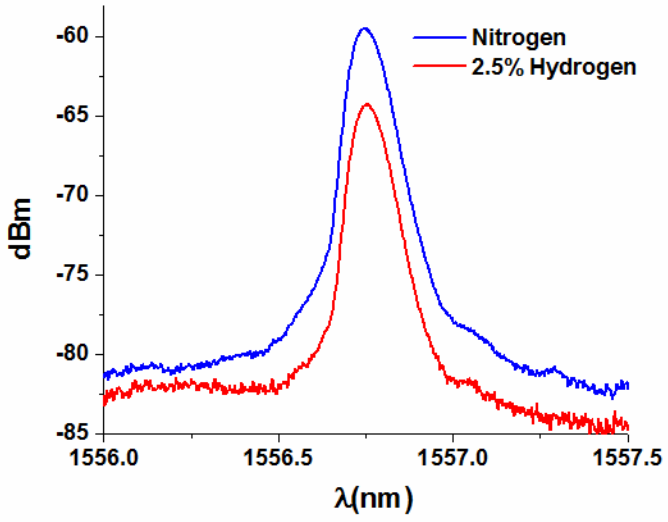

Figure 4-23. The resonance peak of the fiber Brag grating before and after exposure to 2.5% hydrogen in nitrogen at 600°C.

The transmitted power in the nanomaterial coated fiber sensor also depends on temperature. Figure 4-24 shows the variation in the recorded voltage of the photo detector when heating from room temperature to 600°C in air at a rate of 10°C/minute. The reason behind the increase in the transmitted optical power is not fully understood at this time. At lower temperatures, humidity and other components in air will interact with the nanomaterial by increasing its conductivity. But, these effects should be eliminated by 200°C. The reason behind the increase in the observed transmitted power could be from chemical sensitization. At higher temperatures oxygen adsorption at surface defects leads to the formation of O^-, by trapping electrons in the conduction band of TiO_2. Pd catalyzes the disassociations capability of TiO_2 by capturing molecular oxygen to form weak oxygen bonds. This process is temperature dependent and at lower temperatures these weak bond break to recover molecular oxygen[95]. Therefore, the obtained plot could simply be an observation of the rate of this mechanism as a function of temperature.

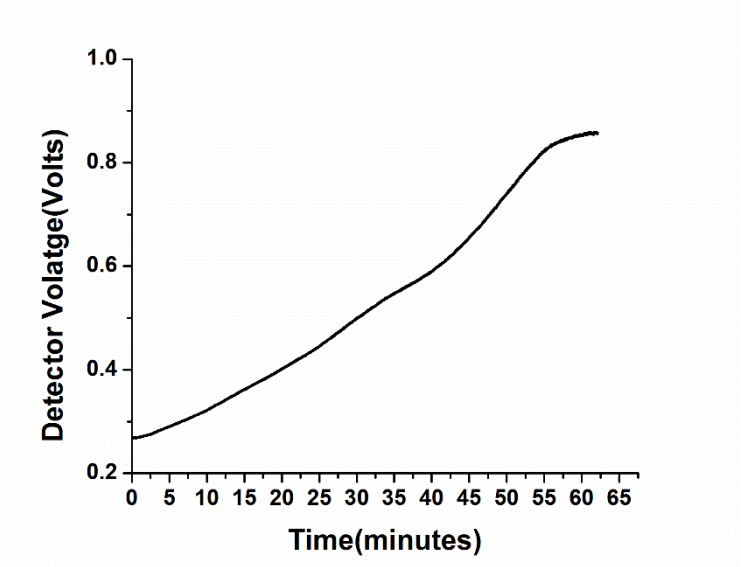

Figure 4-24. Variation in the measured detector voltage (transmitted light intensity) during heat up from 25°C to 600°C at a rate of 10°C/minute, in air.

It is know that variations in the thermal conductivity can also be used for sensing. Variations in thermal conductivity can influence the temperature conductance from the wall of the heating element to the surface of the sensor. Therefore, to examine the possibility that the observed sensory responses are from the modulation of the thermal conductivity when changing from hydrogen to nitrogen, the sensor was exposed to helium as well. Hydrogen and helium have an increased and comparable thermal conductivity in comparison with nitrogen. No sensory variations were observed when exposed to helium under the same conditions as for hydrogen.

4.5.3 Distributed Hydrogen Sensing

With the same sensor a distributed type measurement was performed to examine whether noticeable changes occur upon exposing the Pd-doped TiO_2 nanomaterial coated optical fiber to

Hydrogen. Specifically, changes across the length of the sensor element are of interest for potential applications in measuring the variation of the concentration of hydrogen in a fuel cell, for example. The backscattered Rayleigh amplitude, should in principle, be quite sensitive to changes in the fiber and the nanomaterial in direct contact with the fiber core. Changes in the absorptive properties of the nanomaterial coating will influence the light intensity and intensity distribution in the fiber, as noted earlier with direct transmission measurements. Such changes should then show up in the backscattered amplitude due to a diminishing forward propagating light intensity, which will have a direct influence on the backscattered intensity. As the measurement results show (Figure 4-25), this is indeed the case.

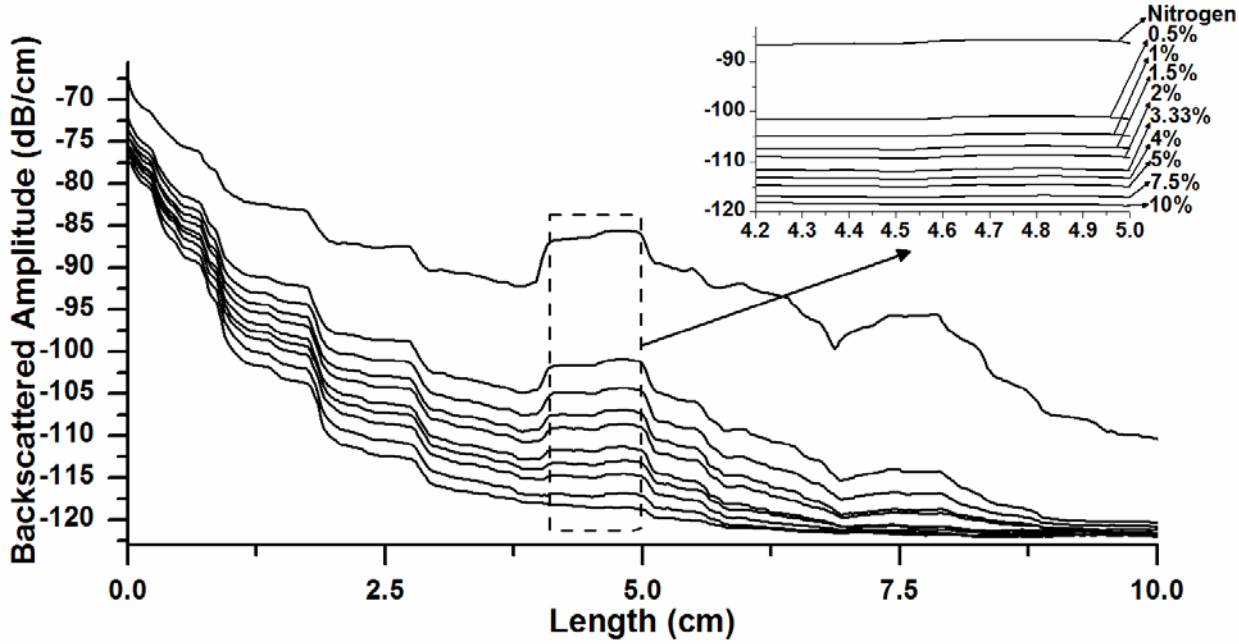

Figure 4-25. Distributed measurement (Optical Frequency Domain Reflectometry) of various concentrations of hydrogen along a 10cm portion of a Pd doped TiO2 nanomaterial coated optical fiber. The inset shows the various hydrogen concentrations from 0% to 10%.

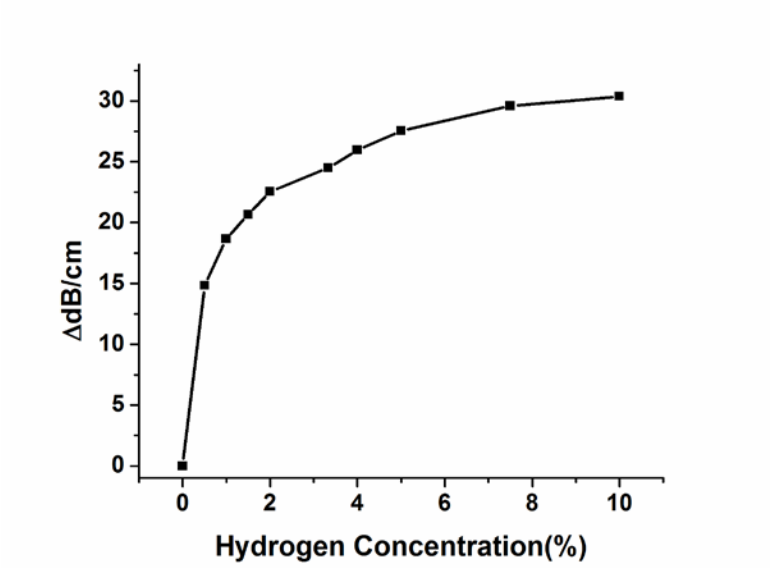

Figure 4-26. Measured change in dB/cm as a function of hydrogen concentration

The sensor was heated to 600°C in the controlled environment furnace and stabilized by exposing to Hydrogen-Nitrogen cycles, as before. After about 3hrs or cycling, the distributed measurement was performed with Frequency Domain Reflectometer (Luna OBR 4600). The concentration of Hydrogen was changed from 0.5% to 10% with various intermediate values (inset of Figure 4-25).

Just as expected, there is a variation in the backscattered amplitude of the light due to losses in the forward propagating light. A 10cm section of the coating is highlighted for which the changes in the backscattered amplitude are shown. The data was collected with a resolution of 0.1mm which was later reduced to 1cm as it made the plot look smoother. In essence, it removed the many bumpy features. It is also interesting to note that there is some waviness to the plots

which is believed to be from the coating thickness variations of the nanomaterial. The fiber is coated by hand and, therefore, such features are expected to exist at the surface of the coating. It also suggest that this type of measurement technique may be used to characterize the surface quality of the films on fiber.

4.6 CONCLUSIONS

Integrating thick functional metal oxide nanomaterial films with optical fiber using the demonstrated refractive index engineering scheme provided important results. First that the developed method can indeed be used to assist in the integration of important functional materials with optical fiber. Second, that a new type of optical sensor can be developed using such methods. And third, important sensory mechanisms surfaced upon examining the manufactured sensors.

As expected from theory, an absorptive response was present, influencing the transmission properties of the fiber sensor. However, form theory it is not clear whether a refractive index response was to be expected for nanomaterials with features in the 10nm regime, which is approximately the same as the penetration depth of the sensory response into the material. Is such cases, the material surface effects dominate, and its influence on the refractive index is not clear as the electronic properties of the surface are modulated. By incorporating fiber Brag gratings into the manufactured samples, the examination of changes in the real part of the refractive indices were characterized. Given, the sensitivity of the instruments used, we did not observe any such modulations, which would have resulted in the displacement of the grating peaks.

Lastly, the distributed type sensing capability of the manufactured Pd-doped TiO_2 sensor was examined. The results confirmed the hypothesis, that nanomaterial coatings can indeed be

used for distributed type sensing, where variations across the length of the sample can be detected. This can have a variety of potential application in industry, military, and etc. A single fiber has the potential to serve as a linear combinations of hundreds of sensors, allowing for the detection in the variation of chemical species across a certain length with a single sensor. The motivation behind examining the distributed sensing capability of the nanomaterial integrated fiber sensor was for potential use in Hydrogen drive solid oxide fuel cells. In that application, it would be used for the simultaneous determination of the temperature and Hydrogen concentration across the device. This information would then be used as a feedback mechanism for control purposes.

5.0 APPLICATIONS IN TRANSFORMATION OPTICS

Recent research efforts have shown that the transparent conducting oxide, aluminum doped zinc oxide, AZO maybe an ideally suited plasmonic material as it has the lowest optical losses after the dielectric permittivity crosses over to negative values in the near infrared (NIR) [96-98]. Using these components a realization of an effective plasmonic media was previously demonstrated by creating a layered structure consisting of 60nm tick alternating ZnO and AZO layers [99]. Most of the community researching unique refractive indices such as negative and low values has been focusing on using nano-metallic rings and other structures to create optical resonance effects in which negative refractive indices can surface. Although these structures are rather clever, there is a great difficulty in manufacturing them on a large scale and the resonance bandwidth is generally quite narrow. Alternative routes such as self-assembly and infiltration with all semiconductor constituents could lead to rapid advancements as these techniques are specifically geared towards large area and rapid manufacture or nanomaterials and would potentially overcome the bandwidth limitations.

By building on the 1D layered metamaterial demonstrated by Naik et al., it may be possible that the plasmonic behavior needed to bring forth the novel refractive index properties can surface in 3D metal oxide nanoporous structures realized by solution phase processing. Rapid advances in all semiconductor metamaterials fabricated from the solution phase could lead to practical realizations of transformation optics designed optical components as many of these require unique refractive index values and refractive index gradients currently not easily attainable, especially on a large scale. More or less, any novel optical components designed by transformation optics techniques require relatively strong refractive index gradients not easily attainable with current

technology [100]. This is due to the fact that transformation optics is inherently tensorial in nature, as it relies on finding solutions to complex problems by coordinate transformations and etc. [101]. In this dissertation the idea to attempt to manufacture a 3D sub-wavelength mixture of zinc oxide and aluminum doped zinc oxide, is explored. That is, building on the work by Naik et al. who have shown interesting optical phenomena by manufacturing a 1D effective medium comprised of ZnO (semiconductor) and AZO (aluminum doped zinc oxide, transparent conductor).

5.1 BACKGROUND AND THEORY

Transformation optics is a unique design method pioneered by Pendry et al. to design such novel optical effects as cloaking, achieved by specifically designed refractive index gradients, and flat lenses by canceling the effect of vacuum by using negative refractive indices to create a complementary medium[101]. Although, similar methods such as conformal mapping have been around for some time, this method of optical design received a lot of attention only several years ago due to the published articles dealing with optical cloaking. Since then the number of publications has increased a great deal showing the many new and clever ways this design methodology can be applied to steer light unconventionally[100]. Initially, it was used to show that under a certain permittivity and permeability gradients, light can bend in such a way as to be guided around an object, effectively making it invisible. This was demonstrated in the microwave regime where manufacturing the needed material properties is much easier, due to the scale[102]. Since then the effect has been shown with gradient photonic crystals, as well[103]. It has been shown that this method can be used to design waveguides for unique steering of light that can be extremely useful in light-wave circuits[100]. Other reports show the designs of illusion type

effects in which objects can be made to look like other things or being able to see through objects that are, otherwise, not transparent[104]. The later can be qualitatively explained by thinking of complementary media. That is, if two media with complementary permittivity and permeability properties are brought into contact, due to a canceling effect, which may be due to the generation of strong surface plasmons at the surface of contact, a media otherwise not transparent could allow the passage of light. Although many of these are quite clever, they require refractive indices and permeability and gradients in those quantities that are generally not attainable. Here lies the difficulty with this design methodology. One may easily crunch through the mathematics to get some parameter values that give a desired effect but in many cases these cannot be practically made in the near future due to the unphysical nature of the requirements. This is a powerful technique but it requires careful thinking and considerations to come up with designs that are actually realizable.

At the very core of this method lies the reformulation of Maxwell's equations into a tensor notation that is free of any coordinate system. By now we have all encountered situations in problem solving in which arriving at a solution to a particular problem is critically dependent on the path taken as certain formulations of the problem can be arbitrarily complex whose solutions might not easily be obtained. This is the basic principle of this method as one can perform a coordinate transformation to a system in which solving the problem is less cumbersome. Once a solution is found, one can simply apply the predefined transformations to find the needed parameter values in Euclidian coordinates, such as Cartesian Cylindrical and Spherical. Maxwell's equations in general form are as follows

$$\nabla \times E + i\omega\mu H = 0$$
$$\nabla \times H - i\omega\varepsilon E = 0$$

Equation 5-1

These equations, due to their form, have the property that they maintain the same form regardless of the coordinate system (form invariance). When the coordinate system is changed such that x'=x'(x), the following is obtained

$$\nabla \times E' + i\omega\mu' H' = 0$$
$$\nabla \times H' - i\omega\varepsilon' E' = 0$$

Equation 5-2

Here, the permittivity/permeability tensors ε' and μ' in the transformed coordinates are related to the ones in the original coordinate systems by the relationships

$$\varepsilon'^{i'j'} = |\det(\Lambda_i^{i'})|^{-1} \Lambda_i^{i'} \Lambda_j^{j'} \varepsilon^{ij}$$
$$\mu'^{i'j'} = |\det(\Lambda_i^{i'})|^{-1} \Lambda_i^{i'} \Lambda_j^{j'} \mu^{ij}$$

Equation 5-3

Where $\Lambda_i^{i'} = \frac{\partial x^{i'}}{\partial x^i}$ indicates the Jacobi matrix of transformation, and the det() is simply the determinant[105].

5.1 MOTIVATION

As mentioned before, it is not easy to use this methodology to arrive at realizable designs, although it is a powerful technique. A well carried out design can be exemplified by one carried out by Wu et. al. that allows efficient coupling of a point source into 4 waveguides with various other transformation optics designed components for light-wave circuits (Figures 5-1 and 5-2)[106].

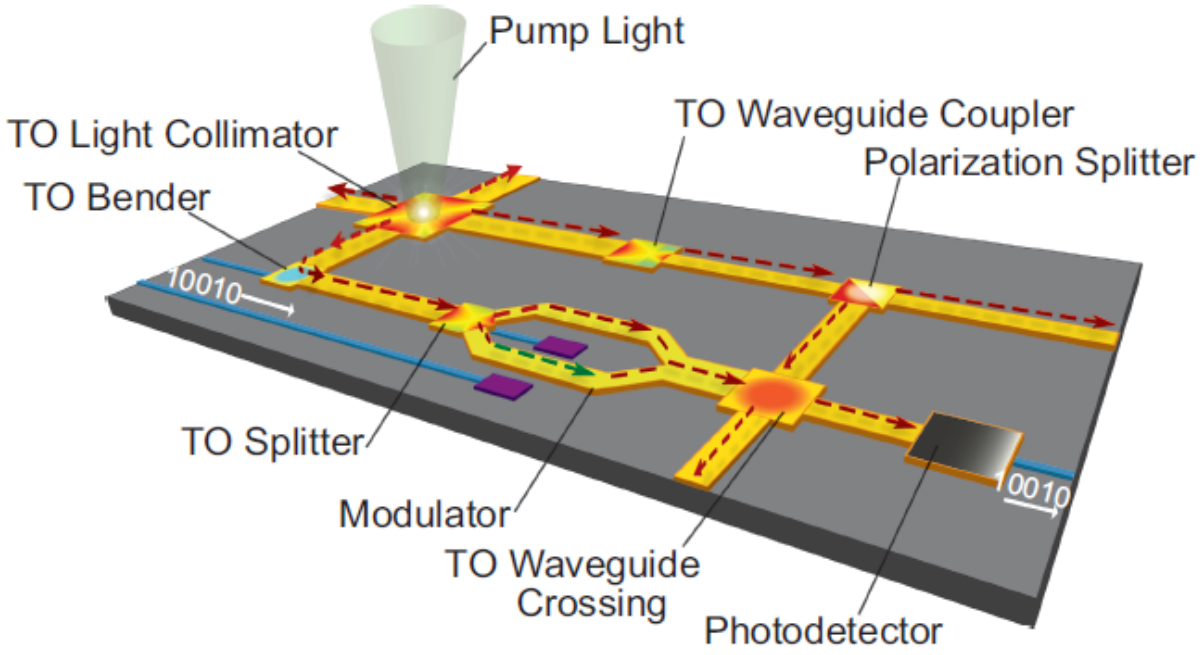

Figure 5-1. A conceptual light-wave circuit realized by transformation optics designed components[100].

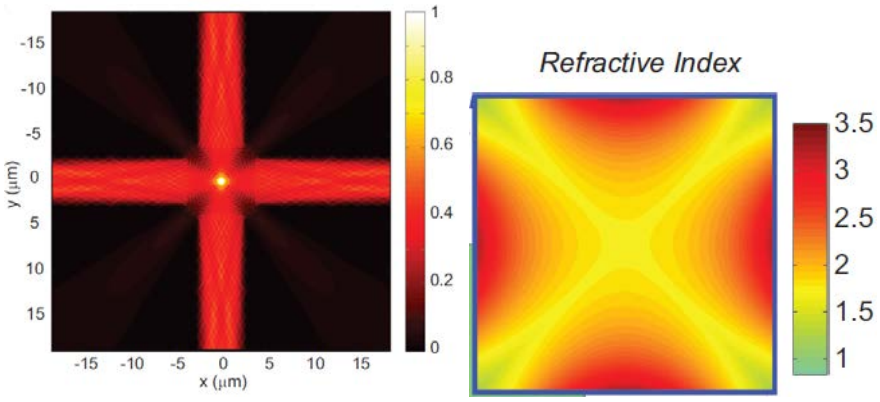

Figure 5-2. Left: Efficient four channel coupling of a point source designed by transformation optics. **Right:** The refractive index gradients needed to realize the device[100].

Although the design shown in Figure 5-2 still requires significant refractive index gradients, the refractive indices are physically feasible values. However, the realization of these gradients is not a trivial matter.

Another interesting example is by Lai et. al. in which they demonstrate that it may be possible to see through walls by placing complementary media against an objects[104]. In this scheme, the wall is metallic and has a permittivity of -1. By applying complementary media with certain material properties and some additional components found by transformation optics design, they show that wall transparency can be achieved. This design, although very nice conceptually, requires unphysical values such as negative permeability values and strong gradients in these values. This design exemplifies the difficulties that one can encounter in using transformation optics in designing otherwise very interesting and novel optical devices. At optical frequencies materials do not have a magnetic permeability other than 1, let alone realizing gradients in those. There are some clever techniques employing the making or nano-metallic resonators but these are heavily constricting. Much more research in the development of novel refractive indices is needed before this design can be realized. However, good designs can yield requirements that can be manufactured today or in the near future where the material components needed exist but the strong gradients in those needed pose the difficulties. This is where a solution phase approach developed for refractive index engineering when coupled with such technologies as dip-pen lithography might be able to overcome the manufacturing difficulties.

Motivated by previously published works detailed above, especially by the work of Naik et al. [99] who have demonstrated negative refraction by manufacturing an alternating thin film stack of zinc oxide and aluminum doped zinc oxide, a question came about. What would happen

if the same thing was done in a 3D arrangement? That is, if a 3D sub-wavelength zinc oxide nanostructure was infiltrated with aluminum doped zinc oxide? This would create a 3D sub-wavelength arrangement of semiconductor (ZnO) and conductor (AZO) interfaces. With a 1D arrangement, there are obvious angular restrictions, but with a 3D arrangement, these restrictions could be entirely lifted. Another question one may ask, which may not have an easily calculable answer is, would this behave as purely localized surface plasmons or a global distribution, or some combination of both? If a truly 3D interconnected network of such interfaces can be manufactured, the results it could present might quite interesting.

Figure 5-3. An illustration of the fundamental question that is addressed

5.2 EXPERIMENT

There are numerous publications that detail various ingredients and processing conditions for the wet preparation of highly conductive aluminum doped zinc oxide films [107-112]. The main

differences in the presented methods lie in the chemical formulations of the precursor solutions and the annealing procedures employed. Reports for the obtained resistivity have been as low as $1.2x10^{-4}$. The various annealing procedures reported range from a combination of annealing in air followed by annealing in vacuum, to annealing in argon, to annealing in various percentages of hydrogen in nitrogen, or hydrogen in argon.

After exploring several of the published methods, the ingredients presented in ref [111] were used for the preparation of the precursor solution with some modification. Although, it is uncommon for reports to specify the amount of water present in their mixtures, they also do not specify the details of their preparation conditions. Such as, whether the preparations took place in an inert environment, and so on. Therefore, the water content present in their precursor solutions could help explain the lack of consistency in the reported numbers for resistivity. Upon some preliminary exploration, we found that adding a 1:1 molar ratio of water with respect to Zn into the precursor solution assisted in partially stabilizing the variations in the formulations. In general, the doping concentration of Al used is 1%, due to limits in solubility [112]. Therefore, 1% Al doping is the concentration that is explored to manufacture low resistivity AZO films.

The general precursor consisted of the following molar ratio 1:0.01:1:2:17.3, of zinc acetate dihydrate to aluminum nitrate nonahydrate to water to monoethanolamine to 2-methoxyethanol. The precursor was prepared by first preparing a separate solution of aluminum nitrate nonahydrate in methoxyethanol which was subsequently used as the Al dopant source. In a separate glass vial zinc acetate dihydrate was dissolved in 2-methoxyethanol with an appropriate amount of monoethanolamine as stabilizer. To this the appropriate amount of water was added and stirred. After complete dissolution, an appropriate amount of the previously prepared aluminum nitrate

nonahydrate methoxyethanol solution was added. This was followed by stirring on a hotplate at 70°C for 1hr. After cooling to room temperature, the precursor was allowed to age for 1 day.

Aluminum doped zinc oxide films were prepared on both glass slides and silicon substrates, where the silicon substrate had an additional 300nm SiO_2 thermal oxide layer for insulation. Before coating, the substrates were cleaned with ethanol and dried by spinning at 5K RPM for 1 min. The precursor was coated on the substrates by the spin cast method at 3K RPM. Eight coatings were applied to each substrate to build up the film thickness and after each coating the substrates were dried on a hotplate at 350°C for 10 minutes in air. After depositing eight coatings, the samples were annealed in a furnace at 500°C in 10% Hydrogen in Argon with heating and cooling rates of 2°C/minute. The as prepared films of aluminum doped zinc oxide were characterized by measuring the sheet resistance with a four-point probe and by Ellipsometry.

5.3 RESULTS AND DISCUSSIONS

Four-point probe measurements are, by far, the most common method used for obtaining the conductivities of thin films. This is generally accomplished by measuring the sheet resistances and multiplying this by the thickness of the film. To obtain the thickness of the films, Ellipsometry was used. The obtained sheet resistances varied considerable from sample to sample, from values as high as 6KΩ/sq to as low as 68Ω/sq. Variation were observed across individual samples, as well that ranged from 68Ω/sq to 450Ω/sq. The four-point probe measurements were performed with a current of 5mA. The lowest sheet resistance obtained was 68Ω/sq, giving a resistivity of 2.4mΩ·cm. There were considerable variations in the film thickness across each sample, which

partly explains the significant variations in the sheet resistances, with a low value of 280nm to a high value 360nm.

Ellipsometry was performed on the sample that provided the lowest sheet resistance. Four location were designated on the sample with increasing sheet resistances and Ellipsometry was performed at those places. The permittivity of the aluminum doped zinc oxide films were determined by fitting a model to the measured optical data, which were measured at 70° on a glass substrate. The model representing the sample under test consisted of a glass substrate of 2mm thickness followed by material file represented by the classical mode, consisting of a Lorentz oscillator component, and a Drude term. No special consideration needed to be adhered to since the classical model fit quite well to the measurements, giving a χ^2 value on average of 10 or less over the whole spectral range. Figure 5-5 shows the obtained real and imaginary values for the permittivity for the four locations on the sample, with increasing resistivity.

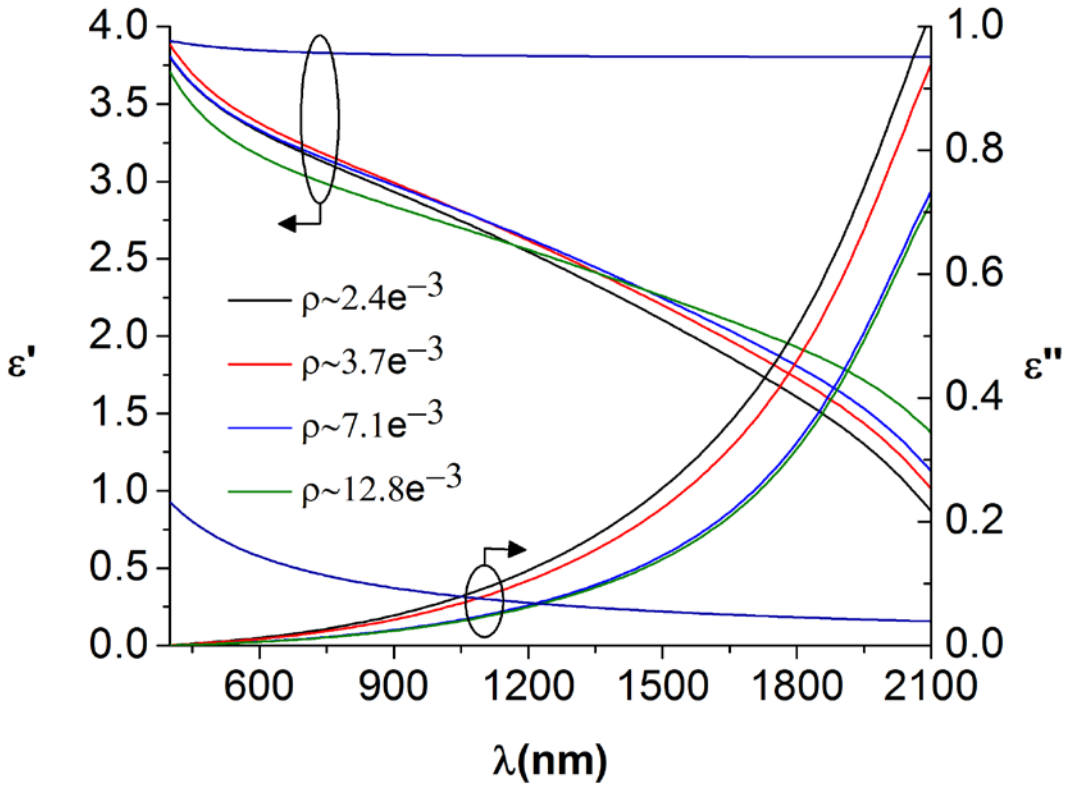

Figure 5-4. Ellipsometer measurement of the real and imaginary parts of the permittivity of ZnO and 1% Al doped ZnO. A listing of the resistivity is also included that are associated with the respective permittivity curves.

The real and imaginary permittivity of zinc oxide is also included for comparison. The real part of the permittivity for undoped zinc oxide stays more or less flat at NIR wavelength, whereas the permittivity for 1% Al doped zinc oxide changes extensively. Doping with aluminum will increase the free electron concentration and mobility which, according to Drude theory will show up as an increase in absorption at NIR wavelengths. This is essentially the trend that is observed. It is observed that when the resistivity, which is simply just the inverse of the conductivity, decrease, the real part of the permittivity decreases, as well, especially at higher wavelengths. A similar trend can also be observed in the imaginary part of the permittivity.

5.4 CONCLUSIONS

The fundamental idea that was to be explored here is the sub-wavelength mixture of zinc oxide and aluminum doped zinc oxide. The mixture would ideally create a 3D continuous network of semiconducting and conducting interfaces at which surface plasmons could be excited. Due to the 3D distribution and symmetry of the interfaces, it would be reasonable to expect that strong angular requirements generally needed to excite surface plasmons would be absent. Furthermore, a functional sample would have been examined for novel optical effect that could come about from essentially making an effective material with volume out of these plasmonic interactions. Going beyond the localized surface plasmons normally obtained by the inclusion of metal nanoparticles to a global surface plasmon effect.

During the exploration with the solution processing of aluminum doped zinc oxide, significant problems surfaced. As indicated in Figure 5-5, the obtained AZO samples had relatively high sheet resistances and, therefore, the real part of the permittivity did not cross over to negative values. The solution processing of aluminum doped zinc oxide is a difficult task, one with many parameters to carefully control. Henceforth, the obtained AZO samples did not meet the permittivity requirements to proceed to the next step of the study, which would have been infiltration. Given the opportunity and the means, I may proceed with the exploration which may include other more suitable methods of backfilling a sub-wavelength ZnO nanostructure with a much more conductive aluminum doped zinc oxide. A much higher conductivity, an increase by an order of magnitude, may be required to proceed any further with this experiment.

Furthermore, I would like to suggest another avenue for research that is in line with the developed method of 3D sub-wavelength refractive index engineering. As demonstrated, there are a variety of feasible designs carried out by transformation optics for which the current

manufacturing difficulty lies in the realization of strong refractive index gradients. For such designs, the presented refractive index engineering method coupled with such techniques as dip-pen lithography, could be of practical importance. Nowadays, dip pen lithography has evolved to where features down to the 50nm scale can be realized in massively parallel, with some 50,000 tips. This, when combined with the demonstrated solution phase refractive index engineering approach, has the potential to practically realize many of the transformation optics designs. That is, to realize the 3D refractive index gradients required by those designs.

6.0 SUMMARY AND OUTLOOK

A method allowing extensive control over the refractive indices of functional materials was presented. Controlling the refractive indices was achieved by block-copolymer assisted 3D nanostructuring in the deep sub-wavelength regime ($\lambda >> \Lambda$). 3D structuring in the sub-wavelength regime allows the use of the quasi-static formulations of effective medium theories, such as the Bruggeman effective medium theory. These types of averaging are relatively simple and yet powerful techniques that when coupled with the demonstrated nanostructuring method, provide low cost optical material engineering solutions. The refractive indices are important design parameters in optics and photonics yet nature does not provide many options in choosing the refractive indices in order to realize optimal designs. With the demonstrated scheme, easily realizable optical materials with tailor able refractive indices in the range of 2.4 to 1.17 can easily be manufactured on the large scale, relatively cost effectively.

Optical fiber type sensing is highly sought after due the relatively inert nature of the silica material components used in their manufacture. This allows fiber to be used as sensors in a wide array of extreme conditions and harsh environments such as very high temperatures (>400°C), in volatile chemical and biological environments, and environments sensitive to electrical devices. However, due to the inert nature of silica, the sensory capability of optical fibers is quite limited. Three fold contributions were provided to advance the field of optical fiber sensing. One, numerical simulations were performed to provide a theoretical framework for integrating sensory materials with optical fiber. Two, by applying the developed refractive index engineering scheme, it was demonstrated that functional sensory materials such as SnO_2 and TiO_2, and their doped variants, can be effectively combined with optical fiber. And three, the type of the sensory

response of the integrated sensors were characterized. With the demonstrated integrated sensors, chemical sensitivity to ammonia and hydrogen were demonstrated, in essence, providing a new method for optical fiber type sensing. Due the limited exploration of functional sensory metal oxides with optical fiber, an opportunity was provided for explorations. Fiber Brag gratings inscribed into the core of the optical fiber sensors coupled with transmission type analysis assisted in demining their sensory responses. An absorptive response was expected however, the effects on the real part of the refractive indices of sensory material due to complete, or near complete modulations were not clear from the theory. The obtained measurement results indicated that there were no significant changes in the real refractive indices due to complete material modulations. At least, on a scale detectable with the instruments used. On the other hand, strong absorptive responses were observed. Therefore, the presented method and results provide important guidance for the design of optical fiber sensors for applications in chemical and biological sensing.

Frequency domain optical reflectometry type measurements were performed on the palladium doped titanium dioxide fabricated fiber sensor. With this type of measurement, it was demonstrated that there exist the potential for the detection of chemical and biological concentration gradients across a single sensor element. A single fiber sensor can, in essence, be used as a linear combination of hundreds of sensors with a relatively high spatial resolution. These types of measurements when coupled with the demonstrated method to integrate functional sensory materials with optical fiber, have a wide scope of applicability from industry, to military, to, commercial sensing. Specifically, it can be directly deployed in hydrogen driven solid oxide fuel cells for monitoring and, even possibly, controlling the conversion efficiencies.

Anti-reflection coatings play a crucial role in today's technology for eliminating specular reflections on eyewear, car windows, precision optical components, to solar cells. Availability of

materials with a wide range of refractive indices is of paramount importance in designing the best anti-reflection coatings. Today, the most common form of anti-reflection coatings employed are in the form of quarter wave dielectric stacks and single layer coatings. Dielectric stacks are quite efficient in eliminating reflections but are strongly limited in their angular and wavelength operational ranges. Single coatings offer broader acceptances but with the cost of higher reflectivity. From theory, the lowest reflectivity is achieved when a continuous gradual refractive index change from the surface to the background material is realized. With today's technology, these are too difficult and costly to realize. Practical approximations to these are layered coatings that approximate the continuous functions with an increasing level of accuracy. These require the realization of large scale materials with refractive indices not provided to us by nature. Some techniques such as chemical vapor deposition, sputtering, and e-beam evaporation have been shown to control refractive indices, but these are restrictive and costly methods. Therefore, the application of the developed low cost solution processing route to tailor the refractive indices of materials was demonstrated. It was shown that wide angular acceptance and broad wavelength anti-reflection coatings can easily be realized with the demonstrated technique. In the 400-700nm range with an acceptance angle of 0-60° from the normal, with only a two layer coating on silicon wafer, an average reflectivity of 3% was demonstrated. This is already a substantial improvement over the 7% normally achieved with the industry convention of a 1-layer TiO_2 coating. The method demonstrated is of practical use however, it has some limits. With the current method, the lowest achievable refractive index is 1.17. Further developments that extend the range of the demonstrated refractive index engineering scheme could provide even higher improvements in eliminating reflective losses. When dealing with solar cells, even a 1% improvement in the energy conversion efficiency can be of substantial merit.

With the last explored application, an attempt was made to explore refractive index engineering beyond the normal range with a 3D geometry. That is, conventional materials have refractive indices of 1 or greater, whereas the attempt was to achieve refractive indices below 1 towards achieving negative values, with all semiconductor components. The idea was to build on the work of Naik et al. who have shown metamaterial properties of sub-wavelength layered media of conductive and semiconductive interfaces. That is, to extend the dimensionality of the demonstrated layered media by infiltrating a sub-wavelength 3D ZnO nanostructure with a solution processed Al-doped zinc oxide. In hope of achieving angle-insensitive easily fabricable on the large scale optical metamaterials with unconventional refractive indices (such as <1 and negative values). Upon exploration, difficulties were encountered in the manufacture of highly conductive Al-doped zinc oxide via the solution processing route. The realized Al-doped zinc oxide materials did not have low enough electrical conductivities for the dielectric permittivity to cross over to negative value at NIR wavelengths. It is believed that, at least, and order of magnitude reduction is required in the lowest obtained resistivity of $2.4 \times 10^{-3} \Omega cm$ in order to obtain the required zero crossing. Therefore, the experiment could not proceed to the next step, which would have been the infiltration of a 3D ZnO nanostructure with a solution processed Al-doped ZnO materials. Given the opportunity, I would like to further explore this scheme of refractive index engineering, either by improving on the existing solution processing route or by exploring alternate routes for infiltration with highly transparent conductors.

Transformation optics is an interesting design methodology with the capability to influence the next generation of optical devices. However, many of the designs require refractive index gradients in 3D space that are not easily achievable, if at all, with current technology. Therefore, I would like to suggest that the demonstrated refractive index engineering scheme, when coupled

with such techniques as dip-pen lithography, may hold the potential to manufacture many of the transformation optics designs effectively and at low cost. This combination could be used to realize the 3D refractive index gradients by deep sub-wavelength nano-engineering.

BIBLIOGRAPHY

[1] A. P. Alivisatos, "Semiconductor Clusters, Nanocrystals, and Quantum Dots," Science, 271(5251), 933-937 (1996).

[2] R. S. Devan, R. A. Patil, J.-H. Lin *et al.*, "One-Dimensional Metal-Oxide Nanostructures: Recent Developments in Synthesis, Characterization, and Applications," Advanced Functional Materials, 22(16), 3326-3370 (2012).

[3] M. Haruta, and M. Daté, "Advances in the catalysis of Au nanoparticles," Applied Catalysis A: General, 222(1–2), 427-437 (2001).

[4] S. Vignolini, N. A. Yufa, P. S. Cunha *et al.*, "A 3D Optical Metamaterial Made by Self-Assembly," Advanced Materials, 24(10), OP23-OP27 (2012).

[5] F. W. Wise, "Lead Salt Quantum Dots: the Limit of Strong Quantum Confinement," Accounts of Chemical Research, 33(11), 773-780 (2000).

[6] A. Pimpin, and W. Srituravanich, [Review on Micro- and Nanolithography Techniques and Their Applications], (2011).

[7] D. Xia, Z. Ku, S. C. Lee *et al.*, "Nanostructures and Functional Materials Fabricated by Interferometric Lithography," Advanced Materials, 23(2), 147-179 (2011).

[8] K. Salaita, Y. Wang, and C. A. Mirkin, "Applications of dip-pen nanolithography," Nat Nano, 2(3), 145-155 (2007).

[9] Y. B. Liu, and X. S. Wang, "Recent advances in block copolymer-assisted synthesis of supramolecular inorganic/organic hybrid colloids," Polymer Chemistry, 2(12), 2741-2757 (2011).

[10] J. Y. Cheng, C. A. Ross, H. I. Smith *et al.*, "Templated Self-Assembly of Block Copolymers: Top-Down Helps Bottom-Up," Advanced Materials, 18(19), 2505-2521 (2006).

[11] M. C. Orilall, and U. Wiesner, "Block copolymer based composition and morphology control in nanostructured hybrid materials for energy conversion and storage: solar cells, batteries, and fuel cells," Chemical Society Reviews, 40(2), 520-535 (2011).

[12] Y. Deng, J. Wei, Z. Sun *et al.*, "Large-pore ordered mesoporous materials templated from non-Pluronic amphiphilic block copolymers," Chemical Society Reviews, 42(9), 4054-4070 (2013).

[13] D. Wei, M. R. J. Scherer, C. Bower *et al.*, "A Nanostructured Electrochromic Supercapacitor," Nano Letters, 12(4), 1857-1862 (2012).

[14] P. R. Solanki, A. Kaushik, V. V. Agrawal *et al.*, "Nanostructured metal oxide-based biosensors," NPG Asia Mater, 3, 17-24 (2011).

[15] B. Schwenzer, L. Wang, J. S. Swensen *et al.*, "Tuning the Optical Properties of Mesoporous TiO2 Films by Nanoscale Engineering," Langmuir, 28(26), 10072-10081 (2012).

[16] G. Stewart, F. A. Muhammad, and B. Culshaw, "Sensitivity improvement for evanescent-wave gas sensors," Sensors and Actuators B: Chemical, 11(1–3), 521-524 (1993).

[17] Z. Jia, "Determination of the effective refractive index of porous silicon/polymer composite films," Chinese Optics Letters, 3(10), 608-610 (2005).

[18] A. Blanco, E. Chomski, S. Grabtchak *et al.*, "Large-scale synthesis of a silicon photonic crystal with a complete three-dimensional bandgap near 1.5 micrometres," Nature, 405(6785), 437-440 (2000).

[19] T. C. Choy, [Effective medium theory : principles and applications] Clarendon Press ; Oxford University Press, Oxford England New York(1999).

[20] W. L. Min, P. Jiang, and B. Jiang, "Large-scale assembly of colloidal nanoparticles and fabrication of periodic subwavelength structures," Nanotechnology, 19(47), (2008).

[21] S. Shao, M. Dimitrov, N. Guan *et al.*, "Crystalline nanoporous metal oxide thin films by post-synthetic hydrothermal transformation: SnO2 and TiO2," Nanoscale, 2(10), 2054-2057 (2010).

[22] V. N. Urade, and H. W. Hillhouse, "Synthesis of Thermally Stable Highly Ordered Nanoporous Tin Oxide Thin Films with a 3D Face-Centered Orthorhombic Nanostructure," The Journal of Physical Chemistry B, 109(21), 10538-10541 (2005).

[23] P. Yang, D. Zhao, D. I. Margolese *et al.*, "Block Copolymer Templating Syntheses of Mesoporous Metal Oxides with Large Ordering Lengths and Semicrystalline Framework," Chemistry of Materials, 11(10), 2813-2826 (1999).

[24] M. P. Tate, V. N. Urade, S. J. Gaik *et al.*, "How to Dip-Coat and Spin-Coat Nanoporous Double-Gyroid Silica Films with EO19-PO43-EO19 Surfactant (Pluronic P84) and Know it Using a Powder X-ray Diffractometer," Langmuir, 26(6), 4357-4367 (2010).

[25] M. C. Orilall, N. M. Abrams, J. Lee *et al.*, "Highly crystalline inverse opal transition metal oxides via a combined assembly of soft and hard chemistries," Journal of the American Chemical Society, 130(28), 8882-+ (2008).

[26] Y. M. Lam, N. Grigorieff, and G. Goldbeck-Wood, “Direct visualisation of micelles of Pluronic block copolymers in aqueous solution by cryo-TEM,” Physical Chemistry Chemical Physics, 1(14), 3331-3334 (1999).

[27] N. W. Ashcroft, and N. D. Mermin, [Solid state physics] Holt, New York,(1976).

[28] T. Choy, [Effective Medium Theory: Principles and Applications (International Series of Monographs on Physics (Oxford, England), 102.)] Oxford Univ Pr (Sd).

[29] W. contributors, “Ellipsometry,” Wikipedia, The Free Encyclopedia.

[30] H. J. Yvon, “Classical Dispersion Model,” http://www.horiba.com/fileadmin/uploads/Scientific/Downloads/OpticalSchool_CN/TN/ellipsometer/Classical_Dispersion_Model.pdf.

[31] H. J. Yvon, “New Amorphous Dispersion Formula,” http://www.horiba.com/fileadmin/uploads/Scientific/Downloads/OpticalSchool_CN/TN/ellipsometer/New_Amorphous_Dispersion_Formula.pdf.

[32] V. N. Urade, T.-C. Wei, M. P. Tate *et al.*, “Nanofabrication of Double-Gyroid Thin Films,” Chemistry of Materials, 19(4), 768-777 (2007).

[33] S. A. Sergeenko, P. S. Yaremov, V. N. Solomakha *et al.*, “Effect of synthesis conditions on the structure and sorption properties of films based on mesoporous tin dioxide,” Theoretical and Experimental Chemistry, 46(3), 197-202 (2010).

[34] M. A. Green, “Self-consistent optical parameters of intrinsic silicon at 300 K including temperature coefficients,” Solar Energy Materials and Solar Cells, 92(11), 1305-1310 (2008).

[35] E. D. Palik, [Handbook of optical constants of solids] Academic Press, Orlando(1985).

[36] B. S. Richards, “Single-material TiO(2) double-layer antireflection coatings,” Solar Energy Materials and Solar Cells, 79(3), 369-390 (2003).

[37] T. Saga, “Advances in crystalline silicon solar cell technology for industrial mass production,” Npg Asia Materials, 2(3), 96-102 (2010).

[38] L. A. Dobrzanski, and A. Drygala, “Laser processing of multicrystalline silicon for texturization of solar cells,” Journal of Materials Processing Technology, 191(1-3), 228-231 (2007).

[39] Y. F. Huang, S. Chattopadhyay, Y. J. Jen *et al.*, “Improved broadband and quasi-omnidirectional anti-reflection properties with biomimetic silicon nanostructures,” Nature Nanotechnology, 2(12), 770-774 (2007).

[40] C. Lee, S. Y. Bae, S. Mobasser *et al.*, “A novel silicon nanotips antireflection surface for the micro sun sensor,” Nano Letters, 5(12), 2438-2442 (2005).

[41] L. Schirone, G. Sotgiu, and F. P. Califano, “Chemically etched porous silicon as an anti-reflection coating for high efficiency solar cells,” Thin Solid Films, 297(1-2), 296-298 (1997).

[42] M. Tao, W. D. Zhou, H. J. Yang *et al.*, “Surface texturing by solution deposition for omnidirectional antireflection,” Applied Physics Letters, 91(8), (2007).

[43] J. Zhao, and M. A. Green, “Optimized Antireflection Coatings for High-Efficiency Silicon Solar-Cells,” Ieee Transactions on Electron Devices, 38(8), 1925-1934 (1991).

[44] G. Wu, J. Wang, S. Jun *et al.*, "Preparation and properties of scratch-resistant nanoporous broadband AR silica films derived by a two-step catalytic sol-gel process." 4086, 807-810.

[45] H. Park, D. Shin, G. Kang *et al.*, “Broadband Optical Antireflection Enhancement by Integrating Antireflective Nanoislands with Silicon Nanoconical-Frustum Arrays,” Advanced Materials, 23(48), 5796-5800 (2011).

[46] Y. Kanamori, M. Sasaki, and K. Hane, “Broadband antireflection gratings fabricated upon silicon substrates,” Optics Letters, 24(20), 1422-1424 (1999).

[47] C. H. Sun, W. L. Min, N. C. Linn *et al.*, “Templated fabrication of large area subwavelength antireflection gratings on silicon,” Applied Physics Letters, 91(23), (2007).

[48] S. Wang, X. Z. Yu, and H. T. Fan, “Simple lithographic approach for subwavelength structure antireflection,” Applied Physics Letters, 91(6), (2007).

[49] B. Paivanranta, T. Saastamoinen, and M. Kuittinen, “A wide-angle antireflection surface for the visible spectrum,” Nanotechnology, 20(37), (2009).

[50] S. Chhajed, M. F. Schubert, J. K. Kim *et al.*, “Nanostructured multilayer graded-index antireflection coating for Si solar cells with broadband and omnidirectional characteristics,” Applied Physics Letters, 93(25), (2008).

[51] M. L. Kuo, D. J. Poxson, Y. S. Kim *et al.*, “Realization of a near-perfect antireflection coating for silicon solar energy utilization,” Optics Letters, 33(21), 2527-2529 (2008).

[52] J. Q. Xi, M. F. Schubert, J. K. Kim *et al.*, “Optical thin-film materials with low refractive index for broadband elimination of Fresnel reflection,” Nature Photonics, 1(3), 176-179 (2007).

[53] J. W. Chen, B. Wang, Y. Yang *et al.*, “Porous anodic alumina with low refractive index for broadband graded-index antireflection coatings,” Applied Optics, 51(28), 6839-6843 (2012).

[54] F. C. Y. Zhao, Q. Shen, and L. Zhang, "Optimal design of graded refractive index profile for broadband omnidirectional antireflection coatings using genetic programming," Progress In Electromagnetics Research, 145, 39-48 (2014).

[55] M. Born, and E. Wolf, [Principles of optics : electromagnetic theory of propagation, interference and diffraction of light] Cambridge University Press, Cambridge ; New York(1999).

[56] M. F. Schubert, F. W. Mont, S. Chhajed *et al.*, "Design of multilayer antireflection coatings made from co-sputtered and low-refractive-index materials by genetic algorithm," Optics Express, 16(8), 5290-5298 (2008).

[57] Y. J. Chang, and Y. T. Chen, "Broadband omnidirectional antireflection coatings for metal-backed solar cells optimized using simulated annealing algorithm incorporated with solar spectrum," Optics Express, 19(14), A875-A887 (2011).

[58] X. Guo, H. Y. Zhou, S. Guo *et al.*, "Design of broadband omnidirectional antireflection coatings using ant colony algorithm," Optics Express, 22(13), A1137-A1144 (2014).

[59] I.-D. Kim, A. Rothschild, B. H. Lee *et al.*, "Ultrasensitive Chemiresistors Based on Electrospun TiO2 Nanofibers," Nano Letters, 6(9), 2009-2013 (2006).

[60] S. Akbar, P. Dutta, and C. Lee, "High-Temperature Ceramic Gas Sensors: A Review," International Journal of Applied Ceramic Technology, 3(4), 302-311 (2006).

[61] G. Korotcenkov, "Gas response control through structural and chemical modification of metal oxide films: state of the art and approaches," Sensors and Actuators B: Chemical, 107(1), 209-232 (2005).

[62] G. Korotcenkov, "Metal oxides for solid-state gas sensors: What determines our choice?," Materials Science and Engineering: B, 139(1), 1-23 (2007).

[63] N. Yamazoe, "New approaches for improving semiconductor gas sensors," Sensors and Actuators B: Chemical, 5(1–4), 7-19 (1991).

[64] N. Yamazoe, "Toward innovations of gas sensor technology," Sensors and Actuators B: Chemical, 108(1–2), 2-14 (2005).

[65] E. Comini, G. Faglia, M. Ferroni *et al.*, "Metal oxide nanowires: Preparation and application in gas sensing," Journal of Molecular Catalysis A: Chemical, 305(1–2), 170-177 (2009).

[66] M. E. Franke, T. J. Koplin, and U. Simon, "Metal and Metal Oxide Nanoparticles in Chemiresistors: Does the Nanoscale Matter?," Small, 2(1), 36-50 (2006).

[67] A. Ponzoni, E. Comini, I. Concina *et al.*, "Nanostructured Metal Oxide Gas Sensors, a Survey of Applications Carried out at SENSOR Lab, Brescia (Italy) in the Security and Food Quality Fields," Sensors, 12(12), 17023-17045 (2012).

[68] H. Zheng, J. Z. Ou, M. S. Strano *et al.*, "Nanostructured Tungsten Oxide – Properties, Synthesis, and Applications," Advanced Functional Materials, 21(12), 2175-2196 (2011).

[69] K. Schroeder, W. Ecke, and R. Willsch, "Optical fiber Bragg grating hydrogen sensor based on evanescent-field interaction with palladium thin-film transducer," Optics and Lasers in Engineering, 47(10), 1018-1022 (2009).

[70] M. Yang, and J. Dai, "Review on optical fiber sensors with sensitive thin films," Photonic Sensors, 2(1), 14-28 (2012).

[71] M. Yang, J. Dai, X. Li *et al.*, "Side-polished fiber Bragg grating refractive index sensor with TbFeCo magnetoptic thin film," Journal of Applied Physics, 108(3), 033102-4 (2010).

[72] Z. Gu, Y. Xu, and K. Gao, "Optical fiber long-period grating with solgel coating for gas sensor," Opt. Lett., 31(16), 2405-2407 (2006).

[73] S. Sumida, S. Okazaki, S. Asakura *et al.*, "Distributed hydrogen determination with fiber-optic sensor," Sensors and Actuators B: Chemical, 108(1–2), 508-514 (2005).

[74] X. Tang, J. Provenzano, Z. Xu *et al.*, "Acidic ZSM-5 zeolite-coated long period fiber grating for optical sensing of ammonia," Journal of Materials Chemistry, 21(1), 181-186 (2011).

[75] X. Wei, T. Wei, J. Li *et al.*, "Strontium cobaltite coated optical sensors for high temperature carbon dioxide detection," Sensors and Actuators B: Chemical, 144(1), 260-266 (2010).

[76] Q. Yan, S. Tao, and H. Toghiani, "Optical fiber evanescent wave absorption spectrometry of nanocrystalline tin oxide thin films for selective hydrogen sensing in high temperature gas samples," Talanta, 77(3), 953-61 (2009).

[77] J. Zhang, M. Luo, H. Xiao *et al.*, "Interferometric Study on the Adsorption-Dependent Refractive Index of Silicalite Thin Films Grown on Optical Fibers," Chemistry of Materials, 18(1), 4-6 (2005).

[78] J. Zhang, X. Tang, J. Dong *et al.*, "Zeolite thin film-coated long period fiber grating sensor for measuring trace chemical," Opt. Express, 16(11), 8317-8323 (2008).

[79] A. Hartung, S. Brueckner, and H. Bartelt, "Limits of light guidance in optical nanofibers," Opt. Express, 18(4), 3754-3761 (2010).

[80] B. E. A. Saleh, and M. C. Teich, [Fundamentals of photonics] Wiley-Interscience, Hoboken, N.J.(2007).

[81] Daveofthenewcity, "Optical fibre modes," http://commons.wikimedia.org/wiki/File:Optical_fibre_modes.jpg, (2007).

[82] J. Moon, J. A. Park, S. J. Lee *et al.*, "Pd-doped TiO2 nanofiber networks for gas sensor applications," Sensors and Actuators B-Chemical, 149(1), 301-305 (2010).

[83] R. V. Baltz, and W. Escher, "Quantum-Theory of Free Carrier Absorption," Physica Status Solidi B-Basic Research, 51(2), 499-& (1972).

[84] H. Peelaers, E. Kioupakis, and C. G. Van de Walle, "Fundamental limits on optical transparency of transparent conducting oxides: Free-carrier absorption in SnO[sub 2]," Applied Physics Letters, 100(1), 011914-3 (2012).

[85] K. J. Albert, N. S. Lewis, C. L. Schauer *et al.*, "Cross-Reactive Chemical Sensor Arrays," Chemical Reviews, 100(7), 2595-2626 (2000).

[86] M. Buric, K. P. Chen, M. Bhattarai *et al.*, "Active fiber Bragg grating hydrogen sensors for all-temperature operation," Ieee Photonics Technology Letters, 19(5-8), 255-257 (2007).

[87] M. Buric, T. Chen, M. Maklad *et al.*, "Multiplexable Low-Temperature Fiber Bragg Grating Hydrogen Sensors," Ieee Photonics Technology Letters, 21(21), 1594-1596 (2009).

[88] R. R. J. Maier, B. J. S. Jones, J. S. Barton *et al.*, "Fibre optics in palladium-based hydrogen sensing," Journal of Optics a-Pure and Applied Optics, 9(6), S45-S59 (2007).

[89] M. Suleiman, N. M. Jisrawi, O. Dankert *et al.*, "Phase transition and lattice expansion during hydrogen loading of nanometer sized palladium clusters," Journal of Alloys and Compounds, 356, 644-648 (2003).

[90] M. L. Åslund, J. Canning, M. Stevenson *et al.*, "Thermal stabilization of Type I fiber Bragg gratings for operation up to 600°C," Opt. Lett., 35(4), 586-588 (2010).

[91] S. Bandyopadhyay, J. Canning, P. Biswas *et al.*, "A study of regenerated gratings produced in germanosilicate fibers by high temperature annealing," Opt. Express, 19(2), 1198-1206 (2011).

[92] A. Lassesson, M. Schulze, J. van Lith *et al.*, "Tin oxide nanocluster hydrogen and ammonia sensors," Nanotechnology, 19(1), (2008).

[93] T. Iwanaga, T. Hyodo, Y. Shimizu *et al.*, "H-2 sensing properties and mechanism of anodically oxidized TiO2 film contacted with Pd electrode," Sensors and Actuators B-Chemical, 93(1-3), 519-525 (2003).

[94] M. K. Kumar, L. K. Tan, N. N. Gosvami *et al.*, "Conduction-atomic force microscopy study of H-2 sensing mechanism in Pd nanoparticles decorated TiO2 nanofilm," Journal of Applied Physics, 106(4), (2009).

[95] A. K. Singh, S. B. Patil, U. T. Nakate *et al.*, "Effect of Pd and Au Sensitization of Bath Deposited Flowerlike TiO2 Thin Films on CO Sensing and Photocatalytic Properties," Journal of Chemistry, 2013, 8 (2013).

[96] G. V. Naik, J. Kim, and A. Boltasseva, "Oxides and nitrides as alternative plasmonic materials in the optical range [Invited]," Optical Materials Express, 1(6), 1090-1099 (2011).

[97] M. A. Bodea, G. Sbarcea, G. V. Naik *et al.*, "Negative permittivity of ZnO thin films prepared from aluminum and gallium doped ceramics via pulsed-laser deposition," Applied Physics A, 110(4), 929-934 (2013).

[98] H. Kim, M. Osofsky, S. M. Prokes *et al.*, "Optimization of Al-doped ZnO films for low loss plasmonic materials at telecommunication wavelengths," Applied Physics Letters, 102(17), - (2013).

[99] G. V. Naik, J. Liu, A. V. Kildishev *et al.*, "Demonstration of Al:ZnO as a plasmonic component for near-infrared metamaterials," Proceedings of the National Academy of Sciences, 109(23), 8834-8838 (2012).

[100] Q. Wu, J. P. Turpin, and D. H. Werner, "Integrated photonic systems based on transformation optics enabled gradient index devices," Light-Science & Applications, 1, (2012).

[101] J. B. Pendry, D. Schurig, and D. R. Smith, "Controlling electromagnetic fields," Science, 312(5781), 1780-1782 (2006).

[102] D. Schurig, J. J. Mock, B. J. Justice *et al.*, "Metamaterial electromagnetic cloak at microwave frequencies," Science, 314(5801), 977-980 (2006).

[103] J. Valentine, J. S. Li, T. Zentgraf *et al.*, "An optical cloak made of dielectrics," Nature Materials, 8(7), 568-571 (2009).

[104] Y. Lai, J. Ng, H. Chen *et al.*, "Illusion Optics: The Optical Transformation of an Object into Another Object," Physical Review Letters, 102(25), 253902 (2009).

[105] D. Schurig, J. B. Pendry, and D. R. Smith, "Calculation of material properties and ray tracing in transformation media," Optics Express, 14(21), 9794-9804 (2006).

[106] Q. Wu, J. P. Turpin, and D. H. Werner, "Integrated photonic systems based on transformation optics enabled gradient index devices," Light Sci Appl, 1, e38 (2012).

[107] M. J. Alam, and D. C. Cameron, “Preparation and properties of transparent conductive aluminum-doped zinc oxide thin films by sol-gel process,” Journal of Vacuum Science & Technology a-Vacuum Surfaces and Films, 19(4), 1642-1646 (2001).

[108] H. Hagendorfer, K. Lienau, S. Nishiwaki *et al.*, “Highly Transparent and Conductive ZnO: Al Thin Films from a Low Temperature Aqueous Solution Approach,” Advanced Materials, 26(4), 632-636 (2014).

[109] N. F. Shih, S. T. Chen, C. C. Chang *et al.*, “Comparisons of Transparency AZO Films Using Sol-Gel and RF Sputtering Methods,” Journal of Superconductivity and Novel Magnetism, 23(6), 1189-1192 (2010).

[110] W. Tang, and D. C. Cameron, “Aluminum-Doped Zinc-Oxide Transparent Conductors Deposited by the Sol-Gel Process,” Thin Solid Films, 238(1), 83-87 (1994).

[111] H. Wang, M. H. Xu, J. W. Xu *et al.*, “Low temperature synthesis of sol-gel derived Al-doped ZnO thin films with rapid thermal annealing process,” Journal of Materials Science-Materials in Electronics, 21(6), 589-594 (2010).

[112] Y. L. Zhang, W. Y. Wang, R. Q. Tan *et al.*, “The Solubility and Temperature Dependence of Resistivity for Aluminum-Doped Zinc Oxide Ceramic,” International Journal of Applied Ceramic Technology, 9(2), 374-381 (2012).